

**DOCTORAL THESIS**

# Microstructural Homogenisation of Selective Laser Melted Ti6Al4V and CoCrFeMnNi High-Entropy Alloys

Javad Karimi

TALLINN UNIVERSITY OF TECHNOLOGY  
DOCTORAL THESIS  
52/2022

# **Microstructural Homogenisation of Selective Laser Melted Ti6Al4V and CoCrFeMnNi High-Entropy Alloys**

JAVAD KARIMI



TALLINN UNIVERSITY OF TECHNOLOGY

School of Engineering

Department of Mechanical and Industrial Engineering

This dissertation was accepted for the defence of the degree 02/08/2022

**Supervisor:** Dr. Prashanth Konda Gokuldoss, Professor  
Department of Mechanical and Industrial Engineering  
Tallinn University of Technology  
Tallinn, Estonia

**Co-supervisor:** Dr. Lauri Kollo  
Department of Mechanical and Industrial Engineering  
Tallinn University of Technology  
Tallinn, Estonia

**Opponents:** Dr. Seyed Mohammad Javad Razavi, Professor  
Department of Mechanical and Industrial Engineering  
Norwegian University of Science and Technology  
Trondheim, Norway

Dr. Jayaraj Jayamani, Professor  
School of Information and Engineering  
Dalarna University  
Falun, Sweden

**Defence of the thesis:** 09/09/2022, Tallinn

**Declaration:**

Hereby I declare that this doctoral thesis, my original investigation and achievement, submitted for the doctoral degree at Tallinn University of Technology has not been submitted for doctoral or equivalent academic degree.

Javad Karimi

-----  
signature



European Union  
European Regional  
Development Fund



Investing  
in your future

Copyright: Javad Karimi, 2022

ISSN 2585-6898 (publication)

ISBN 978-9949-83-891-2 (publication)

ISSN 2585-6901 (PDF)

ISBN 978-9949-83-892-9 (PDF)

Printed by Koopia Niini & Rauam

TALLINNA TEHNIKAÜLIKOOL  
DOKTORITÖÖ  
52/2022

**Selektiivse lasersulatuse teel valmistatud  
Ti6Al4V ja kõrgentroopse CoCrFeMnNi  
sulamite mikrostruktuuri  
homogeniseerimine**

JAVAD KARIMI





# Contents

List of publications.....	6
Author’s contribution to the publications .....	7
Introduction .....	8
List of abbreviations.....	9
1 Literature review.....	10
1.1 Additive manufacturing classification.....	10
1.2 Selective laser melting process.....	11
1.3 Production of metal powders .....	16
1.4 SLM of metallic alloys .....	20
1.4.1 SLM Ti6Al4V alloys .....	22
1.4.2 SLM of HEAs .....	23
1.5 The objectives of the thesis .....	24
2 Experimental methodology.....	25
2.1 Gas atomized and elemental powders .....	25
2.2 SLM system .....	25
2.3 Microstructure characterisation.....	26
2.3.1 Metallographic preparation .....	26
2.3.2 Phase identification and microstructural characterisation.....	27
2.4 Residual stress measurement.....	27
2.5 Characterisation of physical and mechanical properties.....	28
2.5.1 Hardness and microhardness testing.....	28
2.5.2 Tension and compression testing .....	28
2.5.3 High cycle fatigue testing .....	28
2.5.4 Charpy impact testing .....	28
2.5.5 Density .....	29
2.6 Tribological characterisation .....	29
3 Homogenisation of SLM HEAs.....	30
3.1 In-situ high-entropy alloying from elemental powders.....	30
3.2 SLM from GA HEA powder .....	34
4 Homogenisation of SLM Ti6Al4V alloys.....	38
4.1 In-situ Ti6Al4V alloying from elemental powders.....	38
4.2 SLM from GA Ti6Al4V powder .....	41
5 Discussion.....	48
5.1 In-situ alloyed materials .....	48
5.2 SLM from GA powder: Effect of laser remelting.....	51
6 Conclusions and future works.....	55
6.1 Conclusions.....	55
6.2 Suggestions for future work .....	56
References .....	57
Acknowledgements.....	64
Abstract .....	65
Lühikokkuvõte.....	67
Appendix .....	69
Curriculum vitae.....	116
Elulookirjeldus.....	117

## List of publications

The list of author's publications, on the basis of which the thesis has been prepared:

- Paper I **Karimi, J.**, Ma, P., Jia, Y. D., & Prashanth, K. G. (2020). Linear patterning of high entropy alloy by additive manufacturing. *Manufacturing Letters*, 24, 9–13.
- Paper II **Karimi, J.**, Suryanarayana, C., Okulov, I., & Prashanth, K. G. (2021a). Selective laser melting of Ti6Al4V: Effect of laser re-melting. *Materials Science and Engineering: A*, 802, 140558.
- Paper III **Karimi, J.**, Xie, M. S., Wang, Z., & Prashanth, K. G. (2021b). Influence of substructures on the selective laser melted Ti-6Al-4V alloy as a function of laser re-melting. *Journal of Manufacturing Processes*, 68, 1387–1394.
- Paper IV **Karimi, J.**, Antonov, M., Kollo, L., & Prashanth, K. G. (2022). Role of laser remelting and heat treatment in mechanical and tribological properties of selective laser melted Ti6Al4V alloy. *Journal of Alloys and Compounds*, 897, 163207.

## **Author's contribution to the publications**

Contribution to the papers in this thesis are:

- Paper I First author. Methodology. Design of experiments. Conducting experiments. Formal analysis. Data analysis. Manuscript preparation.
- Paper II First author. Methodology. Design of experiments. Conducting experiments. Data analysis. Discussion of the results. Manuscript preparation.
- Paper III First and corresponding author. Design of experiments. Conducting experiments. Data analysis. Manuscript preparation.
- Paper IV First author. Methodology. Design of experiments. Conducting experiments. Data analysis. Discussion of the results. Manuscript preparation.



## Introduction

Additive manufacturing (AM) is an advanced technique used to manufacture objects, and numerous AM processes have been developed over the last two decades. Laser powder-bed fusion, commercially known as selective laser melting (SLM), is a widely used AM process that enables fabrication parts with a high resolution of features and high-dimensional control. This process can manufacture parts from different materials, such as Fe-, Al-, Ti-, Ni-, Co- and Cu-based alloys; and high entropy alloys (HEAs).

To be processed by SLM, metallic alloys must fulfil certain criteria, such as possessing adequate weldability and crack formation resistance, and exhibit different technology readiness levels (TRLs). Among these metallic alloys, Ti6Al4V alloys have been extensively studied in the context of AM and have shown excellent specific strength, corrosion resistance, high thermal stability ( $\sim 350$  °C), and promise for diverse industrial applications. In addition, HEAs, a recently developed class of alloys, have attracted considerable research interest owing to their unique properties, such as excellent mechanical strength even at elevated temperatures (up to 600 °C); and excellent resistance to oxidation, wear, and fatigue. HEAs can be used as thermoelectric, radiation-resistant, and soft magnetic materials and are potential candidates for various industrial applications, including hydrogen storage and electromagnetic shielding.

SLM manufacturing from atomised commercial powder substrates is relatively costly, time-consuming, resource-demanding, and requires considerable expertise, among other challenges. The in-situ alloying of powders using SLM can address the issues associated with the requirement of pre-alloyed commercial powders, providing high flexibility and reducing energy wastage. However, in-situ alloying with a large fraction of elements could result in inhomogeneous distributions or unalloyed elements. Laser remelting strategy could reduce the inhomogeneity in SLM.

The use of SLM is advantageous in the fabrication of objects with a high resolution of features, high-dimensional control. However, SLM is a complex process with a large number of non-transferable process parameters ( $>130$ ), all of which significantly influence the quality of the final part. The parts fabricated by SLM exhibit poor performance under cyclic loading, anisotropy and inhomogeneity in microstructural and mechanical properties, defects (pores and cracks), and high residual stress (RS). Although post-heat treatment can improve the reliability and quality of the SLM parts, it increases the final production cost/time and reduces their strength. In contrast, laser remelting is an affordable non-additive technique that utilises a laser beam to impart energy and remelt the material. It can be applied to homogenise the microstructural and mechanical properties and improve the reliability and quality of SLM parts.

Therefore, in this study, Ti-based and HEAs were in-situ alloyed via SLM. The aim of the present thesis is to investigate the feasibility of producing compositionally homogenous from elemental powders mixtures corresponding to the Ti6Al4V and equiatomic CoCrFeMnNi HEA using SLM with remelting scanning strategy. In situ equiatomic CoCrFeMnNi HEA from elemental powder using SLM is carried out for the first time. In addition, laser remelting was used as a tool for increasing the homogeneity of microstructure and mechanical properties of SLM parts from pre-alloyed and mixed elemental. Furthermore, the influence of laser remelting on the substructure; mechanical properties (tension/compression, impact, hardness, and fatigue); RS; and tribological properties of the SLM parts was investigated.

## List of abbreviations

A	Fracture strain
AM	Additive Manufacturing
ASTM	American Society for Testing and Materials
BCC	Body-centered cubic
CAD	Computer aided design
CoF	Coefficient of friction
DM	Double melting
E	Young's modulus
EDS	Energy dispersive X-ray spectroscopy
FCC	Face-centered cubic
GA	Gas-atomization
HCF	High-cycle fatigue
HCP	Hexagonal closed-packed
HE	High entropy
HEA	High entropy alloys
HV	Hardness Value (Vicker's Hardness)
ISO	International Organization for Standardization
LCS	Longitudinal cross-section
LOF	Lack of fusion
MP	Metallurgical pore
PBF	Powder bed fusion
PDF	Powder diffraction file
RS	Residual stress
SEM	Secondary electron microscope
SLA	Stereolithography
SLM	Selective Laser Melting
SM	Single melting
TCS	Transverse cross-section
TEM	Transmission electron microscope
TM	Triple melting
TRL	Technology readiness level
UCS	Ultimate compressive strength
UTS	Ultimate tensile strength
XRD	X-ray diffractometer
YAG	Yttrium aluminium garnet
YS	Yield strength
3D	Three dimensional

# 1 Literature review

This chapter provides the theoretical background necessary for understanding the work that has been carried out in this dissertation. This chapter first describes the principle and classification of AM processes. The SLM process will be discussed in detail, followed by describing the process parameters and its shortcomings. Then, the main powder preparation techniques for SLM and their advantages and disadvantages will be explained. Finally, the general background of the Ti6Al4V alloy and CoCrFeMnNi HEAs fabricated by SLM, including their microstructural and mechanical properties, will be discussed.

## 1.1 Additive manufacturing classification

Additive manufacturing, developed in the 1980s, is one of the most compelling emerging manufacturing technologies that can potentially revolutionise the manufacturing sector. The American Society for Testing and Materials (ASTM) has defined AM as “the process of joining materials to make objects from 3D model data, usually layer upon layer, as opposed to subtractive manufacturing methodologies” (ASTM, 2012). AM, also referred to as three-dimensional (3D) printing, is a manufacturing technique that uses computer-aided design (CAD) to build objects. Over the last four decades, AM has attracted considerable interest from both industry and academia owing to its ability to produce almost net-shaped components with complex shapes in a cost-efficient and flexible manner. According to ASTM F2792 – 12a (ASTM, 2012), AM processes are classified into seven categories based on the material properties (such as heat resistivity), strength, shape complexity, dimensional accuracy, cost, and surface quality, among other features, as summarised in Table 1.1.

*Table 1.1 Summary of additive manufacturing processes (ASTM, 2012).*

AM categories	Technology	Material	Power source
Binder jetting	Indirect inkjet printing	Polymer, ceramic, and metal powder	Thermal energy
Directed energy deposition	Laser engineered net shaping	Molten metal	Laser, electron beam
Material extrusion	Fused deposition modelling, contour crafting	Thermoplastics, ceramic slurries	Thermal energy
Material jetting	Polyjet, inject printing	Photopolymer, wax	Thermal energy, photocuring
Powder bed fusion	Selective laser sintering	Polyamides, polymer	Laser beam
	Direct metal laser sintering	Metal, ceramic	Laser beam
	Selective laser melting	Metal and ceramic	Laser beam
	Electron beam melting	Metal and ceramic	Electron beam
Sheet lamination	Laminated object manufacturing	Plastic film, metallic sheet	Laser beam
Vat photopolymerisation	Stereolithography	Photopolymer materials	Ultraviolet laser

The application of AM processes depends on the material feedstock, mechanical properties, precision, technology availability, cost, application, post-processing, and expertise. In the binder jetting process, a liquid bonding agent is selectively deposited to join the powder, and this process is used in various applications, such as prototypes, large sand-casting molds, and low-cost metal parts. The directed energy deposition (DED) method involves the use of a metal wire or powder particles as feedstock to manufacture components, and the energy source can be a plasma arc or a high-energy beam. DED fabricates parts by depositing molten material onto a component through a nozzle, and the heat source melts the material. Material extrusion involves using filaments of thermoplastic or composite material to fabricate components from compatible raw materials, including Nylon or ABS plastic. This process can be applied to produce non-functional and cost-effective rapid prototypes, with a dimensional accuracy higher than those of other AM processes. In material jetting, photopolymers or wax can be used as feedstock to manufacture components from multi-materials with high dimensional accuracy and a very smooth surface finish. Powder bed fusion (PBF) is an advanced AM technique wherein a high-energy beam (laser or electron beam) consolidates material in powder form to fabricate objects in a layered-wise manner. In PBF, powder particles are first spread over a platform and then selectively melted by a high-energy beam. Sheet lamination, which offers high speed, low cost, and ease of material handling, involves fabricating parts from metallic sheets using ultrasonic waves and mechanical pressure for bonding. However, this process may require post-processing to improve the quality of the parts, and the materials that can be used in this process are limited. In vat photopolymerisation, a liquid photopolymer in a vat (or tank) is selectively cured by an ultraviolet heat source layer by layer to form a 3D object. This process has high accuracy, high speed, and the possibility to fabricate large objects with high quality.

## **1.2 Selective laser melting process**

The SLM process is one of the most used AM techniques and uses a laser beam to selectively melt the powder particles in a layered-wise manner, which can produce net-shape metal objects with complex geometries. In the SLM process, particles are melted completely along the laser tracks to bond them with the adjacent tracks and the precedent layer. Therefore, this process can fabricate nearly fully dense parts with high design freedom for various industries, including automotive, aerospace, medical, tooling, and energy.

Figure 1.1 illustrates the SLM process. First, a 3D model of the object is created using CAD software. Then, the model is sliced into thin layers. The designed object is fabricated on a metallic substrate plate, which can move up and down. The powder bed in the SLM process is formed by pre-spreading powder particles homogeneously over the platform or a previously solidified layer from the container stores according to the dosage level set on the machine. The laser beam scans the powder particles according to the SLM process parameters and selectively melts the powder particles into the desired shape under a protective gas (argon, nitrogen, or helium). After scanning the layer, the platform is lowered as dictated by the programmed layer thickness. Powder particles are again spread over the platform and melted on top of the former layer. This process is repeated for each layer of the CAD model until the object is fabricated. Finally, the remained powder particles will be collected and may be used again.

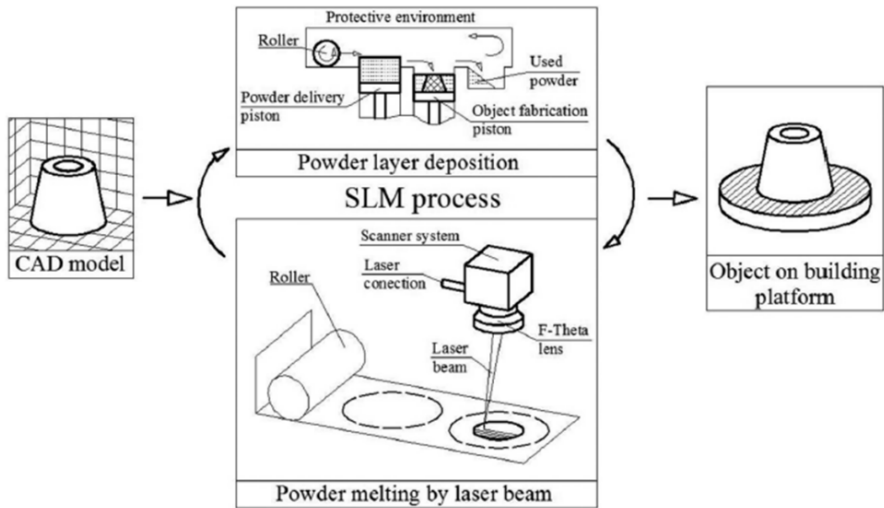


Figure 1.1 Schematic diagram of SLM process (adopted from (Doubenskaia, 2016)). Note that the designed object is fabricated layer by layer.

The SLM process is arguably one of the most successful AM processes. Different classes of material can be processed, including Al-, Ti-, Ni-, Fe-, Cu-, and Co-based alloys, and other classes of materials such as metallic glasses and HEAs (Wu, 2018). In addition, due to a very high cooling rate of the SLM process, the fabrication of amorphous materials is also possible. Moreover, the mechanical properties of the alloys can be controlled by adjusting the SLM process parameters, such as hatch style and preheating of the platform. These process parameters can influence the microstructure of the fabricated parts. However, the total manufacturing costs of the SLM process is relatively high, and the size of the build chamber of the SLM process is a manufacturing restriction. Currently, there is a rigorous quest to improve the quality and performance of SLM components.

**SLM process parameters:** SLM process parameters play a significant role in the physical and mechanical properties of fabricated parts and improper selection of these parameters can result in poor mechanical properties or defects, such as high surface roughness, deformation, and pores. Numerous studies have investigated the effect of process parameters on the quality of the final parts. Different strategies have been used to optimise the process parameters and, consequently, to improve microstructural and mechanical properties, dimensional accuracy, and surface quality. The main process parameters are, as follows.

1. **Laser wavelength:** The laser wavelength affects material absorptivity and, consequently, the total amount of energy required to melt the powders. Boley et al. (2016) reported significant variation in the absorptivity of different metals. SLM machines with a fibre laser typically have a laser wavelength of  $1.06 \mu\text{m}$ , where the absorptivity of the laser at room temperature ( $\sim 25^\circ\text{C}$ ) is very low.
2. **Spot size:** The spot size or laser beam diameter defines the size of the melt pool and affects the properties (such as density) of the fabricated parts. One way to increase the build rate of SLM is to increase the laser power that allows for a larger laser spot size, resulting in a larger melt pool size, higher layer thickness, and larger hatch spacing.

3. **Laser power:** The power of the laser is a key SLM process parameter that controls the amount of energy absorbed by the powder material. Laser power determines productivity, density, and the microstructural and mechanical properties.
4. **Scan speed:** The scan speed plays a vital role in the final product and by increasing the scan speed, the time of laser energy transfer is decreased, resulting in cracks and porosity. The scan speed affects the maximum melt pool temperature, cooling rate, density, and mechanical properties (Chen, 2019).
5. **Scanning strategy:** The scanning strategy is the geometrical pattern followed by the laser beam, which has an influence on the mechanical properties, RS, and surface quality (Ali, 2018). In addition, the scan strategy can improve the surface roughness, mechanical properties, and lower the porosity (Carter, 2014; Larimian, 2020; Rashid, 2017).
6. **Layer thickness:** Layer thickness is a measure of the height of each successive powder layer. Increasing the layer thickness decreases the total build time and production cost. Layer thickness affects productivity, surface quality, mechanical properties, and density (Alfaify, 2019).
7. **Hatch distance:** Hatch distance or scan spacing is the distance between two consecutive laser beam tracks. It determines the productivity of the SLM process and the extent of defect formation. In addition, the hatch distance influences the mechanical properties, surface quality, density, and RS.

**Challenges associated with SLM process:** The SLM process offers a great advantage in fabricating objects with complex geometry. However, it exhibits a large number of challenges due to its complex nature, which requires a comprehensive understanding of the process to fabricate parts with desirable properties. Some of these challenges are discussed in this section.

### 1. Scores of process parameters

SLM is a complex process with a large number of process parameters that have a large influence on the quality of the final part. Yadroitsev (2009) reported that there are more than 130 parameters that could affect the quality of the fabricated part. To examine the effect of these parameters or compare the input energy of the processes, energy density  $E_d$  ( $J/m^3$ ) has been used, which is defined as follows:

$$E_d = \frac{P_{eff}}{v_s h d} \quad 1.1$$

where  $P_{eff}$  is the effective laser power (W),  $h$  is the hatch distance (m),  $v_s$  is the scan speed of laser (m/s), and  $d$  is the layer thickness of the powder bed (m). However,  $E_d$  in SLM process parameter optimisation is a contentious definition, because it may also require considering the melt pool size, properties of the precursor powder (particle size, thermal conductivity, heat capacity, latent heat of fusion, etc.), laser parameters (laser type and mode, spot radius, etc.), scanning strategy, oxygen concentration during the processing, etc. Therefore, it is essential to optimise the SLM process parameters in order to fabricate components with the required properties and different methods can be used to design the experimental setup, including response surface methodology, Taguchi robust design methods, direct optimisation, optimal design of experiments, and energy density ( $E_d$ ) (Khorasani, 2019; Nguyen, 2020).

## **2. Transferring process parameters**

In a complex AM process such as SLM, transferring the optimised process parameters for a particular material among different machine manufacturers may not be possible. In SLM, scores of process parameters influence the properties of the finished part. The machine type and manufacturer, maintenance condition, protective gas flow, and other consumables can be different. The laser beam may degrade and depolarise during that time, which can affect the final quality. The geometry of the SLM component and powder material are not constant, which affect the process. Despite all the developments and improvements, the SLM process is still a trial-and-error experience-based activity. It is vital to improve the reliability and repeatability of this process.

## **3. Surface roughness**

The surface roughness of the 3D net-shape parts fabricated by SLM is relatively high and might be attributable to the turbulence of the melt pool that caused the uneven solidification and partial melting of powder particles. It has been reported that surface roughness can reach  $\sim 12\ \mu\text{m}$ , which is considerably higher than that of machined parts (Jamshidi, 2020). Numerous studies have reported the effects of scanning strategy, post-processing, powder particle size, building direction, and laser power on the surface topography. Eyzat et al. (2019) reported that the application of post-treatment (e.g., heat treatment, polishing, sandblasting, and chemical etching) could reduce the surface roughness. However, post-surface treatments are time-consuming and resource-demanding. Furthermore, Han et al. (2019a) stated that surface roughness improved with the application of laser remelting. Chen et al. (2018) reported that the fabricated SLM parts exhibited orientational dependence on surface topology, which influences the contact and mechanical properties. High surface roughness affects the functional properties of the material, frictional behaviour (especially for biological applications), and optical properties. In addition, the high surface roughness of the parts leads to a considerable reduction in fatigue strength.

## **4. Porosity**

During SLM, there is not sufficient time for conductive homogenisation of the laser input energy, and the heat is not distributed evenly in the loose powder bed. Therefore, pores can be formed that can be categorised into two types: lack of fusion (LOF) and metallurgical pore (MP). LOF pores have an irregular shape, which can form because of improper SLM process parameters. MPs are spherical in shape and can form owing to the presence of adsorbed/entrapped gases. Pores have distinct influences on monotonic and cyclic mechanical properties, which may cause SLM parts to fail prematurely.

## **5. Cracking**

Cracking is a highly complex phenomenon that may occur above the solidus temperature as a result of thermal stresses/strains, which are generated because of solidification shrinkage and thermal contraction. If the liquid phase (in the form of films) separating the grain boundaries and sufficient thermal strains are present, cracking occurs at the grain boundaries. In the rapid heating/solidification of the SLM process, the reason for cracking can be categorised into two types: (1) metallurgical factors, including solidification temperature range, amount and distribution of liquid during solidification, ductility of solidifying metal, the surface tension of grain boundary liquid, grain structure and solidification phase, and (2) mechanical factors, such as contraction stresses, degree of restraint, and geometry.

## **6. Laser absorptivity**

Laser absorption is one of the most important phenomena with a complex nature in the SLM process that influences efficiency and reliability. Laser light irradiates the loose powder and melts the material, which then rapidly solidifies. Laser absorption is the main physical phenomenon in SLM, where the reflectivity of most metals is high. The laser absorption of the loose powder is influenced by many parameters, including the wavelength and power of the laser, powder particle size (cooperation number), powder bed morphology, temperature of the melt pool, angle of incidence, surface roughness, and powder-surface chemistry. Yang et al. (2010) have developed a model to measure the laser absorptivity on the top surface of the Ti6Al4V components.

## **7. Impact strength**

The impact strength of AM parts is poor. Many studies have reported that the impact strength of parts fabricated by SLM is relatively lower than that of their wrought counterparts due to high porosities and large amounts of absorbed oxygen (Yasa, 2010). Grell et al. (2017) studied the effect of building orientation, hot isostatic pressing (HIP), defects (pores), and powder oxidation on the Charpy impact energy of Ti6Al4V parts fabricated by electron beam melting (EBM) and reported that the impact toughness increases with HIP and with a decrease in oxidation.

## **8. Anisotropy**

Anisotropy, i.e., the property of a material exhibiting directionally dependent features in mechanical properties, is one of the major issues facing AM technologies. Anisotropy in the mechanical properties of SLM parts can be influenced by anisotropy in microstructure, crystallographic texture, and spatial distribution of defects concerning the build direction. A large number of studies have reported that the effect of building orientation influences mechanical properties, including tensile, compressive, and fatigue strength (Tridello, 2020; Simonelli, 2014). In addition, it has been reported that the parts fabricated in a horizontal orientation exhibit lower strength than those fabricated vertically.

## **9. Inhomogeneity**

Inhomogeneity is defined as non-uniformity in the features of fabricated parts. In the SLM process, each volume of the material within a deposition layer experiences a different thermal history. The microstructure variation in a SLM part may lead to local variability in mechanical properties. Yang et al. (2010) studied inhomogeneity in the microstructure of as-built SLM (as-SLM) Ti6Al4V alloys using X-ray diffraction (XRD) and scanning electron microscopy (SEM) and observed distinct changes in constituent phases under specific SLM conditions. In addition, numerous studies have reported the effect of heat treatment on the homogenisation of the SLM parts and found a decrease in inhomogeneity (Cao, 2021; Zhang, 2019).

## **10. Residual stress**

In the SLM process, very high-temperature gradients, rapid phase transformation, and rapid solidification lead to the cyclic thermal expansion and contraction of the material, and, consequently, RSs form in the parts. These stresses could lead to crack formation, delamination, or accelerated in-service fatigue failure. The formation of RSs in the SLM parts depends on process parameters (e.g., powder bed temperature and scanning strategy), materials properties (e.g., thermal expansion and Young's modulus), geometry,



support structures, etc. A large amount of studies have reported that the RSs of SLM parts can be removed through the application of a heat treatment process (Shiomi, 2004; Jiang, 2019).

### **11. Cost**

The manufacturing costs of the SLM process are relatively high compared to other processes due to a low build rate. The cost of the SLM machine is quite high, which constitutes a major fraction of the total cost. SLM parts exhibit poor surface quality, which necessitates post-treatment, increasing the final production cost. Furthermore, the production cost of metallic powder particles is quite high, requiring high-quality spherical powders with good flowability, appropriate particle size distribution, and low oxygen content. The total cost of equipment, labour, energy consumption, protective gas, and the pre- and post-processes are high. Liu (2017) developed cost models for the SLM process and investigated the influence of factors such as production volume and raw material price. Powder production cost greatly influences the total cost of SLM and will be discussed in detail in Section 1.4.

### **12. Reliability**

AM parts are considered unreliable, and their fatigue behaviour has been extensively investigated using SLM (Kumar, 2020; Günther, 2017; Cao, 2017; Fotovvati, 2019; Masuo, 2018; Sangid, 2018). Due to the presence of defects and high RSs, SLM parts exhibit inferior performance under cyclic loading compared to that of their wrought counterparts (Sangid, 2018), limiting their application. It has been reported that cracking is mainly initiated by the presence of defects, such as LOF pores and/or MPs (Cao, 2017; Günther, 2017; Masuo, 2018). However, post-processing strategies such as heat treatment and HIP can be applied to reduce the number of LOF pores and MPs and, consequently, improve the fatigue life (Yasa 2010).

## **1.3 Production of metal powders**

In powder-based fusion processes such as SLM, metal powder particles are used to fabricate components. There are various technologies for metal powder production, as shown in Figure 1.2. The produced metal powder particles can be characterised by particle morphology, i.e., shape (irregular or spherical), surface roughness, and size (Sutton, 2016). Table 1.2 lists the diameters of the powder particle produced through various techniques. Furthermore, the production methods influence the physical properties of the powder particles, such as chemical properties (reactivity and impurities), flowability, porosity, density (apparent and tapped), compressibility, and cost.

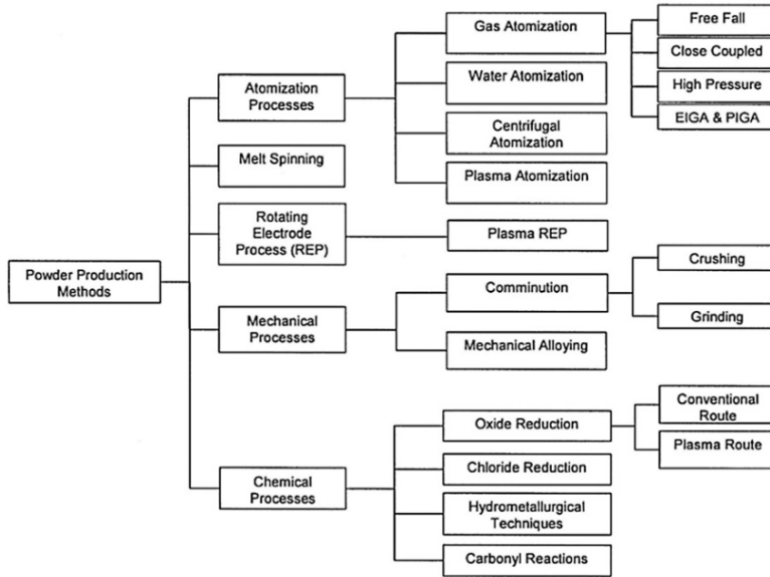


Figure 1.2 Methods of powder production (adopted from (Singh, 2017)).

Table 1.2 Powder particles diameter produced by the techniques given in Figure 1.2 (adopted from (Antony, 2003)).

Process	Powder particle diameter ( $\mu\text{m}$ )	Powder
Gas atomisation (GA)	60–125	Ni, Ti, Zr, Ti-Al, Fe-Gd, Zn, Pb
Water atomisation (WA)	12–16	Fe and Cu
Centrifugal atomisation	7–8	Al-20Si
Plasma atomisation (PA)	40–90	Ti, Mo, Cu, IN 718 (Nickel superalloy)
Plasma rotating electrode process	75–200	1018 steel
Stamp mill, ball mill	25–500	Al, Cu
Oxide reduction	1–10	Fe, Co, Cu, Mo, Al, Mg
Carbonyl reactions	10	Fe, Ni
Hydrometallurgical techniques	1–10	Ni

**Powder atomisation:** The vast majority metal powders used in AM are produced by atomisation processes, which generally show reliable and repeatable results. In SLM, powder characteristics have significant influences on the properties of the final AM part. To produce powder particles using atomisation processes, molten metals are broken into either small liquid drops by high-speed fluids (including gas and water) or fluids with

centrifugal force. The molten drops are then solidified into powder particles. Gas (GA) and plasma (PA) are two main atomisation processes.

The GA process is the main process to produce high-purity powders of a wide range of materials for SLM and it uses high-purity inert gases (e.g., nitrogen, argon, or helium). In the GA process, the metal is usually melted using gas and the molten metal is atomised using gas jets. Figure 1.3a shows a schematic of the GA process. A stream of molten metal is hit by an inert gas jet and nebulised into droplets that are cooled down (with a cooling rate of  $\sim 10^5$  K/s) during their fall in the atomisation tower. The process takes place inside an atomisation tank, which is filled with inert gas. The particles obtained by GA are usually spherical (Fig. 1.3b). However, satellite particles can be formed due to considerable interactions between droplets while they cool in-flight in the cooling chamber. In addition, the inert gas can be entrapped in the powder particles, resulting in porosity. A higher gas flow rate for a certain metal flow rate results in finer powder particles.

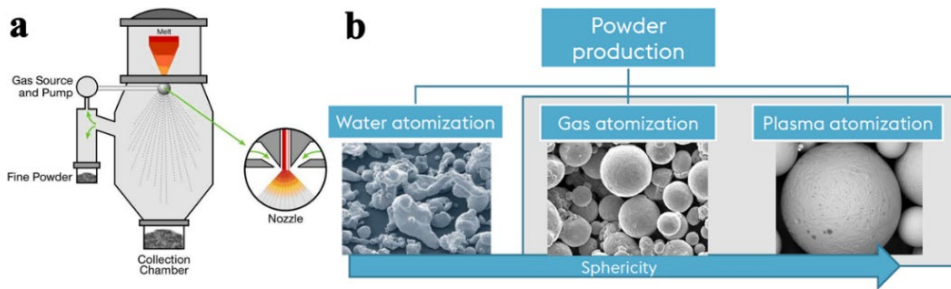


Figure 1.3 **a** Schematic of the GA process (adopted from (Matsagopane, 2019)). **b** Typical morphology of metal powder particles produced by atomisation processes (adopted from (Wallner, 2019)).

PA can be used to fabricate metal powders with premium-quality spherical powders, flatter surface textures, and minimal satellite content. The flowability and packing properties of powders fabricated using PA are better than those of powders fabricated using other atomisation methods. In PA, metal wire is melted in a plasma torch, and a plasma flow breaks up the liquid into droplets. The cooling rate is in the range of 100–1000 K/s, and powder particles are formed. PA can produce powder particles of reactive and high-melting-point materials such as Ti-, Ni-, Ti-, Zr-, Mo-, and W-based alloys. The cost of powder production via PA is significantly higher than that of powder production via GA and water atomisation (WA). It should be noted that WA has limitations in producing particles of reactive metals and alloys, and that the resultant powders typically exhibit poor quality due to irregular shape, poor flowability, and very high oxygen content.

**Powder modification for SLM:** The atomised powders, particularly GA and PA powders, exhibit important advantages, including extremely narrow chemical tolerances and spherically shaped powders with a wide particle size distribution range. In processes involving rapid solidification and the fabrication of complex objects, there are certain limitations related to materials that can be used for the SLM process. A few of the major disadvantages are the following.

- 1. Limited number of available commercial alloys:** In the SLM process with the possibility of the fabrication the most complex objects, the compositional flexibility of the material is restricted. Moreover, certain alloy powders can be

challenging to produce via the atomisation processes due to quality or chemical composition issues.

2. **High cost of production:** The number of metallic powder manufacturers on the market is limited, and the large size of the minimum batch sizes available causes an inflated total price. Furthermore, the powder particle size and morphology requirements for SLM cause an increase in cost (Dong, 2021).
3. **Time-consuming processes:** The production of pre-alloyed powders using atomisation processes is a time-consuming and resource-intensive procedure. Powders are usually produced from alloy ingots that are melted and then atomised. However, a new atomisation processes that uses a mixture of sponge and master alloy has been described by Arimoto et al. (2006).
4. **Required expertise:** Producing powder particles via atomisation processes, particularly PA, requires specific expertise to meet the commercial requirements of customers. The manufacturer should have the ability to control the chemical composition and particle size, as well as consistency within production batches, and only experienced manufacturers are able to fabricate high-purity spherical metal powders with narrow particle distributions.
5. **Other issues:** In brief, powders of some alloy compositions can be challenging to produce via atomisation because of the issues associated with quality or chemical composition. Similarly, powder of alloys that contain elements with large differences in physical properties, such as the melting point or weldability, are difficult to produce via atomisation.

Therefore, developing material for SLM through the (gas) atomisation process is difficult, and there is a need for a flexible alloying procedure. In processes with rapid solidification, such as SLM, materials with different microstructures, phases, and, therefore, physical and mechanical properties can be obtained. Tailoring the chemical composition of alloys in SLM will result in a material with new microstructural and mechanical properties. A plausible solution to the aforementioned problems is to use mixed elemental powders as feedstock to fabricate SLM parts, which is commonly known as in-situ alloying. This technique has made a significant contribution to the development of different alloy systems and offers low production costs and, in addition, can be used instead of purchasing large batches of metal powders of fixed composition. In-situ alloying allows mixing the elemental powders in desired weight or atomic percentage and, consequently, overcoming the limitation in compositional flexibility and availability. A large number of studies have reported successfully in-situ alloying of elemental powder (Dong, 2021; Simonelli, 2018; Vora, 2017; Vora, 2015). Materials produced by SLM from the mixture of elemental powders must be assessed for homogeneity in chemical composition and microstructure, mechanical properties, and defects such as porosity and cracks (Brodie, 2020). Figure 1.4 shows the morphology and chemical composition of a powder mixture, suggesting the homogeneous distribution of powder particles after powder mixing.

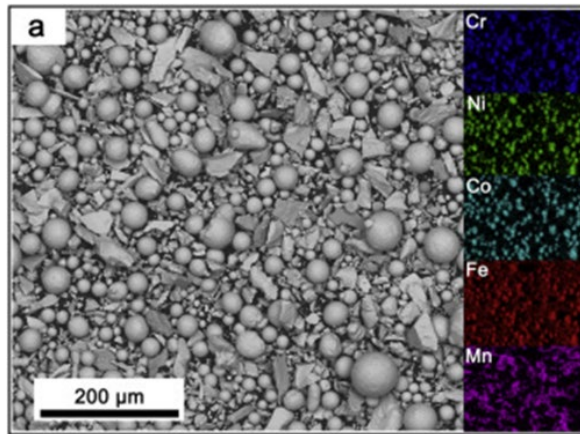


Figure 1.4 SEM image of the blended powder including spherical pre-alloyed CoCrFeNi and irregular-shaped elemental Mn powders, with energy-dispersive X-ray spectroscopy (EDS) mapping (modified from (Chen, 2020b)).

In-situ alloying by SLM can circumvent the consumption of a large amount of pre-alloyed materials and resource wastage. Materials with unique printability, microstructure, phase, and physical and mechanical properties, can be manufactured using in-situ alloying.

#### 1.4 SLM of metallic alloys

The SLM process has been highlighted for its unique advantages in fabricating complex components from metallic alloys in comparison with other fabrication processes. However, the metallic alloys that can be processed by SLM must fulfil certain criteria, such as adequate weldability. According to ISO standard 581-1980, weldability is the capacity of a metal to be welded via a given process for a given purpose, providing integrity to the product and meeting technical requirements. The alloys should resist crack formation, which can appear because of a broad solidification temperature range, low ductility, high surface tension of the grain boundary liquid, coarse columnar grains structure, and RSs (Gorsse, 2017).

Different classes of materials with available GA powder, such as Al-, Co-, Ni-, Fe-, Cu-, Cr-, Ti-based alloys, HEAs, and quasicrystalline materials, can be processed by commercial SLM applications and exhibit desirable properties (Paper I). The SLM process has the capability of easily adjusting process parameters for new generation alloys that are difficult to fabricate using other AM techniques. Table 1.3 lists the most popular alloys for the SLM process. Ongoing research on material development and properties is of interest to the field of material science, which can be applied to various industries.

Table 1.3 Common materials available for SLM.

Material class	Alloy composition	TRL	References
Al-based alloys	AlSi10Mg, AlSi7Mg0.6, AlSi9Cu3, 1050A, 2017A, 2219, 6061, 7020, 7050, 7075, 5083	4–8	(Gorsse, 2017)
Ti-based alloys	Ti6Al4V ELI (Grade 23), TA15, Ti (Grade 2)	7–9	(Gorsse, 2017)
Ni-based alloys	HX, IN625, IN718, IN939	7–9	(Gorsse, 2017)
Co-Cr alloys	CoCr28Mo6, MediDent (CoCr)	7–9	(Gorsse, 2017)
Cu-based alloys	CuNi2SiCr, CuSn10, CuCr1Zr	4–5	(Gorsse, 2017)
Fe-based alloys	316L, 15-5PH, 17-4PH, maraging tool steel, H13, Fe-alloy Invar 36	7–9	(Gorsse, 2017)
High-entropy alloys (HEAs)		1–3	(Hern, 2021)

Currently, only a small number of metallic alloys (approximately >50 alloys (Gorsse, 2017)) can be processed by SLM with different TRLs. The TRL was developed as an estimate of the maturity or readiness of a new technology based on nine levels, according to NASA (Peters, 2015). Various industries, including the manufacturing, automotive, and energy sectors, are using the TRL to evaluate the quality of a new technology. Numerous studies have investigated the AM of materials to improve the available materials or expand the variety of compatible materials. In this work, two alloy classes, namely, Ti-based and HEAs, were selected to address the limitations of SLM and span the maturity or TRL of materials. As summarised in Table 1.3, these two classes of materials have different TRLs.

Ti-based alloys have been extensively studied in the context of AM. Results have indicated that ~35% of scientific publications concern Ti-based alloys, with alloys fabricated by AM exhibiting lower fabrications costs than their wrought counterparts. Ti-based alloys have been used in biomedical and aerospace applications, lightweight structural components, and the research and development sector. Ti-based alloys are typically classified into  $\alpha$ - and  $\beta$ -Ti alloys. Among various Ti-based alloys, Ti6Al4V is the most widely used, accounting for almost half of the market share of Ti products currently in use (Paper III). Ti6Al4V has excellent specific strength, corrosion resistance, and adequate thermal stability (~350 °C).

HEAs (material with at least five principal elements) will be investigated. Since the development of HEAs, research has been accelerated due to their interesting properties (Paper IV). HEAs have considerably higher entropies than traditional alloys, exhibit good mechanical strength even at elevated temperatures, and can be used as thermoelectric, hydrogen storage, radiation-resistant, electromagnetic shielding, and soft magnetic materials. AM was successively applied to manufacture HEA parts, which offers the additional advantage of producing parts with intricate shapes and added functionalities. In the following sections, Ti-based and HEAs and the properties of AM parts using SLM will be discussed in detail.

In-situ alloying by the SLM process is attracting increasing attention from researchers and engineers. The cost of the mixed elemental powder particles is almost an order of magnitude lower than that of commercial atomised powders, suggesting a significant improvement in the affordability. Figure 1.5 illustrates the price of the commercial GA

and mixed elemental Ti6Al4V and CoCrFeMnNi HEA powders. The GA powders are considerably costly, over \$430 per kg for Ti6Al4V (Dong, 2021) and \$550 per kg for HEAs (Sarswat, 2020). In contrast, the cost of the mixed elemental powders that were used in the present work are significantly lower at approximately \$35 and \$55 per kg for Ti6Al4V and CoCrFeMnNi HEAs, respectively. Owing to the low alloying concentrations in Ti6Al4V alloys, the cost of the Ti6Al4V powder mixture is close to that of pure Ti powder. Dong et al. (2021) reported that the Al (6 wt%) and V (4 wt%) increase the feedstock cost by ~\$3 and ~\$11 US per kg, respectively.

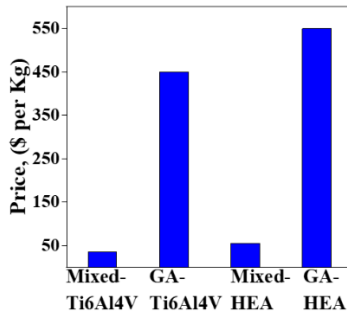


Figure 1.5 Price comparison of commercial GA and mixed elemental Ti6Al4V and CoCrFeMnNi HEA powders.

#### 1.4.1 SLM Ti6Al4V alloys

Ti6Al4V alloys, which were introduced in 1954 in the USA, are an  $\alpha + \beta$  Ti alloy with high specific strength, low density, desirable tribological properties, high fracture toughness, excellent corrosion resistance, and remarkable biocompatibility. These alloys have applications in diverse industries, such as defence, marine, automobile, energy, chemical, and biomedical. Ti6Al4V refers to pure Ti with 6 wt% Al ( $\alpha$  stabiliser) and 4 wt% V ( $\beta$  stabiliser). Ti6Al4V exhibits both  $\alpha$  and  $\beta$  phases, depending on the thermal processing of the material. At high cooling rates (above 410 K/s), the  $\alpha'$  martensite phase is formed, whereas at low cooling rates (above the  $\beta$  transus temperature), the globular  $\alpha$  phase is formed (Warren, 2018).

The SLM process, which can produce almost-net-shape structures with complex geometries via a flexible layer by layer control strategy, has attracted the attention of researchers and engineers for fabricating Ti6Al4V parts. The SLM processing of Ti6Al4V parts involves the melting of powder in small volumes on previously solidified layers. Therefore, it requires a high solidification rate. The as-SLM Ti6Al4V alloys consist of the acicular  $\alpha'$  martensite phase because of the very high cooling rate associated with the SLM process, resulting in high tensile strength and hardness. However, the fabricated parts exhibit poor ductility and reliability (Al-rubaie, 2020; Eyzat, 2019; Kumar, 2020; Li (Z.) 2018; Vaithilingam, 2016; Vrancken, 2014; Yasa, 2011). Yang et al. (2016) investigated the patterns of influence of process parameters of the SLM process, such as scan speed and hatch distance, on the size of the martensitic phase and its formation mechanisms. They found that the size of the martensitic phase could be controlled by the SLM process parameters and that the hierarchical microstructure of acicular  $\alpha'$  martensite is a result of the thermal cycles of SLM. However, the parts fabricated by SLM exhibit poor performance under cyclic loading, anisotropy and inhomogeneity in microstructural and mechanical properties, and defects (pores and cracks).

### 1.4.2 SLM of HEAs

Since the Bronze Age, the design of alloys has been based on one or two principal elements, such as Fe in steels or Ni in superalloys, and a minor alloying approach is applied to adjust the microstructure and properties. Recently, a new class of multicomponent alloys was introduced, denoted as HEAs by Yeh et al. (2004, 2007). Their disordered solid-solution structures are stabilised by a high configurational entropy of mixing ( $\Delta S_{\text{conf}}$ ) because of the addition of multiple elements (five or more) in an equimolar or near-equimolar composition (with an atomic percentage between 5% and 35% (Yeh, 2004)). For alloy development, scientists focused on a limited number of principal elements because of the complex multidimensional phase diagram of a multicomponent alloy system. A large number of metastable/intermetallic phases can be formed, which could decline the mechanical properties. Over the past two decades, this new class of alloys was developed significantly, and a large volume of work was carried out to improve their microstructural and mechanical properties. It is possible to tailor the properties by the proper selection of component elements (Chen, 2020a; Melia, 2019; Schneider, 2018; Wang, 2017; Yeh, 2007). These superior properties of HEA are related to the so-called “core effects” in such multi-principal-element design: high entropy, sluggish diffusion, severe lattice distortion, and the cocktail effect. A large number of studies have implied the potential for discovering new materials with valuable properties in the uncharted phase-space in the middle of multicomponent systems (Lu, 2020; Huang, 2019; Mu, 2013). The difference in entropy of between HEAs solid solutions and other alloys is particularly large owing to the multiprincipal-element design (Tsai, 2014). HEAs, in particular those consisting of refractory elements, have high yield strength at a high temperature. On the other hand, the yield strength of superalloys, including Inconel 718 and Haynes 230, which are generally used in gas turbine engines with operating temperatures around 800 °C, significantly decreases at a temperature just above 600 °C, as shown in Figure 1.6. Therefore, these properties motivate the wide investigation of HEAs (Senkov, 2011).

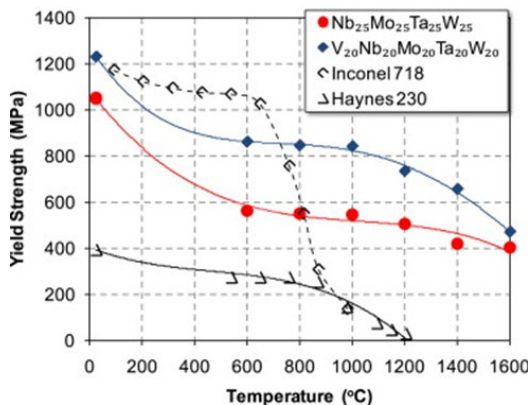


Figure 1.6 The temperature dependence of the yield strength of HEAs and the superalloys Inconel 718 and Haynes 230 (Senkov, 2011).

The CoCrFeMnNi HEA is one of the most studied HEAs with a single-phase face-centred cubic (FCC) solid solution. A CoCrFeMnNi HEA with an equiatomic composition exhibits unique properties, such as adequate high-temperature structural stability, excellent fracture toughness, corrosion resistance, and high ductility at cryogenic temperatures.



The CoCrFeMnNi HEA is a potential candidate for structural applications at cryogenic temperatures. Kilmametov (2019) reported a remarkable hardness value (~6700 MPa) for the CoCrFeMnNi HEA. Lu et al. (2020) studied the mechanical properties of the CoCrFeMnNi HEA at 550 °C and reported that these alloys exhibited adequate fatigue behaviour comparable to that of common austenitic stainless steel. Wang (2020) reported excellent corrosion resistance values for the CoCrFeMnNi HEA. HEAs have been processed using traditional manufacturing routes, such as casting (Melia, 2019), exhibiting complicated microstructure in both as-cast and annealed conditions (Munitz, 2016). The CoCrFeMnNi HEA has been fabricated by SLM using pre-alloyed powder, and the as-fabricated parts possess chemical homogenisation and excellent mechanical properties. Li (R.) et al. (2018) produced the equiatomic CoCrFeMnNi HEA using SLM from GA powder and reported increased density and surface quality with increasing laser energy density. In addition, Kim et al. (2020) reported that the CoCrFeMnNi HEA fabricated via SLM exhibited remarkable mechanical properties in the high-temperature range (up to 600 °C). Chen et al. (2020b) successfully produced an in-situ CoCrFeMnNi HEA using SLM from a mixture of CoCrFeNi pre-alloyed and pure Mn powders and reported that this HEA exhibited adequate printability and homogeneous chemical distribution. However, SLM equiatomic CoCrFeMnNi HEA from atomised commercial powder substrates is relatively costly, time-consuming, and requires considerable expertise.

## 1.5 The objectives of the thesis

SLM is one of the most widely used AM techniques that can produce the most complex objects usually from pre-alloyed powder particles. However, pre-alloyed powders exhibit significant shortcomings, such as rigid chemical composition, limited number of available commercial alloys, resource-demanding and time-consuming production process, production issues, and required expertise. In addition, the SLM parts exhibit poor performance under cyclic loading, anisotropy and inhomogeneity in microstructural and mechanical properties, defects (pores and cracks), and high RS. Therefore, the aim of the present thesis is to investigate the feasibility of producing compositionally homogeneous parts without resorting to pre-alloyed GA powders, instead of using elemental powder mixtures corresponding to the Ti6Al4V and CoCrFeMnNi HEAs. In addition, the effect of a remelting scan strategy on the alloying behaviour was studied, as well as the mechanical and microstructural properties of SLM parts. The main objectives of this thesis are as follows.

1. In-situ alloying of CoCrFeMnNi HEA in equiatomic composition by SLM from the elemental powder mixtures and compare with those fabricated from pre-alloyed GA powder.
2. In-situ alloying of Ti6Al4V by SLM from the elemental powder mixtures and compare with those fabricated from pre-alloyed GA powder.
3. To reveal the alloying behaviours, elemental distribution, microstructure, and mechanical properties of in-situ fabricated Ti6Al4V and CoCrFeMnNi HEAs.
4. To investigate the influence of remelting scan strategy on chemical and morphological inhomogeneity, and anisotropy in microstructure, and mechanical properties of in-situ fabricated Ti6Al4V and high-entropy alloys.
5. To improve the mechanical properties, including tensile/compressive strength, high cycle fatigue strength, hardness, and Charpy impact energy of SLM parts.
6. To reduce the inhomogeneity in microstructural and mechanical properties of SLM parts from GA powder.

## 2 Experimental methodology

The experimental methodology used to fabricate the parts and characterise them in this thesis is described in this chapter. The AM SLM, microstructure characterisations (TEM, SEM), mechanical tests (tension, compression, fatigue and hardness), and RS measurements were explained.

### 2.1 Gas atomized and elemental powders

Ti alloy GA powder (Ti6Al4V ELI-Grade 23) from SLM Solutions, Germany was used, containing 90 wt% Ti, 6 wt% Al, and 4 wt% V. Ti, Al, and V elemental powders used were supplied by READE, USA. Co, Fe, Mn, and Ni elemental powders were supplied by Pacific Particulate Materials, Canada. The elemental powders were blended for 12 h by a blending machine. Particle size distribution was measured using a laser particle size analyser (HORIBA LA-950) in deionised water with a refractive index of 1.3.

### 2.2 SLM system

The Ti6Al4V and high-entropy alloy bulk samples were manufactured using a ReaLizer SLM-50 unit (Germany), which can be used to fabricate objects from metallic powders, including Fe-, Al-, Co-, and Ti-based alloys. It was equipped with a 120 W Yb-YAG laser with a spot size of  $\sim 39 \mu\text{m}$ . Figure 2.1 shows the overall appearance and building chamber of the ReaLizer SLM-50 device. The desktop unit was designed for the production of components with a diameter and height of up to 70 and 80 mm, respectively.



Figure 2.1 ReaLizer SLM 50 device used for the fabrication process.

Table 2.1 lists the process parameters used in the present work. During the manufacturing of AM parts via SLM, each layer was melted either once (single melting, SM), twice (double melting, DM), or thrice (triple melting, TM) to study the influence of the laser re-scanning strategy (Fig. 2.2a). There was at least a 15 s time interval between the melting steps. In the single melting, the powder bed was melted once with the process parameters given in Table 2.1. The SLM process parameters for the Ti6Al4V and CoCrFeMnNi HEAs were optimised to increase printability and reduce pores, cracks, and lamination. During double/triple melting (or remelting scan strategy), each layer was melted two/three times, and the process parameters of SLM were kept the same.

Possible oxygen contamination during the SLM process was avoided using a constant flow of high-purity argon gas. The gas flow was kept constant for the production of all samples. The SLM parts were manufactured on a 20-mm-thick Ti6Al4V or stainless-steel platform.

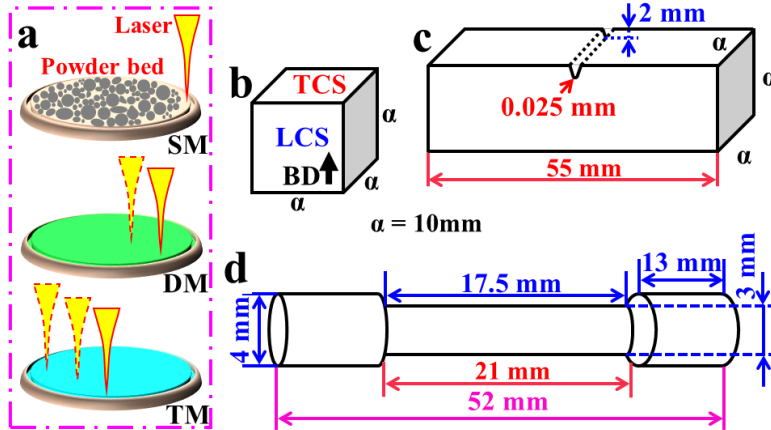


Figure 2.2 Schematic representation of the SLM samples: **a** Increasing the number of melting steps from one to three. **b** Cube with a dimension of 10 mm. **c** Charpy test specimen according to ASTM Test Method E23. **d** Tensile bar sample fabricated by SLM according to ASTM E8/E8M-13a. (adopted from (Paper IV)).

Table 2.1 The process parameters used to fabricate the Ti6Al4V and CoCrFeMnNi HEA samples using the SLM process.

Parameter	Alloys	
	Ti6Al4V	CoCrFeMnNi HEA
Laser spot size, ( $\mu\text{m}$ )	39	39
Hatch distance, ( $\mu\text{m}$ )	60	60
Hatch rotation angle, ( $^\circ$ )	73	73
Laser scan speed, (m/s)	1	1
Layer thickness, ( $\mu\text{m}$ )	25	25
Laser power(W)	60	96

The tensile/fatigue bars were manufactured using the SLM process and the specimens were polished or machined to remove the support or eliminate unmelted/partially melted powder particles (Fig. 2.2d).

## 2.3 Microstructure characterisation

### 2.3.1 Metallographic preparation

For the mounting and polishing of the fabricated SLM samples, standard metallographic practices were used. Kroll's reagent consisting of 5 mL  $\text{HNO}_3$ , 3 mL HF, and 100 mL distilled water was used as an etchant for the Ti6Al4V alloys. Aqua Regia (or royal water) comprised a 3:1 mixture of HCl and  $\text{HNO}_3$  was used as an etchant for the CoCrFeMnNi HEAs. For TEM characterisation, thin-foil samples were prepared by mechanically grinding down to 50  $\mu\text{m}$ . The microstructures of three different in-situ alloyed samples that were fabricated during three different fabrication processes were analysed.

### 2.3.2 Phase identification and microstructural characterisation

The microstructure was characterised by SEM (Zeiss FEG-Germany, and Hitachi TM1000, Tokyo-Japan), TEM (Tecnai G2 F20, FEI, Germany) coupled with energy-dispersive X-ray spectroscopy (EDS), and optical microscopy (Zeiss Axiovert 25). The structural characterisation was analysed using XRD (Rigaku SmartLab SE with a D/teX Ultra 250 1D detector and a Cu-K $\alpha$  source ( $\lambda = 1.5406 \text{ \AA}$ )). The measurements were conducted at room temperature (23 °C) from 20° to 120° (2 $\theta$ ) with a step size of a 0.04° for CoCrFeMnNi HEA and 0.01° for Ti6Al4V. The Scherer equation was used to determine the crystallite size, using the equation:

$$D = \frac{K\lambda}{\beta \cos\theta'} \quad 2.1$$

where  $D$  is the crystallite size (nm),  $\lambda$  is the wavelength of the X-ray beam ( $\text{\AA}$ ),  $K$  is the shape factor (-),  $\beta$  is the full width at half maximum of the diffraction peak (2 $\theta$ ), and  $\theta'$  is the Bragg angle (°). Lattice parameters were calculated using Bragg's law along with the plane spacing equation, as follows:

$$\lambda = 2d \sin \theta, \quad 2.2$$

$$\frac{1}{d^2} = \frac{4}{3} \left( \frac{h^2 + hk + k^2}{a^2} \right) + \frac{l^2}{c^2}, \quad 2.3$$

where  $d$  is inter-planar spacing (nm);  $a$  and  $c$  are the lattice constants (nm); and  $h$ ,  $k$ , and  $l$  are the Miller indices (-). The dislocation density,  $\rho$ , was estimated using the Williamson–Hall approach, as follows:

$$\rho = 14.4 \frac{\varepsilon^2}{b^2}, \quad 2.4$$

where  $\varepsilon$  is lattice strain (-),  $\rho$  is dislocation density ( $\text{m/m}^3$ ), and  $b$  is the magnitude of the Burgers vector. The lattice strain is obtained using the relationship:

$$\beta \frac{\cos \theta}{\lambda} = \frac{0.9}{D} + 2\varepsilon \frac{\sin \theta}{\lambda}, \quad 2.5$$

The average number and width of twins of the TEM images were measured in an area of  $\sim 100 \mu\text{m}^2$  in each sample using an image analyser software. In addition, the distribution and size of voids were measured using the ImageJ software using contrast difference measurements. The dimensions of the acicular  $\alpha/\alpha'$  martensite platelets were measured. Around 50 readings for each dimension were measured from several optical/SEM images, and only the average values are reported. Elemental distribution was tested over several zones of each sample with different magnification by the EDS. The average size, overlap zone, and inter-space of the melt pools were determined with 100, 30, and 30 measurements, respectively.

## 2.4 Residual stress measurement

The RS measurement of the SLM-fabricated parts (Fig. 2.2b) at the TCS and LCS of the sample surface was carried out using XRD (Asenware AW-XDM300, HAOYUAN) with CuK $\alpha$  radiation ( $\lambda = 1.54184 \text{ \AA}$ ) with a step size of 0.02° and time per step of 1 s. The  $\sin^2\psi$  method was used in seven angles ( $\phi$ ), including 0°, 15°, 30°, 45°, -10°, -20°, and -30°. Equation 2.6 was used to calculate the stress in the chosen direction from the inter-planar spacing, as follows:

$$\sigma_\phi = \frac{E}{(1+\nu) + \sin^2 \psi} \left\{ \frac{d_\psi - d_n}{d_n} \right\}, \quad 2.6$$

where  $\sigma_\phi$  is single stress acting in a selected direction (MPa),  $E$  is the elastic modulus (GPa),  $\nu$  is Poisson's ratio (-),  $\psi$  is the angle between the normal of the sample and that of the diffracting plane ( $^\circ$ ),  $d_\psi$  is the inter-planar spacing of planes at an angle  $\psi$  to the surface ( $\text{\AA}$ ), and  $d_n$  is the inter-planar spacing of planes normal to the surface ( $\text{\AA}$ ). Further details have been provided in the study by Fitzpatrick (2005).

## 2.5 Characterisation of physical and mechanical properties

### 2.5.1 Hardness and microhardness testing

The average hardness values were obtained from three samples with at least 12 measurements for each using a Vickers INDENTEC 5030SKV machine with a 5 kgf load and 10 s dwell time. The microhardness test was carried out over 100 indents in each sample (for the hardness maps) using a MICROMET 2001 (Buehler) machine. The homogenisation efficiency of hardness was used to quantitatively study the inhomogeneity. The hardness ranges of 450–500 and 200–250 HV were considered for the Ti6Al4V and CoCrFeMnNi HEAs, respectively, and the hardness values in these ranges are used as indicators of homogenisation efficiency. In addition, the average hardness value was calculated for each sample using 10 indentations.

### 2.5.2 Tension and compression testing

Room-temperature tensile tests were carried out on a servo-hydraulic testing machine (Instron 8516, High Wycombe, UK) with a capacity of 100 kN and a strain rate of 0.001 mm/s. The tensile bars were fabricated according to ASTM E8/E8M-13a. The dimensions of the tensile bars were modified to suit the length of 52 mm per the ratio mentioned in the ASTM standard (Fig. 2.2d). At least three samples were tested in each condition to evaluate the reproducibility of the results and the representative tensile curves are presented where necessary. The compression test was carried out at room temperature (and relative humidity of 58%) using a servo-hydraulic machine (Instron 8516, High Wycombe, UK) with a strain rate of 1 mm/min.

### 2.5.3 High cycle fatigue testing

High cycle fatigue (HCF) tests were carried out on a universal fatigue tester (Instron 8516, High Wycombe, UK) with a Track8800D controller at room temperature, a frequency of 5 Hz, a stress ratio of  $R = -1$ , and under a sinusoidal loading at different stress ranges from 100 to 700 MPa at intervals of 50 MPa (Fig. 2.2d). The HCF test was stopped when the failure occurred or when the samples survived after at least 1 million cycles. The runout specimens (i.e., the HCF test specimens that survived a stress amplitude of 100 MPa up to  $10^6$  cycles) are marked with arrows.

### 2.5.4 Charpy impact testing

The Charpy test specimens were fabricated with the mentioned SLM process parameters, as shown in Figure 2.2c. The room-temperature Charpy impact test was conducted with the Pendulum impact tester RKP 450 (Zwick, Germany) using standard V notch specimens (10×10×55 mm) in accordance with the ASTM Test Method E23. The average Charpy absorbed impact energy values were obtained from at least 3 samples for each condition. Both the vertically-oriented specimens were polished to remove support structure.

### **2.5.5 Density**

The density of the fabricated SLM samples was measured using an analytical balance based on Archimedes' principle. A Mettler Toledo ME204 was employed for the density measurement with a precision of  $\pm 0.0001$  g. In order to measure the density, each sample was first weighed in air and then immersed in distilled water for an adequate amount of time before they were weighted again, at a constant temperature. At least 10 readings for each sample were recorded and the average values are reported.

### **2.6 Tribological characterisation**

The tribological properties were investigated using a tribotester (CETR/Bruker UMT-2) under dry reciprocating sliding conditions, a frequency of 5 Hz, an amplitude of 1 mm, and a load of 0.3 N ( $\sim 30.6$  g). The test comprised five steps of 1000 s each in air at room temperature ( $25 \pm 2$  °C) with a relative humidity of  $45 \pm 5\%$ . The reciprocating sliding tests were conducted on at least three samples with zirconia balls ( $ZrO_2$ ) of  $\varnothing 3$  mm diameter and grade 10 fabricated by RGP BALLS (Cinisello Balsamo, Italy). The volume of material loss (missing net volume) was determined using a 3D profiler (BRUKER ContourGT-K0+; Bruker, Billerica, USA). To study the effect of the building direction on the tribological properties, two surface of the SLM parts were investigated: the transverse and longitudinal cross section. This information must be considered during the design of SLM Ti6Al4V parts used in different applications.

### 3 Homogenisation of SLM HEAs

#### 3.1 In-situ high-entropy alloying from elemental powders

Figure 3.1a depicts the XRD of the equiatomic mixed elemental powder particles, in which the diffraction peaks corresponding to Co, Cr, Fe, Ni, and Mn are shown. Figure 3.1b shows the distribution of the mixed elemental powder particle sizes and the cumulative volume fraction, where  $D_{10}$  and  $D_{90}$  were found to be  $\sim 8$  and  $46 \mu\text{m}$ , respectively, and most of the particles have a diameter less than  $20 \mu\text{m}$  ( $D_{50}$ ). The SEM micrograph of the elemental powders is shown in Figure 3.1c and their distribution after powder blending indicates that the majority of the particles are irregular in shape. The EDS maps of the mixed elemental powders indicate the homogeneous distribution of powder particles after powder mixing.

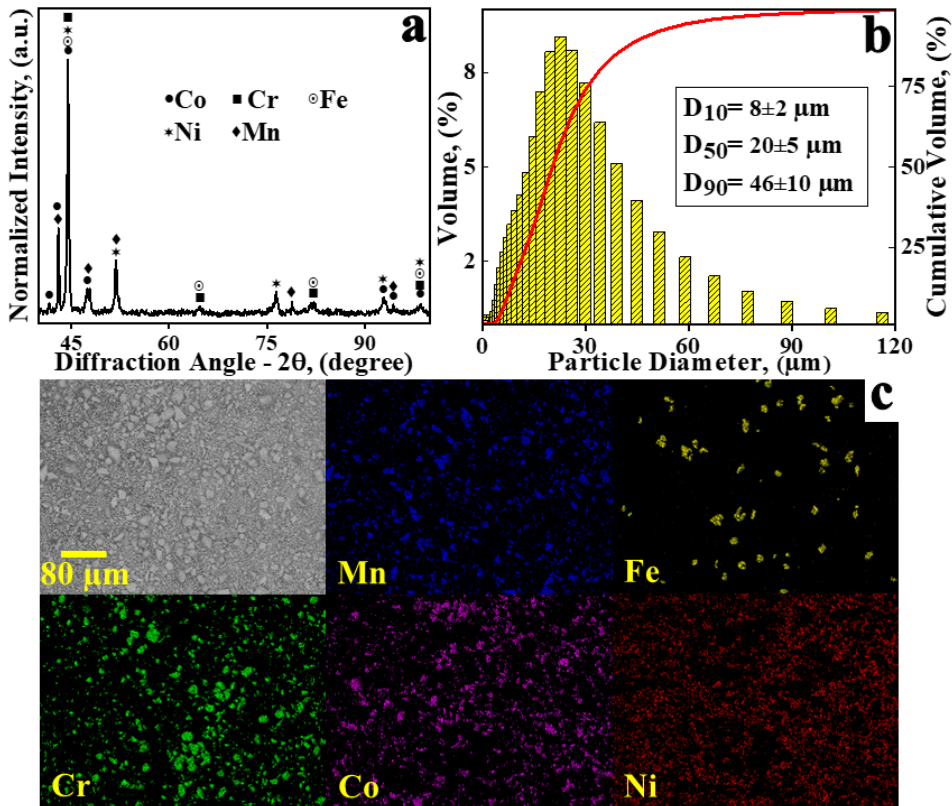


Figure 3.1 Mixed equiatomic CoCrFeMnNi powder. **a** XRD analysis, **b** Histogram showing the size distribution (volume fraction and cumulative volume fraction vs powder particle diameter), **c** SEM micrograph of the powder mixture and the corresponding EDS maps. (The powder diffraction file (PDF) cards of [PDF: 04-015-9337] for Co, [PDF: 04-016-3228] for Cr, [PDF: 00-006-0969] for Fe, [PDF: 04-016-6934] for Mn, and [PDF: 00-004-0850] for Ni were used).

Figure 3.2a and b show the XRD patterns of the samples fabricated by SLM from the mixed elemental powders taken from TCS and LCS, respectively. Both diffractograms show the presence of a single-phase FCC structure, in agreement with Melia et al. (2019). In addition, the lattice parameters were found to be  $\sim 0.3598 \text{ nm}$  for the as-built and

$\sim 0.3592$  nm for the remelted SLM samples. The value of the calculated lattice parameter of the as-SLM sample is similar to that reported by Huang et al. (2019). The crystallite size was found to be 15.3 nm and 15.2 nm for the as-built and remelted SLM samples, respectively.

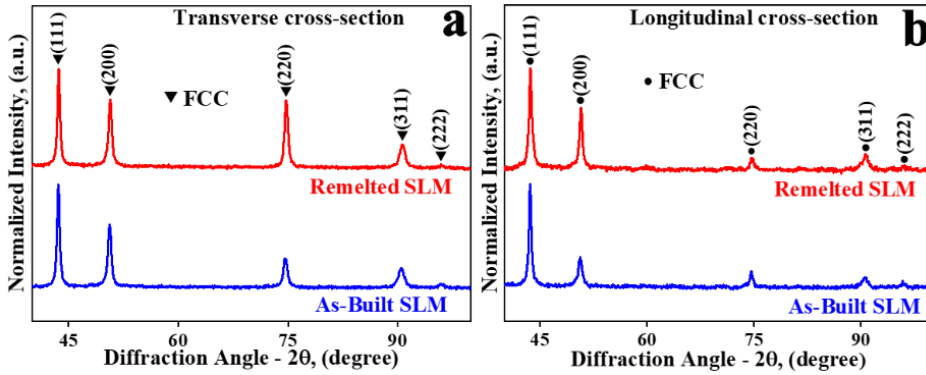


Figure 3.2 XRD diffractograms of the as-built and remelted SLM CoCrFeMnNi HEA samples obtained from **a** TCS and **b** LCS ([PDF: 00-065-0528]).

Figure 3.3a shows the TCS of CoCrFeMnNi HEA, where the laser tracks with overlapped structure can be recognized by the different angular directions, and their average width is  $\sim 40 \pm 9$   $\mu\text{m}$ . Compared to the as-SLM, it may be seen that the laser tracks are less overlapped in the TCS of the remelted SLM sample, and their average width reduces to  $\sim 36 \pm 9$   $\mu\text{m}$  (Fig. 3.3c). In addition, the average depth of the melt pool and its deviation decreased from  $\sim 34 \pm 5$   $\mu\text{m}$  for as-SLM (Fig. 3.3b) to  $\sim 24 \pm 3$   $\mu\text{m}$  for remelted sample (Fig. 3.3d).

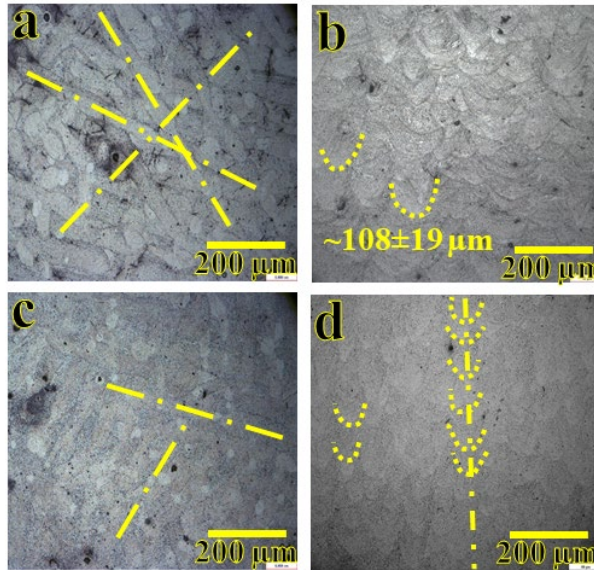


Figure 3.3 Optical micrographs of the samples from the mixed CoCrFeMnNi powder showing the microstructure in: **a** TCS and **b** LCS of the as-SLM; **c** TCS and **d** LCS of the remelted SLM. Laser tracks are indicated by yellow dot-dash lines.



In the parts fabricated by SLM, due to rapid solidification, insufficient hatch overlap (>20% of its hatch distance), low density of the loose powder (>60% for particles with a size between 15 and 63  $\mu\text{m}$ ), and a lack of homogeneous conduction of the input energy, LOF pores can appear. Furthermore, the oscillation of the melt pool surface may cause gas entrapment, which can result in MP formation. The morphologies of the pores in the TCS of the as-built and remelted SLM samples are illustrated in Figure 3.4a and b, respectively. Although the remelting of the solidified layer eliminated the LOF pores, the MPs were retained. In addition, the theoretical density of the SLM samples was found to be  $\sim 94.0 \pm 0.1\%$ .

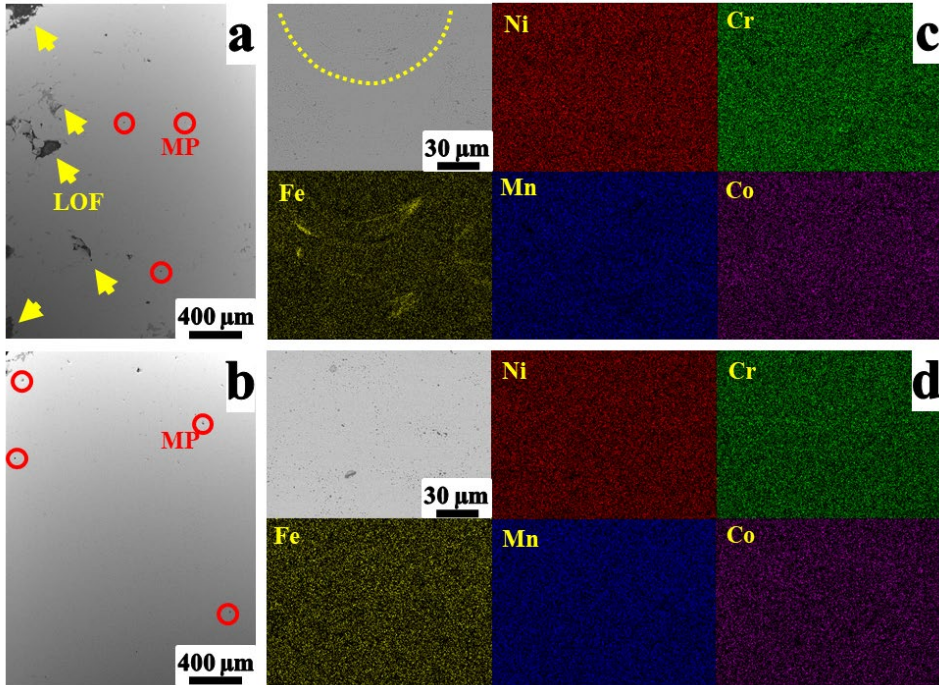


Figure 3.4 Surface porosity in TCS of **a** as-built and **b** remelted SLM CoCrFeMnNi HEA. Backscatter SEM image showing the LCS and the corresponding EDS maps of the **c** as-built and **d** remelted SLM CoCrFeMnNi HEA samples. The yellow dashed line highlights the melt pool boundary.

HEAs show elemental segregation in the interdendritic regions of the welded (Wu, 2018) or cast (Han, 2019b) parts. In a rapid solidification process, such as the SLM, no differences could be observed in the chemical composition of the inner and interdendritic regions of samples, as was reported by Kim et al. (2020). However, EDS mapping of the as-built SLM showed an inhomogeneous distribution of certain elements, such as Fe, in the melt pool (Fig. 3.4c). In contrast, the remelted SLM sample showed a homogeneous distribution of all the elements (Fig. 3.4d). Furthermore, the overall composition of the SLM samples was analyzed as a function of the melting sequence (Table 3.1). The amount of Mn decreases from 18.8 at% for the as-built SLM to 16 at% for the double melting, and the amount of Mn was found to be 12.2 at% for the triple melted SLM sample (Cr  $21.9 \pm 0.2$ , Fe  $20.5 \pm 0.3$ , Co  $22.5 \pm 0.7$ , Ni  $22.9 \pm 0.2$ ).

The reduction in the amount of Mn is probably because of the lower heat of vaporization (220 kJ/mol) and boiling point (2061 °C) compared to the other composing elements (Chen, 2020a).

Table 3.1 Composition (at%) of the CoCrFeMnNi HEA samples fabricated by SLM with remelting.

	Concentration of the elements (at%)				
	Cr	Mn	Fe	Co	Ni
As-built SLM	23.2 ± 0.2	18.8 ± 0.3	16.9 ± 0.4	21.1 ± 0.2	20.1 ± 0.4
Remelted SLM	21.6 ± 0.2	16.0 ± 0.1	18.9 ± 0.1	21.3 ± 0.1	22.2 ± 0.2

Hardness mapping is a tool to quantify heterogeneity of the parts and to understand the material behaviour. It was used to reveal the variation in hardness across the TCS and LCS of the fabricated SLM parts (Fig. 3.5), revealing that the CoCrFeMnNi HEA samples become more uniform and exhibit homogeneous hardness distribution of both TCS and LCS with the remelting scan strategy. Although the hardness of both SLM samples is higher than the traditional casting counterparts, the average microhardness in the TCS and LCS decreased from 269 ± 23 and 291 ± 12 HV for the as-SLM sample to 235 ± 22 and 240 ± 12 HV for the remelted SLM sample, respectively. Salishchev et al. (2014) studied the effect of Mn on the mechanical properties of CoCrFeNi HEA and reported an increase of ~21% in microhardness with the addition of Mn to the CoCrFeNi alloy. It is noteworthy that an anisotropy in the average microhardness of the parts can be observed owing to the directional heat distribution of the SLM process, where hardness ranges from ~200 to ~300 HV for TCS and ~250 to ~350 HV for LCS. Anisotropy in the RS may cause anisotropy in the mechanical properties and plastic deformation.

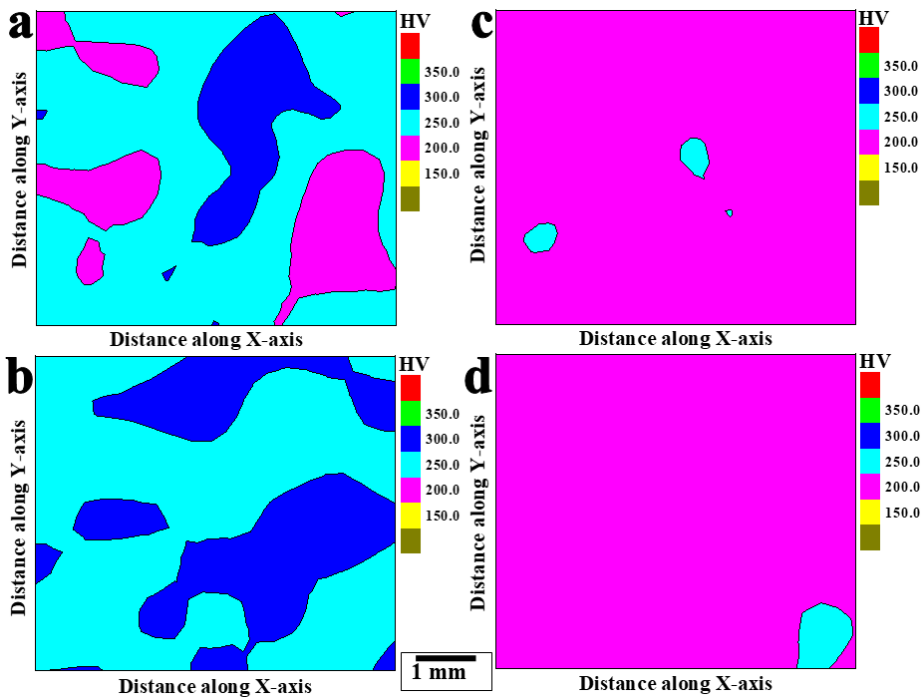


Figure 3.5 Hardness distribution maps for the CoCrFeMnNi HEA samples: **a** TCS and **b** LCS for as-SLM; **c** TCS and **d** LCS for remelted SLM.

The mechanical properties, including the ultimate compressive strength (UCS), yield compressive strength (YCS), and fracture strain (A) obtained from the room-temperature compression test of the samples, are presented in Table 3.2. The compressive tests of the as-built and remelted SLM samples were carried out up to ~50% compressive strain. Both the samples are flattened without complete fracture due to the excellent ductility of CoCrFeMnNi HEA fabricated using the SLM process. Several studies have investigated the compression strength of the CoCrFeMnNi HEA, and reported a ductile behaviour for this alloy. (Kim, 2020; Joo, 2017; Jeong, 2019; Wang, 2016). Qin et al. (2019a) investigated the compressive strength of CoCrFeMnNi and found no fracture up to ~50% compressive strain. In another work, Qin et al. (2019b) reported no fracture when the strain reaches 50%.

*Table 3.2 Compressive strength properties of the as-built and remelted SLM samples, obtained at room temperature. Note that no fracture was observed.*

		Samples	
		As-SLM	Remelted
Compression properties	UCS, MPa	1654 ± 37	1947 ± 130
	YCS, MPa	322 ± 1	505 ± 41
	A, (%)	> 50	> 50

### 3.2 SLM from GA HEA powder

The Morphology of the GA CoCrFeMnNi HEA powder, and its size distribution are shown in Figure 3.6 a–b. The majority of powders have a spherical shape, and satellite particles are also observed (Fig. 3.6a). From the frequency vs. particle diameter plot (Fig. 3.6b), it can be observed that the powder exhibits a narrow distribution with  $D_{10}$ ,  $D_{50}$ , and  $D_{90}$  values of 27, 39, and 57  $\mu\text{m}$ , respectively. Figure 3.6c and d show the XRD patterns of the HEA powder and as-built and remelted SLM samples, respectively, indicating the presence of a single FCC phase, which confirms the HEA structure. This is in agreement with the results reported by Li (R.) et al. (2018), who investigated the SLM of an equiatomic CoCrFeMnNi HEA and reported the presence of an FCC single phase. The crystallite size and lattice parameter were determined to be  $\sim 26 \pm 8$  nm and  $\sim 0.3595$  nm for the powder, respectively, and  $\sim 30 \pm 10$  nm and  $\sim 0.3593$  nm for the SLM samples, respectively.

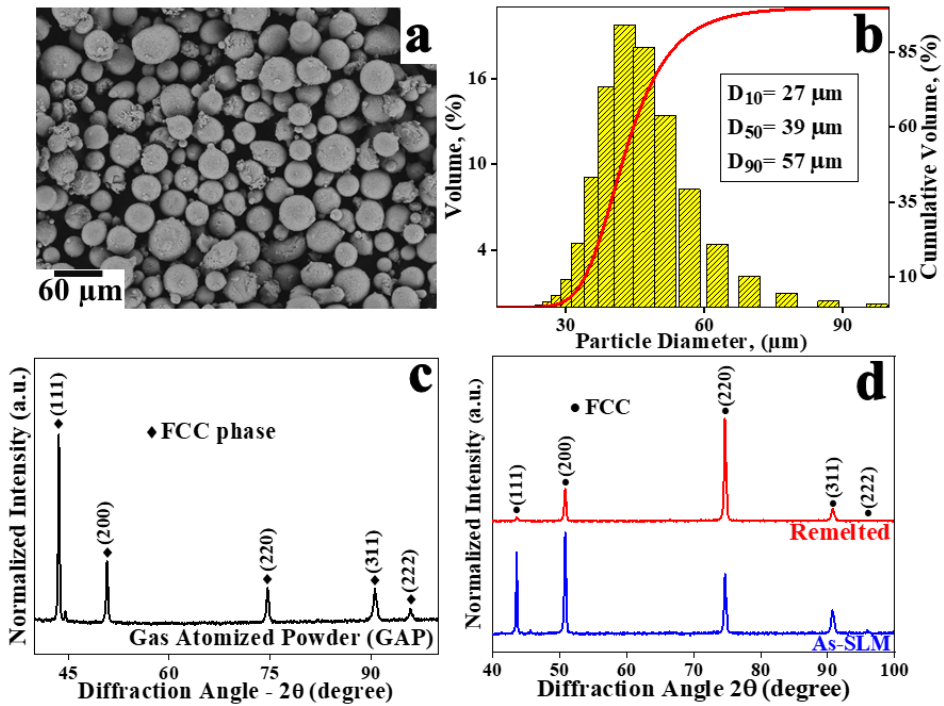


Figure 3.6 **a** SEM image of the GA CoCrFeMnNi powder, **b** Histogram of frequency vs. particle diameter of the HEA powder. XRD patterns of the HEA **c** GA powder and **d** SLM-processed samples ([PDF: 00-065-0528]).

Figure 3.7 a–b shows the TCS surfaces of the CoCrFeMnNi HEA fabricated via SLM from the GA powder. The laser tracks in the as-built SLM samples have an overlapped structure, similar to that observed in the HEA fabricated via SLM from mixed elemental powders (Fig. 3.3a). However, as shown in Figure 3.7 e–f, the laser tracks are less overlapped in the TCS of the remelted SLM sample (Fig. 3.7 e–f) compared to those observed for the as-SLM sample. The LCS of the as-built and remelted SLM samples are shown in Figure 3.7 c–d and g–h, respectively. It is noteworthy that the size and depth of the melts pool and the laser tracks did not show a significant difference between the parts fabricated from GA and mixed elemental powders.

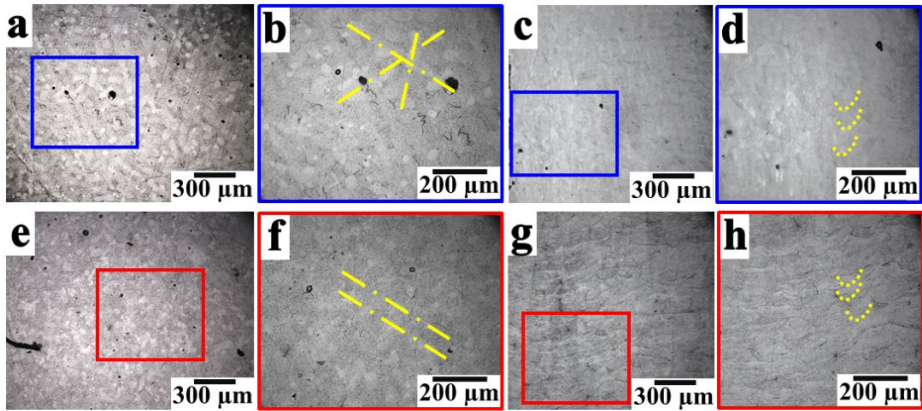


Figure 3.7 Optical micrographs of the samples from the GA CoCrFeMnNi powder showing the microstructure in: **a** TCS and its high magnification image in **b**, and **c** LCS and its high magnification image in **d** for the as-built SLM sample; **e** TCS and its high magnification image in **f**, and **g** LCS and its high magnification image in **h** for the remelted SLM sample.

Hardness mappings across the TCS surface of the as-built and remelted SLM samples from the GA CoCrFeMnNi HEA powder are shown in Figure 3.8, revealing that the as-built SLM CoCrFeMnNi HEA sample becomes more uniform and exhibits homogeneous hardness distribution in the TCS surface with the application of a remelting scan strategy. The average microhardness in the TCS decreased from  $229 \pm 17$  HV for the as-built sample to  $216 \pm 16$  HV for the remelted sample. The average Vickers hardness of the as-fabricated SLM samples in the TCS is similar to the value of 212 HV for SLM CoCrFeMnNi HEA reported by Piglione (2018). In addition, the theoretical density of the SLM samples from the GA powder was found to be  $\sim 94.0 \pm 0.2\%$ , which is close to that of the SLM parts from the mixed elemental powder.

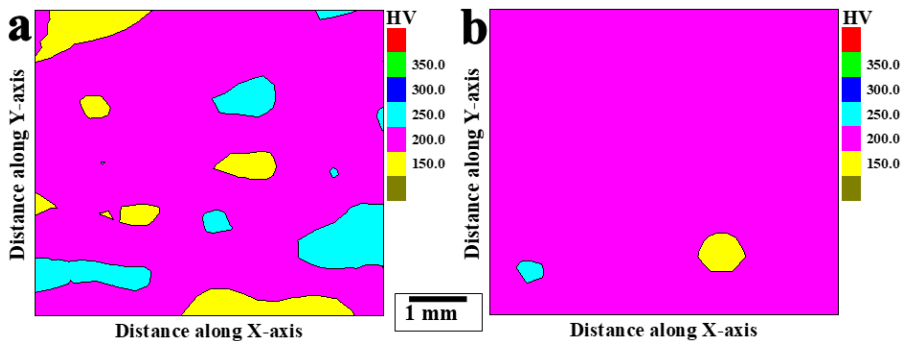


Figure 3.8 TCS hardness distribution maps for the SLM CoCrFeMnNi HEA samples from GA powder: **a** SM and **b** DM.

The mechanical properties, including the UCS, YCS, and A obtained from the room-temperature compression test of the SLM samples from the GA CoCrFeMnNi HEA powder, are shown in Table 3.3. The tests were performed up to a compressive strain of  $\sim 50\%$ . Both the samples flattened without complete fracture owing to their excellent ductility, in agreement with the results of Rogal et al. (2017), who reported high ductility for the parts produced using HIP. Therefore, the as-built and remelted SLM samples fabricated from GA and mixed elemental powders exhibit high ductility.

*Table 3.3 Compressive strength properties of the as-built and remelted SLM samples from the GA CoCrFeMnNi HEA powder, obtained at room temperature. Note that no fracture was observed.*

		Samples	
		As-SLM	Remelted
Compression properties	UCS, MPa	2422 ± 13	2722 ± 197
	YCS, MPa	452 ± 10	490 ± 41
	A <sub>c</sub> , (%)	> 50	> 50

The CoCrFeMnNi HEA parts were fabricated using SLM from two different powder feedstocks, namely, GA and mixed elemental powders. The microstructure, mechanical properties, chemical composition, and hardness of the fabricated parts were studied. Results suggested that a remelting scan strategy can be successfully applied to the in-situ fabrication of CoCrFeMnNi HEA using SLM from mixed elemental powder. With the application of laser remelting, the hardness distribution of the as-SLM samples from both GA and mixed elemental powders turned homogeneous. Although the remelted samples exhibited a slight decrease in hardness, and the amount of Mn in the fabricated parts from mixed elemental powders decreased, the remelting scan strategy eliminated the inhomogeneous distribution of the mixed elements. Overall, SLM (with the remelting scan strategy) of elemental powder can be an alternative approach to the SLM of pre-alloyed powder, significantly reducing the time and cost of production and increasing the versatility of the chemical composition of the powders.

## 4 Homogenisation of SLM Ti6Al4V alloys

### 4.1 In-situ Ti6Al4V alloying from elemental powders

Figure 4.1a shows the XRD patterns of the Ti6Al4V mixed elemental powder particles and elemental powders. The XRD analysis of the mixed elemental powders shows the diffraction peaks corresponding to Ti, Al, and V. Figure 4.1b shows the distribution of the mixed elemental powder particle sizes and the cumulative volume fraction. The powder particles show a narrow distribution with  $D_{10}$  and  $D_{90}$  values of  $\sim 31$  and  $\sim 63$   $\mu\text{m}$ , respectively, with the diameter of the most of powder particles is less than or equal to  $\sim 42$   $\mu\text{m}$  ( $D_{50}$ ). The SEM micrograph with EDS mapping of the powder mixture is shown in Figure 4.1c. The mixed elemental powder particles are irregular in shape and small in size and the EDS maps indicate the homogeneous distribution of Ti, Al, and V powder particles.

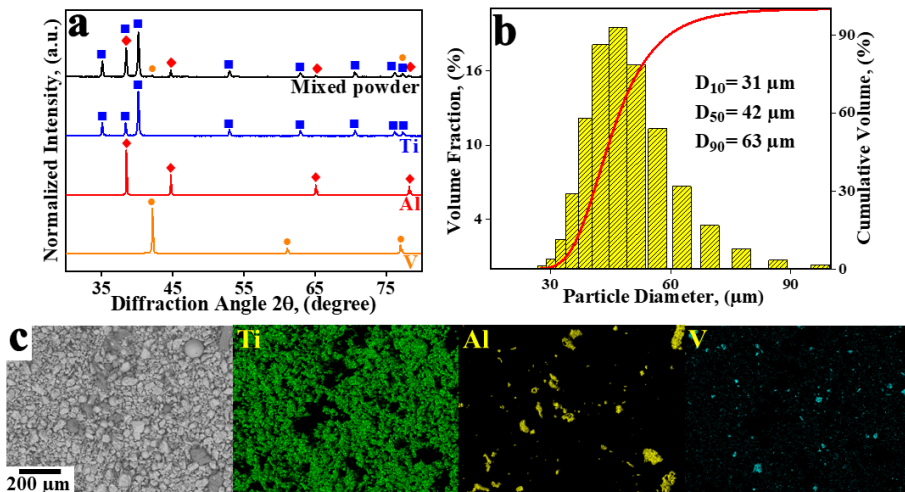


Figure 4.1 Mixed Ti6Al4V powder. **a** XRD analysis (using [PDF: 04-004-9158] for Ti, [PDF: 04-006-6522] for Al, and [PDF: 04-021-7462] for V). **b** Histogram showing the size distribution (volume fraction and cumulative volume fraction vs. powder particle diameter). **c** SEM micrograph of the powder mixture and the corresponding EDS maps.

During SLM fabrication, each powder layer is melted either one, two, or three times to investigate the influence of the remelting scan strategy (with the process parameters listed in Table 2.1). The XRD patterns of the SM, DM, and TM SLM samples from the elemental powder mixture in the TCS and LCS are shown in Figure 4.2, revealing the presence of the  $\alpha/\alpha'$  phase. Because both  $\alpha$  and  $\alpha'$  phases have the hexagonal close packed (HCP) structure with similar lattice parameters ( $a$  and  $c$  of  $\sim 0.295$  and  $\sim 0.461$  nm, respectively), they exhibit the same diffraction peaks and are not distinguishable in the XRD patterns, which was also noted by Cho et al. (2019). In this study, the lattice parameters,  $a$  and  $c$ , were determined to be  $\sim 0.2924$  and  $\sim 0.4767$  nm, respectively. Furthermore, the crystallite size was determined to be  $\sim 16 \pm 3$  nm.

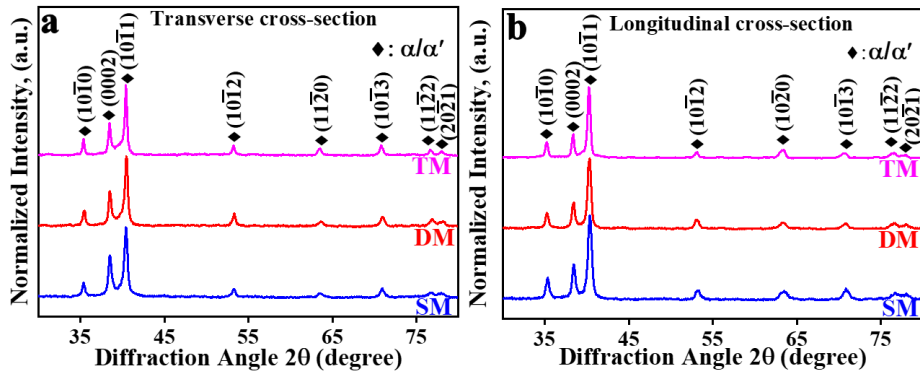


Figure 4.2 XRD diffractograms of the SLM Ti6Al4V samples as a function of melting sequence obtained from **a** TCS and **b** LCS ([PDF: 00-044-1294]).

Figure 4.3 shows the SEM images of Ti6Al4V specimens with an increasing number of melting steps. The microstructure of the SM, DM, and TM samples all comprise the  $\alpha/\alpha'$  phase, in agreement with XRD results. The presence of the  $\alpha/\alpha'$  phase can be attributed to the rapid solidification in the SLM process ( $\sim 10^5$  K/s), which could lead to a high hardness and tensile strength (Warren, 2018), low ductility (Liu, 2019), and poor fatigue behaviour (Edwards, 2014; Hrabe, 2019). The  $\alpha/\alpha'$  phase shows the plate morphology and the size of the lath changes with the number of melting steps.

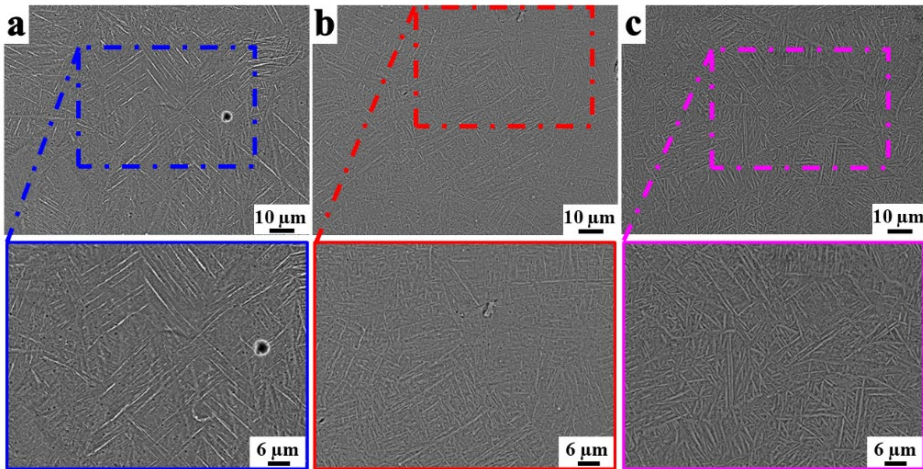


Figure 4.3 SEM images and their magnified views of the SLM Ti6Al4V samples produced from the elemental powder mixture with **a** one, **b** two, and **c** three melting steps.

Figure 4.4 shows the EDS maps of the SM, DM, and TM samples. The EDS maps of the SM sample exhibit an inhomogeneous distribution of the elements; such inhomogeneity in the microstructure could cause inhomogeneity in the mechanical properties and poor corrosion resistance. In contrast, the DM and TM samples show a homogeneous elemental distribution. Moreover, the chemical composition of the samples was measured using EDS point scans and is summarised in Table 4.1, revealing that the chemical composition of the fabricated SLM samples does not vary with increasing number of melting steps.



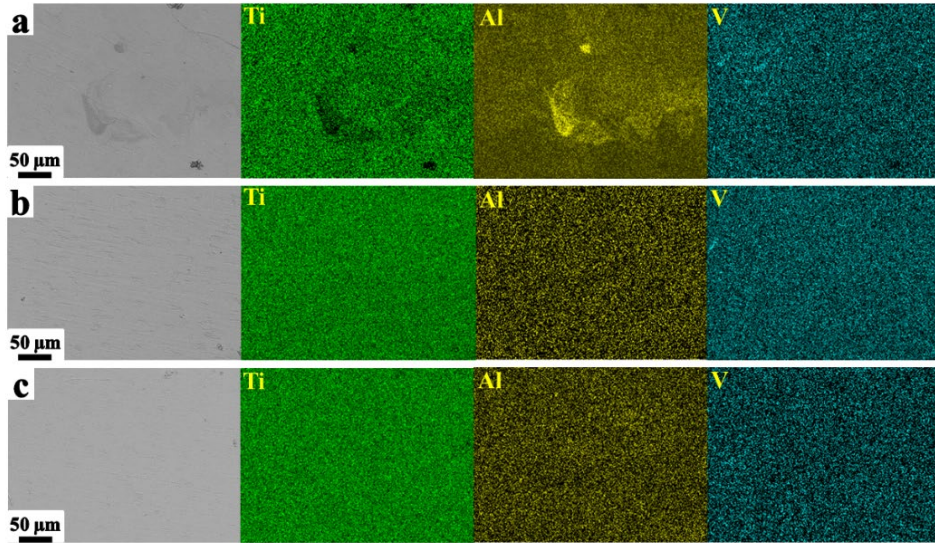


Figure 4.4 Backscatter SEM images showing the LCS and the corresponding EDS maps of the SLM samples as a function of melting steps: **a** SM, **b** DM, and **c** TM.

Table 4.1 Chemical composition of the SLM Ti6Al4V samples as a function of melting steps measured using EDS.

Sample	Concentration (wt%)			
	Al	V	Fe	Ti
SM	6.1	2.4	0.7	Balance
DM	5.1	2.4	0.1	Balance
TM	7.3	2.2	-	Balance

The hardness distribution maps of the SLM parts are shown in Figure 4.5 a–c. The as-SLM Ti6Al4V samples show an inhomogeneity in the hardness distribution, which ranges from 250–500 HV (Fig. 4.5a). However, the hardness distribution maps indicate more homogeneous hardness distribution following remelting. Nevertheless, the DM and TM samples show some degree of non-uniformity in the hardness distribution. The average microhardness increased from  $423 \pm 21$  HV for SM to  $431 \pm 14$  HV for DM and reached  $465 \pm 11$  HV for TM. Changing the number of melting steps effectively altered the microstructure of the SLM Ti6Al4V samples and affected the morphology of the  $\alpha/\alpha'$  lath dimensions, as shown in Figure 4.3, which, consequently, affected the mechanical properties, such as hardness and distribution. Moreover, using a laser remelting scan strategy can increase the density of twins, which can serve as a barrier to the progression of dislocations during plastic deformation, effectively strengthening a material according to the Hall–Petch relationship. Hence, it can result in an increase in hardness (Paper III).

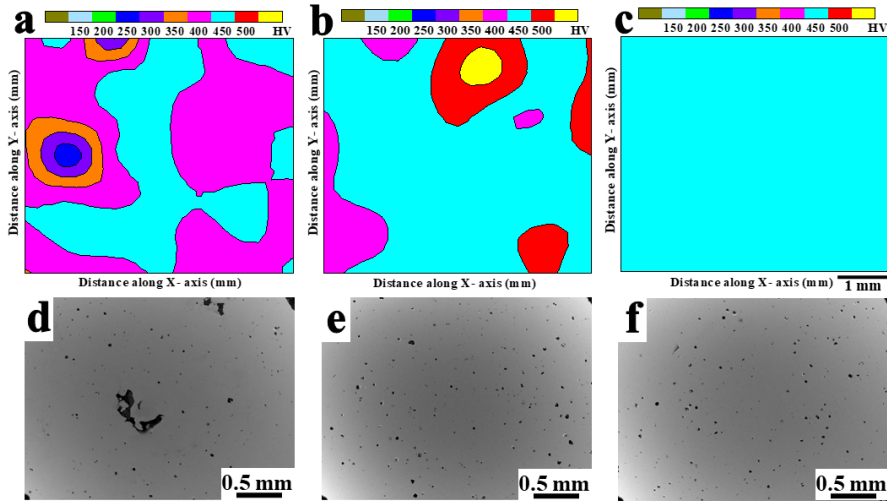


Figure 4.5 Hardness distribution maps and surface porosity of the SLM Ti6Al4V samples produced from a mixture of elemental powders: **a,d** SM; **b,e** DM; and **c,f** TM.

The morphology of the surface pores in specimens with remelting steps is shown in Figure 4.5 d–f. Upon increasing the number of melting steps from one to three, LOF pores, which typically have irregular shapes, could be eliminated. However, the MPs, which are spherical in shape and small in size, are still observed in the remelted samples. The theoretical densities of the SLM samples were found to be 97.3%, 98.2%, and 98.5% for the SM, DM, and TM samples, respectively.

The room-temperature compression tests of the SLM samples produced from mixed elemental powder were carried out and the mechanical properties, including the UCS and YCS, are summarised in Table 4.2. Increasing the number of melting steps slightly improves the UCS and YCS from SM to TM. It is noteworthy that the SLM samples exhibited higher UCS and YCS compared to those exhibited by their cast counterparts (Pederson, 2012).

Table 4.2 Compressive properties of the SLM samples from elemental powder mixture.

	Melting sequence			
	Single	Double	Triple	
Compression properties	UCS, MPa	1139 ± 52	1209 ± 63	1336 ± 100
	YCS, MPa	943 ± 69	1099 ± 45	1241 ± 36

## 4.2 SLM from GA Ti6Al4V powder

Figure 4.6a depicts the XRD pattern of the GA Ti6Al4V powder particles, revealing the presence of single-phase HCP  $\alpha$ -Ti. The inset shows the morphology of the powder particles that are spherical in shape with satellite particles attached to them. Figure 4.6b shows the distribution and cumulative volume fraction of the GA powder particle sizes. The powder comprises a narrow range of particle sizes ( $D_{10}$ ,  $D_{90}$ , and  $D_{50}$  of 31, 63, and 42  $\mu\text{m}$ , respectively). Figure 4.6c shows the XRD patterns of the SLM samples with different numbers of melting steps, indicating the presence of the  $\alpha/\alpha'$  phase, which is attributed to the rapid solidification of SLM. The lattice parameters,  $a$  and  $c$ , are 0.2923 and 0.4683 nm, respectively, with an average crystallite size of  $\sim 15 \pm 0.5$  nm.

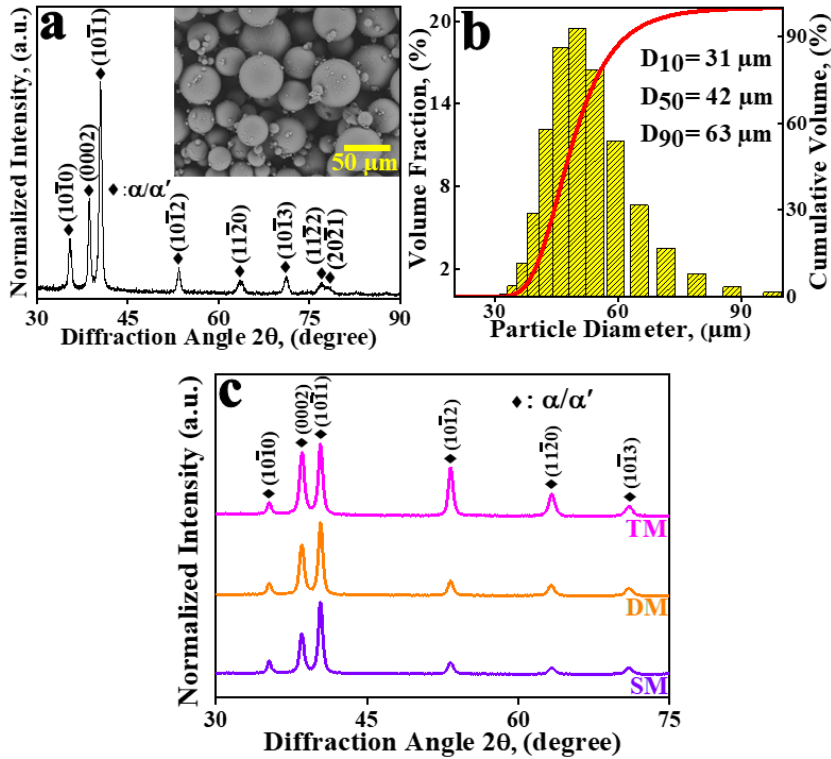


Figure 4.6 **a** XRD pattern of the GA Ti6Al4V powder. The inset shows the SEM profile of the GA powder. **b** Histogram showing the size distribution (volume fraction and cumulative volume fraction vs. powder particle diameter). **c** XRD patterns for the SLM-processed Ti6Al4V samples as a function of the number of melting steps ([PDF: 00-044-1294]).

Figure 4.7 shows the SEM and TEM images of the samples with a different number of melting steps. The microstructure of SM, DM, and TM all comprise the acicular  $\alpha/\alpha'$  phase (Fig. 4.7a, d, and g), in agreement with the XRD results. However, the size of the acicular  $\alpha/\alpha'$  phase changes with remelting, with the width ( $0.40 \pm 0.05$ ,  $0.65 \pm 0.05$ , and  $1.31 \pm 0.12 \mu\text{m}$  for SM, DM, and TM, respectively) increasing and the length ( $12 \pm 6$ ,  $10 \pm 4$ , and  $8 \pm 4 \mu\text{m}$  for SM, DM, and TM, respectively) decreasing as the number of remelting steps increases. In addition, a large proportion of the acicular  $\alpha/\alpha'$  phase is twinned in the SM sample, which can be attributed to the non-uniform heat distribution in the powder bed and the high internal strain, shown in the magnified view inserted in Figure 4.7a. The chemical composition of the SLM samples measured using the EDS point scans is given in Table 4.3, indicating that the chemical composition of the samples does not vary with an increase in the number of melting steps.

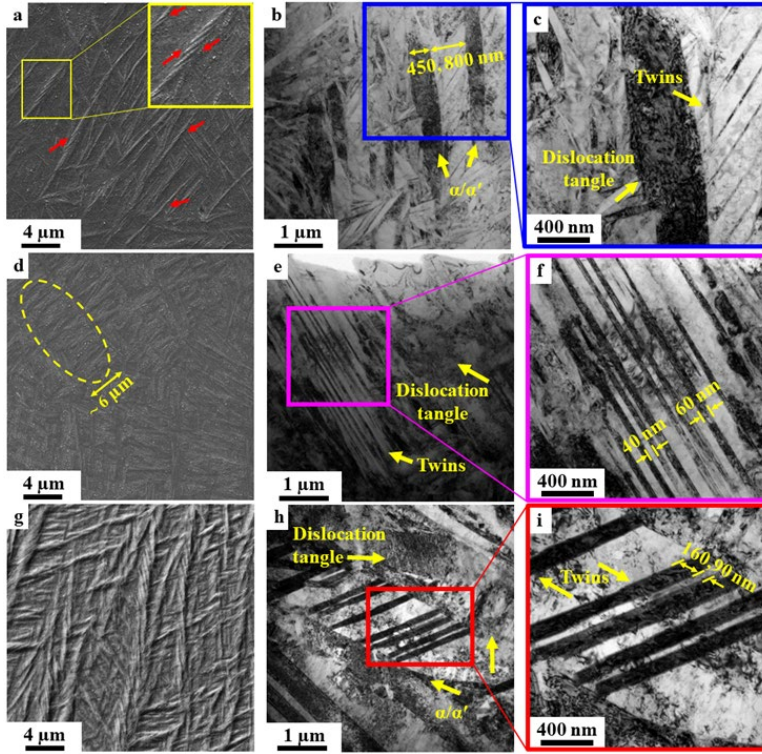


Figure 4.7 Microstructure and substructure of SLM samples. **a** SEM image (the red arrows indicate twined acicular  $\alpha'$  martensite) and **b** TEM image (showing acicular  $\alpha'$  martensite and twins) and its high magnification image in **c** of SM. **d** SEM and **e** TEM image (showing uniformly distributed twins) and its high magnification image in **f** of DM. **g** SEM image and **h** TEM image (showing uniformly distributed twins) and its high magnification image in **i** of TM. (modified from (Paper III)).

Table 4.3 Chemical composition of the SLM Ti6Al4V samples produced from GA powder measured using the EDS in TEM.

	Sample		
	SM	DM	TM
Al	6.9 ± 0.1	5.9 ± 0.3	6.6 ± 0.1
V	3.2 ± 0.7	3.5 ± 0.8	3.5 ± 0.7
Fe	0.2 ± 0.3	0.2 ± 0.1	0.2 ± 0.3
Ti	Balance	Balance	Balance

The TEM images of the samples indicate the presence of uniformly distributed twins between the acicular  $\alpha/\alpha'$  phases (Fig. 4.7 b–c, e–f, and h–i for SM, DM, and TM, respectively). In addition, high-density dislocations arraying in tangles are evident inside the matrix and the acicular  $\alpha/\alpha'$  phase.

Hardness distribution maps of SLM parts are shown in Figure 4.8 a–c, revealing homogeneous distribution of hardness for the TM sample. However, in the SM and DM samples, some degree of non-uniformity is observed in the hardness distribution. In addition, the average Vickers hardness values increased from  $334 \pm 10$  HV for SM to  $347 \pm 7$  HV for DM, reaching  $368 \pm 12$  HV for TM. Changing the number of melting steps

effectively altered the microstructure of the SLM Ti6Al4V samples produced from GA powder in terms of the dimensions of acicular  $\alpha/\alpha'$  phase, which affected the hardness and its distribution. Furthermore, the Vickers hardness of the LCS surfaces of the SLM samples ( $\sim 410$  HV for SM and DM and  $\sim 440$  HV for TM) are higher than that of the TCS surfaces.

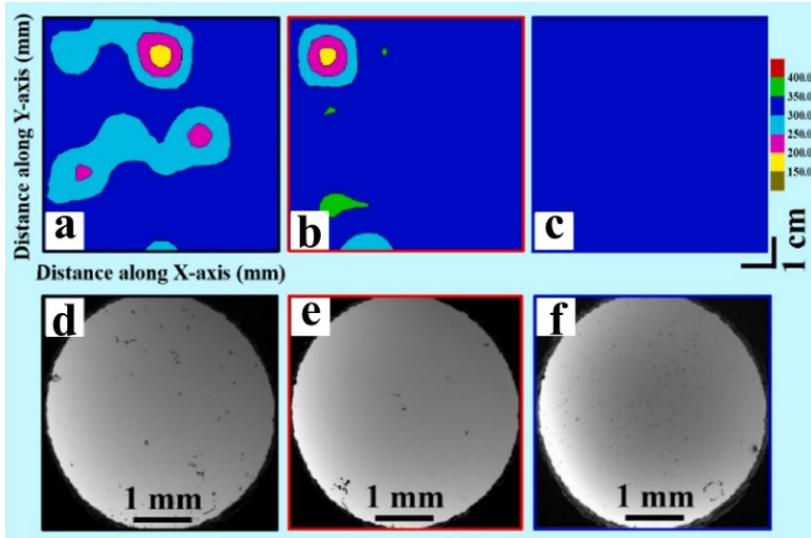


Figure 4.8 Hardness distribution maps and surface porosities of the SLM Ti6Al4V samples from GA powder: **a,e** SM; **b,f** DM; and **c,g** TM (modified from (Paper II)).

The morphology of surface pores in the specimens with remelting steps is shown in Figure 4.8 d–f. The LOF pores could be eliminated by applying a remelting scan strategy, while the MPs are retained. However, the size of these pores is significantly reduced upon increasing the number of melting steps from one to three. The theoretical densities of the SLM samples were found to be  $98.0 \pm 0.5\%$ ,  $98.8 \pm 0.3\%$ , and  $99.5 \pm 0.2\%$  for the SM, DM, and TM samples, respectively.

Figure 4.9a shows the tensile stress-strain curves for the SLM Ti6Al4V samples, and the corresponding mechanical properties are listed in Table 4.4. The ultimate tensile strength (UTS) and yield strength (YS) values obtained from the room-temperature tensile test, increased upon increasing the number of melting steps and are higher than the wrought counterpart (Gil, 2001; Salishchev, 2014). However, the ductility of the TM sample is inferior compared to that of the SM and DM samples. The fracture surfaces of the tensile samples are shown in Figure 4.9 b–g. The fracture surface of the SM sample (Fig. 4.9 b–c) showed the presence of deep dimples, indicating appreciable ductility. In contrast, the DM and TM samples (Fig. 4.9 d–g) showed shallow and small sized dimples, suggesting that the samples are more brittle.

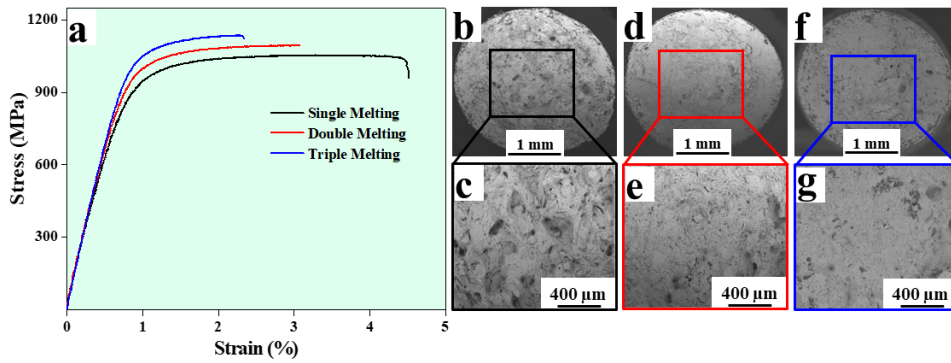


Figure 4.9 **a** Tensile stress-strain curves for the SLM Ti6Al4V samples. SEM images of the fracture surface for the SLM samples: **b** SM and its high magnification image in **c**; **d** DM and its high magnification image in **e**; and **f** TM and its high magnification image in **g** (adopted from Paper II).

Table 4.4 Room-temperature tensile/compressive properties of the SLM Ti6Al4V samples (tensile properties adopted from (Paper II)). *E* indicates the elastic modulus.

		Melting sequence		
		Single	Double	Triple
Tension	UTS, (MPa)	1055 ± 3	1104 ± 12	1135 ± 3
	YS, (MPa)	930 ± 0.2	985 ± 8	1027 ± 5
	Elongation, (%)	4.3 ± 0.5	3 ± 0.1	2 ± 0.1
	<i>E</i> (GPa)	120 ± 1	128 ± 0.9	134 ± 5
Compression	UCS, MPa	1423 ± 159	1544 ± 23	1613 ± 62
	YCS, MPa	1109 ± 96	1149 ± 86	1162 ± 92
	<i>A<sub>c</sub></i> , (%)	23 ± 3	21 ± 3	15 ± 6

Compressive tests were carried out to evaluate the effect of intrinsic defects (such as porosity) on the mechanical properties. The mechanical properties obtained from the room-temperature compression test of the samples, are presented in Table 4.4. It can be seen that the melting sequence improved the average values of UCS and YCS from SM to TM, but it causes a significant decrease in ductility. An asymmetry is observed in the strength behaviour under tensile and compressive stress (strength differential effect). In addition, the Charpy impact test was carried out to determine the influence of laser remelting, microstructure, and defects (porosity) on the capacity of SLM-fabricated parts to absorb energy before failure (Fig. 4.10a). The Charpy absorbed impact energy increases upon increasing the number of melting steps. However, the impact energy value of the SLM samples from GA powder is lower than their cast counterparts (Takao, 1992). Furthermore, Figure 4.10b shows that the RS increases as the number of melting steps increases at both the TCS and LCS surfaces. Due to the directional heat distribution of the SLM process, anisotropy in the RS distribution of the parts can be created, where the RS value in the TCS is lower than that in the LCS (Fig. 4.10b). Anisotropy in the RS may cause anisotropy in the mechanical properties and plastic deformation (Vrancken, 2014).

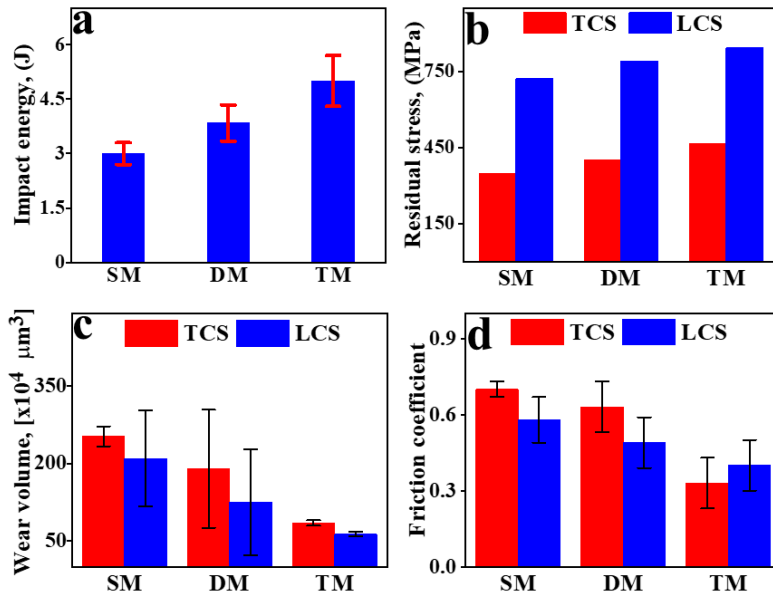


Figure 4.10 **a** Absorbed energy obtained from the Charpy V-notch test. **b** RS values of the SLM samples for both TCS and LCS surfaces. **c** CoF values for TCS and LCS surfaces of SLM samples. **d** Average wear volumes of SLM samples (modified from (Paper IV)).

Tribological sliding wear tests with ball-on plate configurations were conducted to evaluate the wear resistance and coefficient of friction (CoF) values of the SLM samples as. As shown in Figure 4.10d, the CoF values of both the TCS and LCS surfaces decrease with an increase in the number of melting steps. In addition, the average wear volumes of the SLM parts (Fig. 4.10c) decrease with an increase in the number of melting steps for both the TCS and LCS surfaces. It can be seen that the as-built and remelted SLM samples exhibit anisotropy in the average wear volume and CoF.

The room-temperature HCF testing results of the SLM samples are shown in Figure 4.11. Runout, i.e., the HCF test samples that survive under the stress amplitude of 100 MPa for up to  $10^6$  cycles, is marked with an arrow. The HCF strength of the fabricated specimens improved with increasing the number of melting steps. It has been reported that the HCF endurance limit of parts fabricated by the SLM process is considerably lower than the wrought counterparts (Fotovvati, 2019), which can be due to the defects and/or RSs associated with the SLM process.

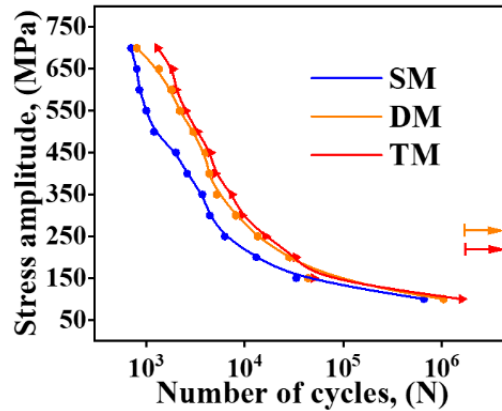


Figure 4.11 S-N curves of SLM samples. Arrows indicate runout (modified from (Paper IV)).

Ti6Al4V parts were fabricated using the SLM process with different melting sequences from two different powder feedstock, viz. mixed elemental and GA powders. The microstructure, substructure (twining and dislocation propagation), and mechanical properties, including hardness, strength, impact, and fatigue, were studied. Inhomogeneities in chemical composition and hardness were discussed. Tribological properties, obtained from sliding wear tests, were studied. In addition, the effect of remelting scan strategy on the mechanical and tribological properties, porosity, and microstructure and substructure were investigated. The present results indicate that a remelting scan strategy can be successfully applied to the in-situ fabrication of Ti6Al4V alloys using SLM from mixed elemental powder. Upon the application of laser remelting, the hardness distribution of the as-SLM samples from both GA and mixed elemental powders became homogenised. In summary, the present results suggested that the remelting scan strategy refines the microstructure and improves the mechanical properties of SLM Ti6Al4V samples; however, it increases the production time and cost.



## 5 Discussion

### 5.1 In-situ alloyed materials

The SLM process can produce the most complex objects from pre-alloyed powders with minimal wastage and no need for special tooling. A large portion of such powders is produced by atomisation processes, particularly the GA process. However, these pre-alloyed atomised powders have a narrow composition range, time-consuming and resource-intensive production process, and limited availability. In-situ alloying is an affordable strategy to fabricate SLM parts from elemental powder mixtures. In-situ alloying via SLM can be applied to overcome the shortcomings of this process in the manufacturing of parts from GA powders. This effective strategy offers several advantages, i.e., producing parts from elemental powder mixtures with a lower cost, compositional flexibility and improved availability. However, inhomogeneity of in-situ alloying with a large fraction of elements could result in inhomogeneous distributions or unalloyed elements and laser remelting reduced the inhomogeneity, where it could span the TRL of materials. In addition, the procedure can be applied to explore the printability as well as the microstructure of the desired composition, because the microstructural and mechanical properties of SLM-fabricated parts may differ from those of their traditional counterparts (such as casting) owing to rapid solidification and layered-wise production. Furthermore, in-situ alloying by the SLM process is attracting increasing attention from researchers and engineers. As discussed in section 1.4, the cost of the mixed elemental powder particles is almost an order of magnitude lower than that of commercial atomised powders, suggesting a significant improvement in the affordability.

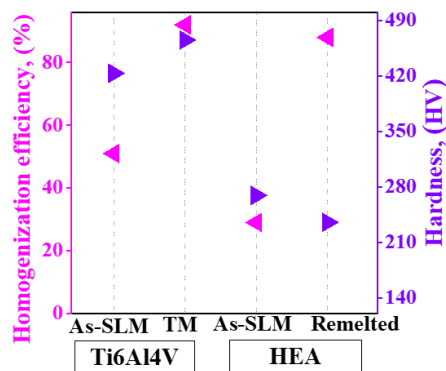


Figure 5.1 Homogenisation efficiency and hardness values of the as-built and remelted SLM samples from elemental powder mixture. (Details related to the homogenisation efficiency were discussed in Section 2.5.1).

As discussed in Sections 3.1 and 4.1, the SLM-fabricated parts from mixed elemental powder exhibited comparable mechanical properties to those produced from pre-alloyed powders (Sections 3.2 and 4.2). However, the SLM parts fabricated from elemental powder mixtures exhibited inhomogeneity in elemental distribution and, consequently, in their microstructure, which may lead to local variability in mechanical and tribological properties. Nevertheless, previous investigations of the inhomogeneity of SLM parts have been largely constrained to a qualitative level. Here, homogenisation efficiency was applied to quantitatively compare the inhomogeneity of the SLM samples. Figure 5.1

shows a comparison of the homogenisation efficiency and hardness of in-situ alloyed Ti6Al4V and CoCrFeMnNi HEA via the SLM process. The hardness range for the Ti6Al4V and CoCrFeMnNi HEAs were 450–500 and 200–250 HV, respectively, and the values in these ranges are shown. The homogenisation efficiency in both alloys classes increased by increasing the number of melting steps. The microstructures of the Ti6Al4V and CoCrFeMnNi HEAs are consistent with those that are typically observed for their alloy classes, namely acicular  $\alpha/\alpha'$  and fine grains, respectively. The morphology of the microstructure changes with the number of melting steps and, consequently, affects the mechanical properties. In addition, the homogeneous hardness distribution maps (hardness uniformity all over the samples) also indirectly confirm that the samples were homogenised with an increasing number of melting steps. Furthermore, the density of parts fabricated from the mixed elemental powders was comparable to those obtained from the GA powders.

The as-built SLM samples produced from elemental powder mixtures showed an inhomogeneous distribution of the elements, which can affect the mechanical properties and corrosion and wear resistance. Inhomogeneity of in-situ alloying with a large fraction of elements (over 5 at% (Chen, 2020a)) can result in inhomogeneous distributions or unalloyed elements. As discussed in Section 3.1, the in-situ alloying of equiatomic (i.e., 20 at% for each element) HEA via SLM exhibited inhomogeneity in the elemental distribution application of a remelting scan strategy led to successive melting and solidification events at different rates, resulting in the homogenisation of the microstructure and an uniform distribution of the elements.

In the rapid solidification powder bed fusion processes, such as SLM, due to the extremely short duration of laser-material interaction and accompanying highly localised heat input, the melt pool is rapidly quenched by the previously solidified layers (Yasa, 2010). As a result, the microstructural and mechanical properties of the SLM-fabricated parts can differ from those of their traditional cast or wrought counterparts. In addition, there is a large number of SLM process parameters that affect the fabrication process and the mechanical and microstructural properties of the fabricated parts. Yadroitsev (2009) reported that there are more than 130 process parameters that could influence the quality and mechanical properties of the fabricated parts using SLM. Among these process parameters, the melt pool geometry plays a vital role in the properties of the fabricated parts, because, e.g., a small SLM part consists of  $\sim 10^5$  melt pools or hatches (for a cuboid with the dimensions of  $10 \times 10 \times 15$  mm with a hatch distance and layer thickness of 60 and 25  $\mu\text{m}$ , respectively). Numerous studies have investigated the effect of the melt pool depth on the mechanical and microstructural properties and defect formation, such as LOF pores and improper bonding in the SLM parts (Ali, 2018; Li, Liu, 2017; Liu, 2019). The SLM HEA parts were chosen to study the melt pool size because the laser tracks and melt pools were observable in both the TCS and LCS. In order to melt the powder or bulk and form a melt pool with a temperature higher than the melting point, the required energy ( $E_{\text{required}}$ ) can be calculated as follows (Tan, 2018; Coelho, 2018):

$$E_{\text{required}} = C_p m (T_m - T_0) + mL_f, \quad 5.1$$

where  $C_p$  is the heat capacity (J/kg·K),  $L_f$  is the latent heat of fusion (J/kg),  $T_m$  and  $T_0$  are the melting and substrate temperatures (K), respectively, and  $m$  is the mass of the spherical sector of the melt pool (kg). The  $C_p$  and  $L_f$  of equiatomic CoCrFeMnNi HEA was reported to be 494 J/kg·K and  $2.8 \times 10^5$  J/kg. The  $m$  value can be measured as follows:

$$m = \rho \frac{2}{3} \pi r^2 h, \quad 5.2$$

where  $\rho$  is the density of the material ( $\text{kg/m}^3$ ), and  $h$  is the depth of melt pool (m). The laser (pulse) energy input can be determined from the following expression (Abioye, 2019):

$$E_{in} = \eta Pt, \quad 5.3$$

where  $P$  is the laser power (W),  $t$  is the laser exposure time (s), and  $\eta$  is the absorptivity of the laser. Accordingly, the depths of the melt pool ( $h$ ) of the as-built and remelted SLM HEA samples were determined to be  $\sim 39$  and  $\sim 23$   $\mu\text{m}$ , respectively. However, there is a minor discrepancy between the calculated  $h$  values and those obtained from optical observation ( $\sim 34 \pm 5$  and  $\sim 24 \pm 3$   $\mu\text{m}$  for as-built and remelted SLM, respectively) and the average error of the estimated  $h$  values was  $\sim 10\%$ . Nevertheless, some simplifying assumptions were used in the calculation. It was assumed that the laser beam melts only powder particles and partial remelting of previously solidified layers or adjacent laser tracks was eliminated. The difference in physical properties of the bulk and powder bed was ignored. The melt pool shapes were considered to be spherical sectors, while the observations indicated that they were irregular in shape (Fig. 3.3b and 3.7c).

In the SLM process, the molten pool dynamics involve multiple physical phenomena (Zhao, 2020), and the Marangoni effect and vapour recoil pressure have a vital impact on the compositional uniformity in the melting stage of the powder mixture (Mosallanejad, 2021). Figure 5.2 illustrates the Marangoni effect and the vapour recoil pressure in the SLM process. The Marangoni effect plays a dominant role in the mass transfer phenomenon in the melt pool, which constitutes the majority of the fluid flow in the melt pool during the SLM process due to a gradient of surface tension (He, 2020). During the interaction of the high-energy laser (with a spot size of  $\sim 39$   $\mu\text{m}$ ) and the powder, a small melt pool ( $\sim 100$   $\mu\text{m}$ ) is formed. A temperature gradient inside the pool results in a gradient of surface tension on the top surface, promoting local melt flow. As can be seen from Figure 5.2, the bottom part of the melt will be lifted upward with the surface material transferring downward, where the Marangoni force contributes to the complete melting of the particles by dragging them into the melt pool (Tan, 2021). This can accelerate the movement of the unmelted or partially melted powder particles to the bottom of the melt pool. However, an elemental powder mixture, particularly in the HEAs with high atomic fractions, may exhibit different solidification behaviour. As discussed in Section 3.1, inhomogeneity was observed in the elemental distribution (Fig. 3.4c). Application of a remelting scan strategy improved the chemical homogeneity of in-situ alloyed HEA. The Marangoni effect, which causes fluid flow in the melt pool, provides the opportunity for homogenising elemental distribution of in-situ alloying using the SLM process with remelting. In SLM, the melt expulsion by the recoil pressure is caused by spatial variation of the normal stress exerted by vapour pressure. The gradient of vapour pressure causes melt flow from the high-pressure zone toward the low-pressure zone (Volkov, 2017).

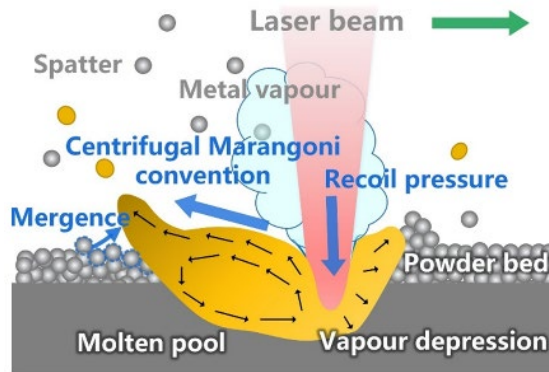


Figure 5.2 Schematic illustration of the mechanisms of the protrusion at the rear of the molten pool because of the vapour recoil pressure and Marangoni convection (adopted from (Yin, 2020)). Note that droplet spatter can from due to the vapour recoil pressure.

In-situ alloying of two classes of alloys, viz. Ti6Al4V and equiatomic CoCrFeMnNi HEAs, via the SLM process was investigated. The as-built SLM samples showed a degree of inhomogeneity in elemental and hardness distributions. The results indicated that a remelting scan strategy could successfully decrease inhomogeneity of the in-situ fabricated Ti6Al4V and CoCrFeMnNi HEAs. Although a remelting sequence will increase production cost and time, the present results clearly indicate that it reduce inhomogeneities in microstructural and mechanical properties. However, the remelted HEA samples showed a slight decrease in the hardness value because of a reduction in the amount of Mn. Furthermore, a remelting scan strategy can eliminate the inhomogeneous distribution of the mixed elements and reduce porosities. Overall, SLM with a remelting scan strategy using elemental powder can be an alternative approach to the SLM of pre-alloyed powder, which will significantly reduce production time and cost and increase the flexibility of the chemical composition of the powders.

## 5.2 SLM from GA powder: Effect of laser remelting

Ti6Al4V and equiatomic CoCrFeMnNi HEA parts were manufactured using the SLM process, and the occurrence of LOF pores and MPs were investigated in the fabricated parts. Reducing porosity in SLM parts is a major challenge. Porosity affects the tribological and mechanical properties, including fatigue and tensile strength. Koutiri et al. (2018) have reported that porosity (particularly LOF pores) is the reason for crack formation in SLM parts under cyclic loading. In the rapid solidification of the SLM process, there is not sufficient time available for conductive homogenisation of the input energy and heat distribution in the powder bed. Therefore, pore formation occurs in the SLM samples. LOF pores and MPs can form because of the improper selection of SLM process parameters and gas entrapment, respectively (Cao, 2017; Günther, 2017; Masuo, 2018). As discussed in Chapters 3 and 4, the morphology of surface pores in the SLM samples changes when a remelting scan strategy is used. Increasing the number of melting steps can eliminate LOF pores, but MPs are retained. However, the size of these pores is significantly reduced with an increasing number of melting steps, as shown in Figure 5.3a and b for the Ti6Al4V and CoCrFeMnNi HEAs, respectively. A reduction in the LOF pores can lead to improvement of fatigue and impact behaviour, as well as tensile and compression strength.

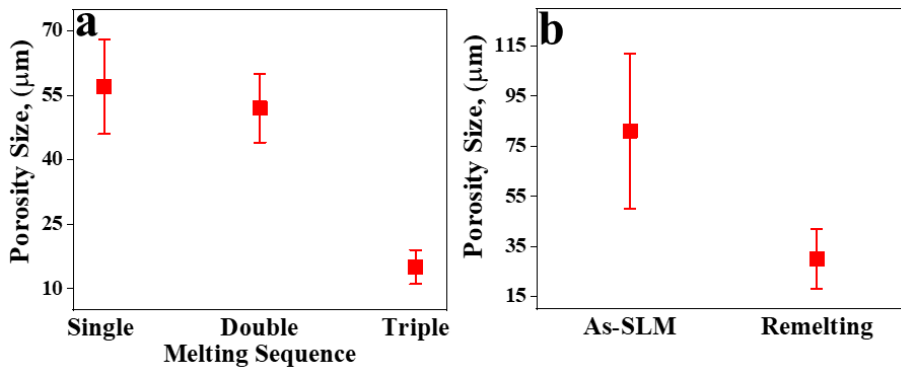


Figure 5.3 Surface porosity of SLM samples as a function of melting sequence from GA powder: **a** Ti6Al4V and **b** high-entropy alloys.

Using a remelting scan strategy improved the mechanical properties, such as hardness and strength, of the SLM parts. Increasing the number of melting steps improved their tension and compression strengths of the SLM Ti6Al4V samples produced from GA powder, and increased the average Vickers hardness values of the LCS and TCS surfaces. However, ductility decreased with an increasing number of melting steps. Moreover, the results obtained from Charpy tests of Ti6Al4V produced from GA powder indicated that the laser remelting strategy improved the impact energy, which is ascribed to the reduction in LOF. Hrabe et al. (2019) studied the effect of porosity on Charpy absorbed energy of Ti6Al4V parts fabricated by EBM and reported that porosity has a detrimental influence on the impact energy.

The remelting scan strategy improved the fatigue behaviour of the SLM parts, which is drawback of AM parts. Increasing the number of melting steps from single melting to triple melting resulted in an improvement of the HCF strength of the SLM Ti6Al4V samples produced from GA powder. SLM parts usually exhibit much lower (over 75% (Fotovvati, 2019)) HCF life compared to their wrought counterparts, mainly due to the presence of discontinuities such as pores (LOF and MP), which may act as nuclei for crack formation. LOF pores, which refer to the zones of non-processed powder particles, are irregular in shape and large in size. LOF pores are the main factor for defects that can initiate cracks because of induced stress and accumulated plastic strain (Li, 2009), which may deteriorate the HCF behaviour. A large number of studies have clearly demonstrated that the number of LOF pores is decreased with the application of laser remelting, and, consequently, results in higher density (Demir, 2017; Paper II; Liu, 2019; Pei, 2020). As mentioned in Section 3.2, the remelted samples (in particular TM) showed an improvement in the HCF life due to a significant reduction in the number of LOF pores. It should be noted that the location of discontinuities (LOF and MP) plays a major role in the fatigue behaviour of AM Ti6Al4V (Günther, 2017).

RS plays an essential role in the performance and mechanical and tribological properties of SLM parts (Gu, 2012; Liu, 2019; Yasa, 2010). In a rapid solidification process such as SLM, the materials are subjected to a large thermal gradient, which can reach  $\sim 10^7$  K/m (Vrancken, 2014)). This can be attributed to the short duration of the laser-material interaction and highly localised heat input ( $< 2600$  °C (Liu, 2019)). In addition, the thermal conductivity of the loose powder bed is much lower compared to that of the bulk material, where it is around two orders of magnitude lower than in the bulk. The large thermal gradient, low thermal conductivity, and rapid heating by laser irradiation

can result in RSs. In the SLM process, a bending moment is generated when the first layer is scanned, which, in a layered-wise production, becomes more complex (Boruah, 2018). In the SLM process, the top layer expands and the previous layers limit this expansion, and a large thermal gradient can exacerbate this process. Hence, a compressive stress can be formed in the top layer of the SLM sample. During solidification, the upper layers shrink, and the compressive stresses change to tensile stresses because their thermal contraction is limited. Moreover, these stresses can rise above the yield stress of the material. In a layer by layer fabrication, each layer will produce stresses, forming a complicated superposition of stresses and strains (Yadroitsev, 2015). Hence, the additively manufactured materials may show plastic deformations whenever the stress rise above the yield stress. It is also noteworthy that the cooling rate is higher in the remelted samples than that of the as-SLM samples, which can influence the microstructural and mechanical properties. As observed, tensile/compressive stresses were higher in the remelted specimens than those of the as-SLM samples. Shiomi et al. (2004) studied the influence of remelting scan strategy on RS and found that the measured RS in remelted samples was higher than that of the as-SLM samples.

The substructure of the AM Ti6Al4V samples via the SLM process with remelting scan strategy was studied, because the substructure also influences the mechanical properties. In the SLM Ti6Al4V, a high density of dislocations, stacking faults, and twins was observed (Fig. 4.7) (Cao, 2020). Twinning and plastic deformation can be formed in Ti alloys and are considered to be competitive mechanisms. Twinning can appear in a few microseconds, while slip bands can be formed in several milliseconds. Twins can form because of the limitations of slip systems. Moreover, high shear stress may lead to the formation of the twins and twins can be formed with a lower amount of stress than that required for slip formation. As discussed, compressive and tensile stresses can remain in the SLM samples that can result in plastic deformation, which can relieve the stress when it is above yield stress. A large number of studies have reported twinning as a strain-accommodation and stress-relief mechanism (Luo, 2012; Morawiec, 2009). Both compressive and tensile twinning types can accommodate strain in a material. Moreover, increasing the number of remelting steps increases the cooling rate, which can enhance the probability of twinning because of the changes in the critical resolved shear stresses for twinning that favour twinning formation (Azarniya, 2019; Cao, 2018; Poorhaydari, 2006). As described in Section 4.2, the substructure of SLM Ti6Al4V alloys changed upon increasing the number of remelting steps, resulting in an increased amount of twinning. This is probably because of the higher amount of RS and higher cooling rate in the remelted samples. According to the Hall–Petch relationship, the formed twins can act as a barrier to the propagation of dislocation during plastic deformation, similar to conventional grain boundaries, and may effectively strengthen the material.

Dislocations can appear in the material during the SLM process because of plastic deformation and rapid solidification (Gorsse, 2017). As discussed, this phenomenon can accommodate the internal stresses of AM materials. The substructure of the SLM Ti6Al4V samples exhibited a high density of tangled dislocations within the acicular phase (Fig. 4.7), making it challenging to quantify the density of dislocations. Figure 5.4 shows that the density of dislocations increased upon increasing the number of melting sequences from one to three. Furthermore, it was observed that from the TEM images that the density of dislocation increased with remelting. Nevertheless, the XRD results indicated information from considerably larger volumes of the materials compared to the TEM measurements.

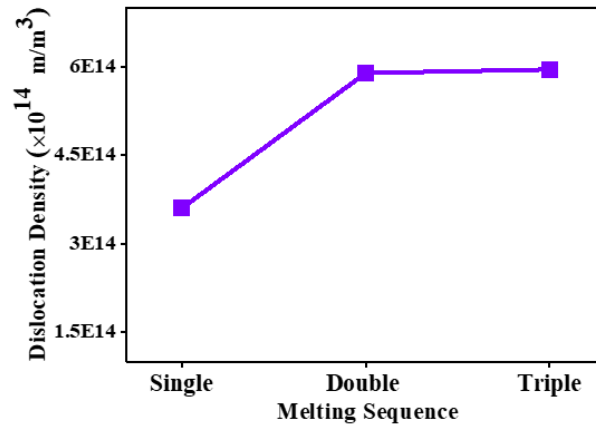


Figure 5.4 The dislocation density of SLM Ti6Al4V samples obtained from XRD data.

The SLM parts were fabricated from commercial GA Ti6Al4V and CoCrFeMnNi HEA powders, and the microstructure, substructure, mechanical and tribological properties, RS, and surface quality of these parts were investigated. It was observed that a remelting scan strategy can be applied to improve the surface quality and mechanical properties under cycling and monotonous loadings. In addition, this strategy homogenised the hardness distribution. However, SLM in conjunction with a remelting scan strategy increases the production time, and, consequently, the total cost of the fabrication process. Overall, the present results suggest that even though the successive remelting of the same layers increases the production time and cost, the several advantages of this strategy can compensate for the cost increase. The SLM process with a remelting scan strategy could improve the behaviour of the final parts, which will be considered as an economic benefit and a breakthrough in the field of AM.

## 6 Conclusions and future works

### 6.1 Conclusions

In the present work, the feasibility of producing chemically homogenised parts using the SLM process from elemental powder mixtures of two classes of alloys with different atomic fractions, viz. Ti6Al4V and equiatomic CoCrFeMnNi, was studied. The main results for the in-situ alloying of the two classes of alloys processed via SLM can be summarised as follows.

1. Crack-free and dense equiatomic CoCrFeMnNi and Ti6Al4V samples were fabricated by the SLM process from elemental powder mixtures, and both classes of alloys exhibited good printability. The microstructural properties of the remelted sample were similar to those of the sample fabricated from GA powder.
2. Both the classes of alloys showed an inhomogeneous distribution of the elements in the parts fabricated from powder mixtures using the SLM process. Such inhomogeneity could lead to inhomogeneity in the microstructure and mechanical and tribological properties. However, with the application of a remelting scan strategy, the elemental distribution became homogenised.
3. The effect of a remelting scan strategy on the SLM melt pool geometry, which plays a vital role in the microstructural and mechanical properties, was investigated. The prediction matched the observed values, and the melt pool depth exhibited a lower depth in the remelted than the as-built SLM samples.
4. Hardness mapping, a tool to quantify heterogeneity and understand the material behaviour, revealed variation in the hardness across the SLM parts. According to hardness distribution maps, both classes of alloys became more uniform and showed homogeneous distribution of hardness with the application of a remelting scan strategy.
5. The combined effects of the remelting scan strategy and Marangoni flow within the melt pool allow the mixing the powders so that the chemical composition, microstructure, and mechanical properties of both classes of alloys are close to that of the parts produced from pre-alloyed commercial powders.

In addition, the effects of a remelting scan strategy on the microstructural and mechanical properties, surface quality, and pore morphology of the SLM parts produced from commercial GA powders of the two classes of alloys were studied. Additionally, the effects of laser remelting on the heterogeneity in the microstructural and mechanical properties were investigated, revealing considerable advances in the understanding of the effect of this approach.

1. Increasing the number of melting steps from one to two to three increased the cooling rate of the SLM parts, which affected the microstructural and mechanical properties of the fabricated parts.
2. The application of a melting sequence led to an increase in twinning and dislocation density, which can influence the mechanical properties, such as hardness. The as-SLM Ti6Al4V parts contain a high density of dislocations because of the rapid heating/cooling and the repeated thermal cycles of the SLM process. The increase in the RS and cooling rate of the remelted samples may lead to an increase in the twins and dislocations.
3. The as-SLM samples showed the presence of LOF pores. Upon increasing the number of melting steps from one to three, the LOF pores were eliminated.



However, the spherical MPs remained. Both the size and number of pores decreased upon increasing number of melting steps.

4. Increasing the number of melting steps from one to three resulted in an improvement of the HCF strength. Discontinuities (LOF and MP) acted as nuclei for crack formation in the SM samples, while cracks were mainly initiated from the surface in DM and TM samples. In addition, the Charpy absorbed impact energy of the fabricated parts increased with an increasing number of melting steps.
5. The melting sequence decreased the wear volume and CoF in the ball-on-disk configuration for both the TCS and LCS of SLM parts. However, anisotropy was found for both the wear volume and CoF between the TCS and LCS surfaces.

The present results elucidated the possibility of in-situ alloying using the SLM process from elemental powder mixtures with different atomic fractions. A remelting scan strategy enables homogenisation of the distribution of the elemental powder particles of the in-situ alloyed materials via the SLM process. The SLM-fabricated parts from the powder mixtures can reduce the production time and cost and broadening the compositional flexibility. In addition, a remelting scan strategy can be applied to improve the microstructural and mechanical properties of SLM parts produced from GA powders. It was observed that even though the successive remelting of the same layers increases the production time and cost, the increase in the mechanical strength and homogenisation of the samples can compensate for the cost increase. Successive melting of the same layer multiple times may improve the properties of the final parts, which will improve their economic viability and represent a breakthrough in the field of AM.

## 6.2 Suggestions for future work

- 1) In all AM processes of Ti6Al4V alloys, columnar  $\beta$  grain structures are found to dominate the microstructure. A detailed study is needed to explore the grain morphology and texture of the SLM parts as a function of melting sequence, where this information is critical since the grain size plays in titanium alloys an important role in the mechanical properties.
- 2) Further research is needed to evaluate mechanical properties under cyclic and monotonic loading of in-situ alloyed materials. This information are necessary to complete existing knowledge of in-situ alloyed materials.
- 3) A detailed investigation of the substructure of HEA manufactured by the SLM is needed to reveal twin formation. This information is vital to advance knowledge about the influence of substructure on mechanical properties.
- 4) Further research is needed to reveal the influence of the location of LOF and MP in the SLM as a function of melting sequence samples, which this information is vital to advance knowledge about the HCF behaviour.

## References

- Abioye, T. E. (2019). Geometrical, microstructural and mechanical characterization of pulse laser welded thin sheet 5052-H32 aluminium alloy for aerospace applications. *Transactions of Nonferrous Metals Society of China*, 29, 667–679.
- Alfaify, A. Y. M. (2019). The effect of changing particle size distribution and layer thickness on the density of parts manufactured using the laser powder bed fusion process. PhD thesis: The university of sheffield.
- Ali, H. (2018). Effect of scanning strategies on residual stress and mechanical properties of selective laser melted Ti6Al4V. *Materials Science and Engineering A*, 712, 175–187.
- Al-rubaie, K. S. (2020). Machinability of SLM-produced Ti6Al4V titanium alloy parts. *Journal of Manufacturing Processes*, 57, 768–786.
- Antony, L. V. M. (2003). Processes for production of high-purity metal powders. *The Minerals, Metals & Materials Society*, 55, 14–18.
- Arimoto, N. (2006). New production method by gas-atomization process of titanium alloy powder. *Powder metallurgy world congress*, 1137–1140.
- ASTM F2792-12a. (2012). Standard terminology for additive manufacturing technologies. ASTM International, Harbor Drive, West Conshohocken, United States.
- Azarniya, A. (2019). Additive manufacturing of Ti–6Al–4V parts through laser metal deposition (LMD): Process, microstructure, and mechanical properties. *Journal of Alloys and Compounds*, 804, 163–191.
- Boley, C. D. (2016). Metal powder absorptivity : modeling and experiment. *Applied Optics*, 54, 2477–2482.
- Boruah, D. (2018). An analytical method for predicting residual stress distribution in selective laser melted/sintered alloys. *Residual Stresses*, 6, 283–288.
- Brodie, E. G. (2020). Remelt processing and microstructure of selective laser melted Ti25Ta. *Journal of Alloys and Compounds*, 820, 153082.
- Cao, F. (2017). The role of crack origin size and early stage crack growth on high cycle fatigue of powder metallurgy Ti-6Al-4V alloy. *International Journal of Fatigue*, 102, 45–58.
- Cao, M. (2021). The effect of homogenization temperature on the microstructure and high temperature mechanical performance of SLM-fabricated IN718 alloy. *Materials Science & Engineering A*, 801, 140427.
- Cao, S. (2018). Role of martensite decomposition in tensile properties of selective laser melted Ti-6Al-4V. *Journal of Alloys and Compounds*, 744, 357–363.
- Cao, S. (2020). On the role of cooling rate and temperature in forming twinned  $\alpha'$  martensite in Ti–6Al–4V. *Journal of Alloys and Compounds*, 813, 152247.
- Carter, L. N. (2014). The influence of the laser scan strategy on grain structure and cracking behaviour in SLM powder-bed fabricated nickel superalloy. *Journal of alloys and compounds*, 615, 338–347.
- Chen, J. (2019). Influence of laser power and scan speed on the microstructure and properties of GH4169 alloy prepared by selective laser melting. *IOP Conf. Series: Materials Science and Engineering*, 688, 033064.
- Chen, P. (2020a). Fabricating CoCrFeMnNi high entropy alloy via selective laser melting in-situ alloying. *Journal of Materials Science & Technology*, 43, 40–43.
- Chen, P. (2020b). In-situ alloyed, oxide-dispersion-strengthened CoCrFeMnNi high entropy alloy fabricated via laser powder bed fusion. *Materials & Design*, 194, 108966.

- Chen, Z. (2018). Surface roughness of selective laser melted Ti-6Al-4V alloy components. *Additive Manufacturing*, 21, 91–103.
- Cho, J. Y. (2019). Selective laser melting-fabricated Ti-6Al-4V alloy\_ Microstructural inhomogeneity, consequent variations in elastic modulus and implications. *Optics & Laser Technology* 111, 664–670.
- Coelho, B. N. (2018). A comparative study of the heat input during laser welding of aeronautical aluminum alloy AA6013-T4. *Journal of Aerospace Technology and Management*, 10, 1–12.
- Demir, A. G. (2017). Investigation of remelting and preheating in SLM of 18Ni300 maraging steel as corrective and preventive measures for porosity reduction. *International Journal of Advanced Manufacturing Technology*, 93(5–8), 2697–2709.
- Dong, Y. P. (2021). Cost-affordable Ti-6Al-4V for additive manufacturing\_ Powder modification, compositional modulation and laser in-situ alloying. *Additive Manufacturing*, 37, 101699.
- Doubenskaia, M. (2016). Parametric analysis of SLM using comprehensive optical monitoring. *Rapid Prototyping Journal*, 22, 40–50.
- Edwards, P. (2014). Fatigue performance evaluation of selective laser melted Ti-6Al-4V. *Materials Science and Engineering A*, 598, 327–337.
- Eyzat, Y. (2019). Characterization and mechanical properties of As-Built SLM Ti-6Al-4V subjected to surface mechanical post-treatment. *Procedia CIRP*, 81, 1225–1229.
- Fitzpatrick, M. E. (2005). Determination of residual stresses by X-ray diffraction. National Physical Laboratory, Teddington, Middlesex, United Kingdom.
- Fotovvati, B. (2019). Fatigue performance of selective laser melted Ti6Al4V components: State of the art. *Materials Research Express*, 6, 012002.
- Gil, F. J. (2001). Formation of a-Widmanstatten structure: Effects of grain size and cooling rate on the Widmanstatten morphologies and on the mechanical properties. *Journal of Alloys and Compounds*, 329, 142–152.
- Gorsse, S. (2017). Additive manufacturing of metals: A brief review of the characteristic microstructures and properties of steels, Ti-6Al-4V and high-entropy alloys. *Science and Technology of Advanced Materials*, 18, 584–610.
- Graça, S. (2008). Determination of dislocation density from hardness measurements in metals. *Materials Letters*, 62, 3812–3814.
- Grell, W. A. (2017). Effect of powder oxidation on the impact toughness of electron beam melting Ti-6Al-4V. *Additive Manufacturing*, 17, 123–134.
- Gu, D. (2012). Densification behavior, microstructure evolution, and wear performance of selective laser melting processed commercially pure titanium. *Acta Materialia*, 60, 3849–3860.
- Günther, J. (2017). Fatigue life of additively manufactured Ti-6Al-4V in the very high cycle fatigue regime. *International Journal of Fatigue*, 94, 236–245.
- Han, Q. (2019a). Effect of heat treatment and laser surface remelting on AlSi10Mg alloy fabricated by selective laser melting. *International Journal of Advanced Manufacturing Technology*, 102, 3315–3324.
- Han, J. (2019b). Tensile properties and serrated flow behavior of as-cast CoCrFeMnNi high-entropy alloy at room and elevated temperatures. *Metals and Materials International*, 25, 296–303.
- He, Q. (2020). Modeling and numerical studies of selective laser melting: Multiphase flow, solidification and heat transfer. *Materials & Design*, 196, 109115.

- Hrabe, N. (2019). Effects of internal porosity and crystallographic texture on Charpy absorbed energy of electron beam melting titanium alloy (Ti-6Al-4V). *Materials Science and Engineering A*, 742, 269–277.
- Huang, E. (2019). Element effects on high-entropy alloy vacancy and heterogeneous lattice distortion subjected to quasi-equilibrium heating. *Scientific Reports*, 9, 14788.
- Jamshidi, P. (2020). Selective laser melting of Ti-6Al-4V: The impact of post-processing on the tensile, fatigue and biological properties for medical implant applications. *Materials (Basel)*, 13; PMC7345457.
- Jeong, H. T. (2019). A high-temperature deformation mechanisms and processing maps of equiatomic CoCrFeMnNi high-entropy alloy. *Materials Science & Engineering*, 756, 528–537.
- Jiang, X. (2019). Heat treatment effects on microstructure-residual stress for selective laser melting AlSi10Mg. *Materials Science and Technology*, 36, 168–180.
- Joo, S. (2017). Structure and properties of ultra fine-grained CoCrFeMnNi high-Entropy alloys produced by mechanical alloying and spark plasma sintering. *Journal of Alloys and Compounds*, 698, 591–604.
- Khorasani, A. (2019). The effect of SLM process parameters on density, hardness, tensile strength and surface quality of Ti-6Al-4V. *Additive Manufacturing*, 25, 176–186.
- Kilmametov, A. (2019). High-pressure torsion driven mechanical alloying of CoCrFeMnNi high entropy alloy. *Scripta Materialia*, 158, 29–33.
- Kim, Y. (2020). Superior temperature-dependent mechanical properties and deformation behavior of equiatomic CoCrFeMnNi high-entropy alloy additively manufactured by selective laser melting. *Scientific Reports*, 1–13.
- Koutiri, I. (2018). Influence of SLM process parameters on the surface finish, porosity rate and fatigue behavior of as-built Inconel 625 parts. *Journal of Materials Processing Technology*, 255, 536–546.
- Kumar, P. (2020). High cycle fatigue in selective laser melted Ti-6Al-4V. *Acta Materialia*. 194, 305–320.
- Larimian, T. (2020). Effect of energy density and scanning strategy on densification, microstructure and mechanical properties of 316L stainless steel processed via selective laser melting. *Materials Science & Engineering A*, 770, 138455.
- Li, C. (2017). Efficient predictive model of part distortion and residual stress in selective laser melting. *Additive Manufacturing*, 17, 157–168.
- Li, P. (2009). Quantification of the interaction within defect populations on fatigue behavior in an aluminum alloy. *Acta Materialia*, 57, 3539–3548.
- Li, R. (2018). Selective laser melting of an equiatomic CoCrFeMnNi high-entropy alloy : Processability, non-equilibrium microstructure and mechanical property. *Journal of Alloys and Compounds*, 746, 125–134.
- Li, Z. (2018). Optimising the process parameters of selective laser melting for the fabrication of Ti6Al4V alloy. *Rapid Prototyping Journal*, 24, 150–159.
- Liu, B. (2019). Selective laser remelting of an additive layer manufacturing process on. *Results in Physics*, 12, 982–988.
- Liu, S. (2019). Additive manufacturing of Ti6Al4V alloy: A review. *Materials and Design*, 164, 107552.
- Liu, Z. (2017). Economic comparison of selective laser melting and conventional subtractive manufacturing processes. PhD thesis: Northeastern University Boston, Massachusetts.

- Lu, K. (2020). High-temperature low cycle fatigue behavior of an equiatomic CoCrFeMnNi high-entropy alloy. *Materials Science and Engineering: A*, 791, 139781.
- Luo, J.R. (2012). Twinning behavior of a strongly basal textured AZ31 Mg alloy during warm rolling. *Acta Materialia*, 60(5), 1986–1998.
- Masuo, H. (2018). Influence of defects, surface roughness and HIP on the fatigue strength of Ti-6Al-4V manufactured by additive manufacturing. *International Journal of Fatigue*, 117, 163–179.
- Matsagopane, G. (2019). Conceptual design framework for setting up aluminum alloy powder production system for selective laser melting (SLM) process. *Effective Production and Recycling of Powder Materials*, 71, 1840–1857.
- Melia, M. A. (2019). Mechanical and corrosion properties of additively manufactured CoCrFeMnNi high entropy alloy. *Additive Manufacturing*, 29, 100833.
- Mosallanejad, M. H. (2021). In-situ alloying in laser-based additive manufacturing processes\_ A critical review. *Journal of Alloys and Compounds*, 872, 159567.
- Mu, Y. (2020). Frictional wear and corrosion behavior of AlCoCrFeNi high-entropy alloy coatings synthesized by atmospheric plasma spraying. *Entropy*, 22, 740.
- Munitz, A. (2016). Heat treatment impacts the micro-structure and mechanical properties of AlCoCrFeNi high entropy alloy. *Journal of Alloys and Compounds*, 683, 221–230.
- Nguyen, D. S. (2020). Optimization of selective laser melting process parameters for Ti-6Al-4V alloy manufacturing using deep learning. *Journal of Manufacturing Processes*, 55, 230–235.
- Paul, H. (2009). On twinning and shear banding in a Cu-8 at.% Al alloy plane strain compressed at 77 K. *International Journal of Plasticity*, 25, 1588–1608.
- Pederson, R. (2012). Microstructure and mechanical behavior of cast Ti-6Al-4V with addition of boron. *Central European Journal of Engineering*, 2, 347–357.
- Pei, C. (2020). A damage evolution model based on micro-structural characteristics for an additive manufactured superalloy under monotonic and cyclic loading conditions. *International Journal of Fatigue*, 131, 105279.
- Peters, S. (2015). A readiness level model for new manufacturing technologies. *Production Engineering*, 9, 647–654.
- Piglione, A. (2018). Printability and microstructure of the CoCrFeMnNi high-entropy alloy fabricated by laser powder bed fusion. *Materials Letters*, 224, 22–25.
- Poorhaydari, K. (2006). Transformation twins in the weld HAZ of a low-carbon high-strength microalloyed steel. *Materials Science and Engineering A*, 435–436, 371–382.
- Qin, G. (2019a). Strengthening FCC-CoCrFeMnNi high entropy alloys by Mo addition. *Journal of Materials Science & Technology*, 35, 578–583.
- Qin, G. (2019b). CoCrFeMnNi high-entropy alloys reinforced with Laves phase by adding Nb and Ti elements. *Journal of Materials Research*, 34, 1011–1020.
- Rashid, R. (2017). Effect of scan strategy on density and metallurgical properties of 17-4PH parts printed by Selective Laser Melting (SLM). *Journal of Materials Processing Technology*, 249, 502–511.
- Rogal, Ł. (2017). CoCrFeMnNi high entropy alloy matrix nanocomposite with addition of Al<sub>2</sub>O<sub>3</sub>. *Intermetallics*, 86, 104–109.
- Salishchev, G. A. (2014). Effect of Mn and V on structure and mechanical properties of high-entropy alloys based on CoCrFeNi system. *Journal of Alloys and Compounds*, 591, 11–21.

- Sangid, M. D. (2018). Role of heat treatment and build orientation in the microstructure sensitive deformation characteristics of IN718 produced via SLM additive manufacturing. *Additive Manufacturing*, 22, 479–496.
- Sarswat, P. (2020). Design and fabrication of new high entropy alloys for evaluating titanium. *Materials*, 13, 3001.
- Schneider, J. M. (2018). Elemental segregation in an AlCoCrFeNi high-entropy alloy – A comparison between selective laser melting and induction melting. *Journal of Alloys and Compounds*, 784, 195–203.
- Senkov, O. N. (2011). Mechanical properties of Nb<sub>25</sub>Mo<sub>25</sub>Ta<sub>25</sub>W<sub>25</sub> and V<sub>20</sub>Nb<sub>20</sub>Mo<sub>20</sub>Ta<sub>20</sub>W<sub>20</sub> refractory high entropy alloys. *Intermetallics*, 19, 698–706.
- Shiomi, M. (2004). Residual stress within metallic model made by selective laser melting process. *CIRP Annals - Manufacturing Technology*, 53, 195–198.
- Simonelli, M. (2014). Effect of the build orientation on the mechanical properties and fracture modes of SLM Ti–6Al–4V. *Materials Science & Engineering A*, 616, 1–11.
- Simonelli, M. (2018). A comparison of Ti-6Al-4V in-situ alloying in Selective Laser Melting using simply-mixed and satellited powder blend feedstocks. *Materials Characterization*, 143, 118–126.
- Singh, S. (2017). Material issues in additive manufacturing: A review. *Journal of Manufacturing Processes*, 25, 185–200.
- Soare, V. (2015). Influence of remelting on microstructure, hardness and corrosion behaviour of AlCoCrFeNiTi high entropy alloy. *Materials Science and Technology*, 31, 1194–1200.
- Sutton, A. T. (2016). Powders for additive manufacturing processes: Characterization techniques and effects on part properties. *Solid Freeform Fabrication 2016: Proceedings of the 26th Annual International*, 1004–1030.
- Takao, K. (1992). Fatigue notch characteristics of commercially pure titanium. *mechanical behaviour of materials. Materials Science and Engineering: A*, 503, 15, 92–95.
- Tan, C. (2018). Selective laser melting of high-performance pure tungsten: parameter design, densification behavior and mechanical properties. *Science and Technology of Advanced Materials*, 6996, 1–11.
- Tan, P. (2021). Effects of sub-atmospheric pressure on keyhole dynamics and porosity in products fabricated by selective laser melting. *Journal of Manufacturing Processes*, 64, 816–827.
- Tong, C. J. (2005). Mechanical performance of the Al<sub>x</sub>CoCrCuFeNi high-entropy alloy system with multiprincipal elements. *Metallurgical and Materials Transactions A: Physical Metallurgy and Materials Science*, 36, 1263–1271.
- Tridello, A. (2020). Effect of microstructure, residual stresses and building orientation on the fatigue response up to 10<sup>9</sup> cycles of an SLM AlSi10Mg alloy. *International Journal of Fatigue*, 137, 105659.
- Tsai, K. Y. (2013). Sluggish diffusion in Co–Cr–Fe–Mn–Ni high-entropy alloys. *Acta Materialia*, 61, 4887–4897.
- Tsai, M. H. (2014). High-entropy alloys: A critical review. *Materials Research Letters*, 2, 107–123.
- Vaithilingam, J. (2016). The effect of laser remelting on the surface chemistry of Ti6Al4V components fabricated by selective laser melting. *Journal of Materials Processing Technology*, 232, 1–8.

- Volkov, A. N. (2017). Melt dynamics and melt-through time in continuous wave laser heating of metal films: Contributions of the recoil vapor pressure and Marangoni effects. *International Journal of Heat and Mass Transfer*, 112, 300–317.
- Vora, P. (2015). AlSi12 in-situ alloy formation and residual stress reduction using anchorless selective laser melting. *Additive Manufacturing*, 7, 12–19.
- Vora, P. (2017). Customised alloy blends for in-situ Al339 alloy formation using anchorless selective laser melting. *Technologies*, 5, 24.
- Vrancken, B. (2014). Residual stress via the contour method in compact tension specimens produced via selective laser melting. *Scripta Materialia*, 87, 29–32.
- Wallner, S. (2019). Powder production technologies. *Berg Huettenmaenn Monatsh*, 164, 108–111.
- Wang, B. (2016). Mechanical properties and microstructure of the CoCrFeMnNi high entropy alloy under high strain rate compression. *Journal of Materials Engineering and Performance*, 25, 2985–2992.
- Wang, R. (2017). Evolution of microstructure, mechanical and corrosion properties of AlCoCrFeNi high-entropy alloy prepared by direct laser fabrication. *Journal of Alloys and Compounds*, 694, 971–981.
- Wang, Y. (2020). Effect of the grain size on the corrosion behavior of CoCrFeMnNi HEAs in a 0.5 M H<sub>2</sub>SO<sub>4</sub> solution. *Journal of Alloys and Compounds*, 858, 157712.
- Warren, R. (2018). Effects of heat treatments on microstructure and properties of Ti-6Al-4V ELI alloy fabricated by electron beam melting (EBM). *Materials Science & Engineering A*, 685, 417–428.
- Wu, Z. (2018). Microstructures and mechanical properties of a welded CoCrFeMnNi high-entropy alloy high-entropy alloy. *Science and Technology of Welding and Joining*, 23, 585–595.
- Yadroitsev, I. (2009). Selective laser melting: Direct manufacturing of 3D-objects by selective laser melting of metal powders. *Applied Catalysis B: Environmental*, 75, 229–238.
- Yadroitsev, I. (2015). Evaluation of residual stress in stainless steel 316L and Ti6Al4V samples produced by selective laser melting. *Virtual and Physical Prototyping*, 10, 67–76.
- Yang, J. (2010). Experimental investigation and 3D finite element prediction of the heat affected zone during laser assisted machining of Ti6Al4V alloy. *Journal of Materials Processing Technology*, 210, 2215–2222.
- Yang, J. (2016). Formation and control of martensite in Ti-6Al-4V alloy produced by selective laser melting. *Materials & Design*, 108, 308–318.
- Yasa, E. (2010). Charpy impact testing of metallic selective laser melting parts. *Virtual and Physical Prototyping*, 5, 89–98.
- Yasa, E. (2011). The investigation of the influence of laser re-melting on density, surface quality and microstructure of selective laser melting parts. *Rapid Prototyping Journal*, 17, 312–327.
- Yeh, J. W. (2004). Nanostructured high-entropy alloys with multiple principal elements: Novel alloy design concepts and outcomes. *Advanced Engineering Materials*, 6, 299–303.
- Yeh, J. W. (2007). High-entropy alloys - A new era of exploitation. *Materials Science Forum*, 560, 1–9.
- Yin, J. (2020). Correlation between forming quality and spatter dynamics in laser powder bed fusion. *Additive Manufacturing*, 31, 100958.

- Zhang, H. (2019). Effect of post heat treatment on microstructure and mechanical properties of Ni-based composites by selective laser melting. *Materials Science & Engineering A*, 765, 138294.
- Zhao, Y. (2020). Role of operating and environmental conditions in determining molten pool dynamics during electron beam melting and selective laser melting. *Additive Manufacturing*, 36, 101559.



## Acknowledgements

Undertaking this Ph.D. has been a truly life-changing experience for me, and it would not have been possible without the support and guidance that I received from many people.

I would like to first say a very thank you to my supervisor, Prof. Prashanth Konda Gokuldoss and my co-supervisor, Dr. Lauri Kollo, for their support and encouragement. Without their guidance and constant feedback, this Ph.D. would not have been achievable.

I gratefully acknowledge the funding received towards my Ph.D. from the International the Archimedes Foundation Ph.D. fellowship for my research visit. I acknowledge the financial support from ASTRA “TUT Institutional Development Programme for 2016–2022” Graduate school of Functional Materials and Technologies (2014-2020.4.01.16-0032).

Many thanks also to Dr. Maksim Antonov for all those scientific discussions that helped improve the quality of this research. He made my access simpler to the research facilities and laboratory. It wouldn't have been possible to conduct this research without his precious support.

I gratefully give my thanks to the academic staff and experimental officers Dr. Mart Viljus, Dr. Rainer Traksmaa, Endel Esinurm, Mrs. Laivi Väljaots, Dr. Rocio Estefania Rojas Hernandez, Dr. Le Liu, Dr. Mart Saarna, Dr. Marek Tarraste, Dr. Priidu Peetsalu, Hans Vallner, Dr. Meelis Pohlak, Dr. Sergei Bereznev, Dr. Mai Uibu, and Dr. Märt Kolnes who generously passed on their hard-earned experiences and skills in metallography preparation, optical and electron microscopy, mechanical testing, XRD and so on. I was deeply impressed by their not showing any tiredness even though I made countless mistakes and asked many fundamental questions.

I would like to thank Prof. Ilona Oja Acik, Prof. Irina Hussainova, Prof. Jakob Kübarsepp, Prof. Kristo Karjust, Prof. Renno Veinthal, Prof. Fjodor Sergejev, supporting and guiding me during my research.

I would also like to thank the Departments of Mechanical and Industrial Engineering at the Tallinn University of Technology for administrative support.

I would like to thank my friends and colleagues, Dr. Nikhil Kumar Kamboj, Dr. Ramin Rahmani, Dr. Tatevik Minasyan, Miss. Mina Shahin, Rahul Kumar, Dr. Ali Saffar Shamshirgar, Navid Alinejadian, Dr. Raghunandan Ummethala, Dr. Yaroslav Holovenko, Dr. Neera Singh, Valerie Goettgens, Dr. Philipp Mair, Simon Bergmüller, Dr. Lukas Kaserer, without whose assistance I would not have been able to complete this work in its entirety.

I wish to convey my sincere gratitude to Prof. Gerhard Leichtfried for accepting me as a visiting PhD student, his tremendous support and supervision.

I would like to acknowledge my father, who died in a tragic car crash before the completion of my education, for his great role in my life, and I know he would be proud of me. I would also like to say a heartfelt thank you to my mom, brothers, and sisters for their endless support and encouragement.

And finally, my warm and heartfelt thanks to my wife, Mahtab Shahin, who has been by my side throughout this Ph.D., living every single minute of it, and without whom, I would not have had the courage to embark on this journey in the first place.

Javad Karimi  
Tallinn, August 2022

## Abstract

### Microstructural Homogenisation of Selective Laser Melted Ti6Al4V and CoCrFeMnNi High-Entropy Alloys

Selective laser melting (SLM) is one of the most widely used additive manufacturing (AM) processes, which offer the possibility of fabricating parts with a high resolution of features, high-dimensional control, and almost unlimited complexity from atomised powders. The microstructural and mechanical properties and surface quality of SLM-fabricated parts can be tuned by varying the process parameters (such as the scanning strategy) to produce parts with desired properties. In contrast to those obtained using traditional manufacturing processes, materials with different microstructural and mechanical properties can be obtained using SLM owing to the rapid solidification and complex thermal cycles. However, SLM manufacturing costs from atomised commercial powders are relatively high due to the limited number of commercially available alloys, costly and time-consuming powder production, specific expertise requirements, and other challenges. Metallic alloys that can be processed by SLM exhibit different technology readiness levels; furthermore, SLM parts exhibit inhomogeneity in the microstructural and mechanical properties and poor reliability and surface quality. In this work, two alloy classes with different atomic fractions, namely, Ti6Al4V and CoCrFeMnNi high-entropy alloys (HEA), were in-situ alloyed via SLM. This alloying strategy provided high flexibility and circumvented the consumption of a large amount of pre-alloyed materials, thereby reducing resource wastage. The microstructural and mechanical properties of the SLM parts fabricated from in-situ alloyed materials were studied and compared with those fabricated of the SLM parts from pre-alloyed gas-atomised (GA) powders. The effect of the remelting scan strategy on the inhomogeneity in the microstructural and mechanical properties of the SLM parts was investigated. In addition, the effect of the melting sequence on the substructure, including twinning and dislocation density, was investigated. The influence of laser remelting on the mechanical properties, including tension, compression, impact, hardness, and high cycle fatigue, was systematically studied. The influence of the remelting scan strategy on the anisotropy in wear behaviour and residual stress (RS) of the parts fabricated by SLM was investigated. The effects of laser remelting on defects such as porosity were also studied. The results showed that in-situ high-entropy CoCrFeMnNi and Ti6Al4V alloyed via SLM comprised inhomogeneous distributions of mixed elements. However, the elemental distributions turned homogeneous with the application of remelting. The microstructural and mechanical properties of the remelted sample were similar to those of the sample fabricated from GA powder. With increasing number of melting steps, the hardness distribution of the as-built SLM sample (from GA and mixed elemental powders) turned homogeneous; tensile, compressive, impact, and high cycle fatigue strengths increased; the density of twins and dislocations increased, which could affect the mechanical properties; and the wear volume decreased, while anisotropy was observed between the transverse and longitudinal cross-sections.

The SLM process from pre-alloyed powders exhibits significant shortcomings, such as rigid chemical composition, a limited number of available commercial alloys, resource-demanding and time-consuming production process, production issues, required expertise, etc. The SLM parts exhibit relatively high surface roughness, poor performance under cyclic loading, anisotropy and inhomogeneity in microstructure and mechanical properties, defects (pores and cracks) and high residual stress. The aims of

the present thesis are to investigate the feasibility of producing compositionally homogenous without resorting to gas-atomized alloy powders but using different powders systems, namely elemental powders mixtures corresponding to the Ti6Al4V (heavily studied in the context of AM) and equiatomic CoCrFeMnNi HEA (recently developed class of alloys). This strategy can reduce the production time and cost, and broadening the compositional flexibility. The printability of in-situ alloyed materials, Ti-6Al-4V and CoCrFeMnNi HEA, were investigated, which these alloys have attracted tremendous attention from researchers and engineers due to their interesting properties such as excellent corrosion resistance and good thermal stability. Chemically homogenized HEA in equiatomic composition was successfully in-situ alloyed via SLM from the elemental powders mixtures. The SLM Ti6Al4V was fabricated with tunable microstructure and mechanical properties. The tribological and mechanical properties, including wear behavior, tensile and compressive strength, high cycle fatigue strength, hardness, and Charpy impact energy of SLM parts, were improved. The effect of cooling rate on the substructure (dislocation density) of selective laser melted parts and its correlation with the mechanical properties were investigated. The depth of the melt pool size was predicted, which matched the experimental results. The present results proved the possibility of in-situ alloying using SLM from elemental powder mixtures with high atomic fractions. Laser remelting enables homogenization distribution of the elements of the in-situ alloyed materials. Hence, this technique can reduce the production time and cost, and broadening the compositional flexibility. Even though the successive laser remelting increases the time and cost of production, the improvement in reliability, mechanical properties, and homogenization of the samples can compensate for the cost increase. Successive melting of the same layer multiple times may improve homogenizing the powder bed, which will be considered as an economic benefit and a huge relief and breakthrough in the field of additive manufacturing.

## Lühikokkuvõte

# Selektiivse lasersulatuse teel valmistatud Ti6Al4V ja kõrgentroopse CoCrFeMnNi sulamite mikrostruktuuri homogeniseerimine

Selektiivne lasersulatus (SLM) on üks enim kasutatavaid kihtlisandustootmis protsesse, mis võimaldab toota atomiseeritud metallipulbritest suure täpsusega osi, mille kuju võib olla peaaegu piiramatut keerukas. SLM-i valmistatud komponentide mikrostruktuuri ja mehaanilisi omadusi ning pinnakvaliteeti saab häälestada ka protsessi parameetrite (nagu skaneerimisstrateegia) muutmisega, luues võimaluse ka muuta detaili erinevaid omadusi. SLM-protsessis saab traditsiooniliste tootmisprotsessidega võrreldes kiire tahkumise ja keeruliste termiliste tsüklite tõttu luua erineva mikrostruktuuri ja mehaaniliste omadustega materjale. Kaubandusliku gaasatomiseeritud pulbri SLM-i tootmiskulud on aga suhteliselt kõrged, kuna saadaval on piiratud arv kaubanduslikke sulameid. Lisaks kulukas ja aeganõudev pulbri tootmisprotsess, nõutavad eelteadmised ja muud väljakutsed. Erinevatel metallisulamitel, mida saab SLM-iga töödelda, on erinev tehnoloogia küpsusaste või tehnoloogia valmisoleku tase (TRL). Tihti kaasneb SLM meetodil toodetud detailidel mikrostruktuuri ja mehaaniliste omaduste ebaühtlus, samuti madal töökindlus ja pinnakvaliteet.

Käesolevas töös legeriti in-situ SLM-i meetodil kahte erineva TRL-i ja aatomfraktsiooniga sulamiklassi – Ti6Al4V ja CoCrFeMnNi kõrgentroopseid sulamid (HEA), kus printimisel toimuv legerimine tagab suurema paindlikkuse ning väldib vajadust eellegeeritud materjalide järele. Uuriti in-situ legeeritud materjalidest valmistatud SLM-i katsekehade mikrostruktuuri ja mehaanilisi omadusi ning võrreldi neid vastavalt eellegeeritud gaaspihustatud pulbritest valmistatud detailidega. Uuriti übersulatusskaneerimise strateegia mõju SLM-i detailide mikrostruktuuri ja mehaaniliste omaduste ebahomogeensusele. Uuriti sulatamisjärjestuse mõju alamstruktuuridele, sealhulgas kahestumistasandite ja dislokatsioonide kontsentratsioonile. Süstemaatiliselt uuriti laseri übersulatamise mõju mehaanilistele omadustele, sealhulgas tõmbele ja survele, löögisitkusele, kõvadusele ja kõrgtsükllilise väsimusele. Uuriti übersulatusskaneerimise strateegia mõju SLM-i teel valmistatud detailide kulumiskäitumise anisotroopiale ja jääkpingele. Uuriti ka laseri übersulatamise mõju poorsusele. Tulemused näitasid, et ühekordse SLM-i kaudu legeeritud in-situ CoCrFeMnNi HEA ja Ti6Al4V koosnesid segatud elementide ebahomogeensest jaotumisest. Teisest küljest homogeniseeriti elementide jaotus kasutades übersulatamist. Übersulatatud proovi mikrostruktuur ja mehaanilised omadused on võrreldavad gaasatomiseeritud pulbri valmistatud proovide mikrostruktuuri ja mehaaniliste omadustega. SLM-i teel pihustatud ja segatud pulbritest valmistatud detailide kõvadusjaotus homogeniseeriti suureneva arvu sulamistega. Tõmbe-, surve- ja löögitugevus suurenesid sulatamisetappide arvu suurenemisega. Kõrgtsüklliline väsimustugevus paranes sulamiste arvu suurenemisega. Kahestumistasandite ja dislokatsioonide tihedus suurenes übersulatamisega, mis võis samuti mõjutada mehaanilisi omadusi. Kulumiskindlus übersulatamisega kaasnevalt suurenes, samas kui TCS-i ja LCS-i vahel leiti anisotroopia.

Eellegeeritud pulbritest valmistatud SLM-i protsessil on olulisi puudujääke, nagu raskesti muudetav keemiline koostis, piiratud arv saadaolevaid kaubanduslikke sulameid, ressursinõudlik ja aeganõudev tootmisprotsess, nõutavad teadmised jne.

SLM meetodil valmistatud detailidel on suhteliselt kõrge pinnakaredus, madal vastupanu tsüklilisele koormusele, mikrostruktuuri ja mehaaniliste omaduste anisotroopsus ja ebahomogeensus, defektid (poorid ja praod) ning kõrged jääkpinged. Käesoleva lõputöö eesmärgiks on uurida, kas on võimalik toota koostiselt homogeenseid materjali nii, et ei peaks kasutama eellegeritud sulamipulbreid, kuid kasutades elementaarpulbrite segusid, mis vastavad Ti6Al4V-le (AM kontekstis palju uuritud) ja ekvaatomilisele HEA-le (hiljuti välja töötatud sulamite klass). See strateegia võib vähendada tootmisaega ja -kulusid ning laiendada kompositsiooni paindlikkust. Ti-6Al-4V ja CoCrFeMnNi HEA valiti prinditavuse uurimiseks, kuna need sulamid on pälvinud teadlaste ja inseneride poolt tohutut tähelepanu tänu nende huvitavatele omadustele, nagu suurepärase korrosioonikindlus ja hea termiline stabiilsus. Keemiliselt homogeniseeritud HEA võrdse aatomilise koostisega legeriti edukalt in situ SLM-i kaudu elementaarpulbrite segudest. SLM Ti6Al4V valmistati häälestatava mikrostruktuuri ja mehaaniliste omadustega. SLM-osade triboloogilisi ja mehaanilisi omadusi, sealhulgas kulumiskäitumist, tõmbe- ja survetugevust, kõrgtsüklilist väsimustugevust, kõvadust ja Charpy purunemissitkust parandati. Uuriti jahutuskiiruse mõju selektiivsete laseriga sulatatud detailide alusstruktuurile (dislokatsioonitihedusele) ja selle seost mehaaniliste omadustega. Hinnati sulavanni sügavust, mis ühtis katsetulemustega. Käesolevad tulemused tõestasid in-situ legerimise võimalikkust, kasutades SLM-i. Laser-übersulatamine võimaldab in-situ legeritud materjalide elementide homogeniseerimist. Seega võib see tehnika vähendada tootmisaega ja -kulusid ning laiendada kompositsiooni paindlikkust. Kuigi järjestikune laseri übersulatamine suurendab tootmise aega ja kulusid, võib proovide töökindluse, mehaaniliste omaduste ja homogeniseerimise paranemine kompenseerida kulude kasvu. Sama kihi mitmekordne sulatamine võib parandada pulbrikihi homogeniseerimist, mida peetakse majanduslikuks kasuks ning tohutuks kergenduseks ja läbimurdeks metallide kihtlisandustehnoloogiate valdkonnas.

# Appendix

## Paper I

**Karimi, J.**, Ma, P., Jia, Y. D., & Prashanth, K. G. (2020). Linear patterning of high entropy alloy by additive manufacturing. *Manufacturing Letters*, 24, 9–13.





Contents lists available at ScienceDirect

## Manufacturing Letters

journal homepage: [www.elsevier.com/locate/mfglet](http://www.elsevier.com/locate/mfglet)

## Linear patterning of high entropy alloy by additive manufacturing

J. Karimi<sup>a,\*</sup>, P. Ma<sup>b</sup>, Y.D. Jia<sup>c</sup>, K.G. Prashanth<sup>a,d,e,\*</sup><sup>a</sup> Department of Mechanical and Industrial Engineering, Tallinn University of Technology, 19086 Tallinn, Estonia<sup>b</sup> School of Materials Engineering, Shanghai University of Engineering Science, Shanghai 201620, China<sup>c</sup> School of Materials Science and Engineering, Shanghai University, Shanghai 200444, China<sup>d</sup> Erich Schmid Institute of Materials Science, Austrian Academy of Sciences, Jahnstrasse 12, A-8700 Leoben, Austria<sup>e</sup> CBCMT, School of Mechanical Engineering, Vellore Institute of Technology, Vellore 632014, Tamil Nadu, India

## ARTICLE INFO

## Article history:

Received 25 November 2019

Received in revised form 18 January 2020

Accepted 4 March 2020

Available online 5 March 2020

## Keywords:

High entropy alloys

Layered microstructure

Selective laser melting

Additive manufacturing

## ABSTRACT

An equimolar AlCoCrFeNi high-entropy alloy (HEA) was synthesized using selective laser melting (SLM). XRD patterns show peaks of a single-phase BCC structure typical for a HEA. The process parameters were optimized carefully in such a way that a layered microstructure with gaps of controllable size (average size  $\sim 67 \pm 1 \mu\text{m}$ ) is obtained. The size of the gaps can be controlled using the process parameters and the hatch distance. SLM may be the only process that can process such unique microstructures (linear patterns), where their unique properties may be used as filters in extreme environments like corrosion, temperature, nuclear, etc.

© 2020 Society of Manufacturing Engineers (SME). Published by Elsevier Ltd. All rights reserved.

## 1. Introduction

Recently, additive manufacturing (AM) has attracted the attention in fabrication of metallic materials [1,2]. Laser-based powder bed fusion process or Selective laser melting (SLM) is one of the AM processes that produce complex metallic components by selectively melting micron-sized powder in a layer-by-layer fashion under a protective atmosphere, using a computer controlled laser beam [3–5]. SLM can fabricate wide variety of metallic materials from Al-based [6–8], Ti-based [9–11], Ni-based [12,13], Fe-based [14–16], Cu-based [17], Co-based [18] alloys and other classes of materials like metallic glasses [14,19] and high entropy alloys (HEA) [20]. HEAs are generally manufactured by casting or powder metallurgy routes. SLM has a great potential for the fabrication of HEA with complex shapes and added functionalities [21,22].

Traditionally, conventional metallurgical theory suggests that multiple alloying elements in an alloy could result in the formation of intermetallic phases with complex microstructure. However, recently, since the development of HEAs (material with at least five principle elements), the research in the field of HEA is accelerated due to the interesting properties of HEAs [23–39]. They have significantly higher mixing entropies than those in conventional alloys.

Generally, transition metals like Al, Mn, Fe, Cr, Co, Cu, Ti, V and Ni have been used in the formation of HEAs [23–29]. HEAs have excellent mechanical strength even at elevated temperatures. In addition, HEAs exhibit outstanding resistance to oxidation and wear, fatigue and fracture resistance, and toughness [30–40]. HEAs can be used as thermoelectric, hydrogen storage, radiation resistant, electromagnetic shielding, and soft magnetic material [30–40]. Various synthesis routes such as arc melting [41,42], spark plasma sintering [42,43], direct laser fabrication [44,45], have been utilized to fabricate HEAs. Recently, additive manufacturing processes were employed successively to produce HEA, which offer the additional advantage of producing HEAs with intricate shapes and added functionalities [46].

Layered and porous structures provide unique properties that can be utilized in several applications (for instance filters, energy absorption/crash resistant applications, etc.) [47]. HEA may be produced as layered/porous structure using AM, where both the benefits of HEAs and layered structure can be utilized. SLM process can not only produce HEAs but can also fabricate layered structures in a precisely controlled fashion. Such materials have potential applications in the field of biology, metallurgy, chemical, petroleum and nuclear industries, etc. In the present study, pre-alloyed powders were used to fabricate HEA using SLM. Layered microstructure with differing gap sizes were fabricated and the size of the gaps were controlled precisely using hatch gap and hatch overlaps for advanced filter based applications.

\* Corresponding authors at: Department of Mechanical and Industrial Engineering, Tallinn University of Technology, 19086 Tallinn, Estonia (K.G. Prashanth).

E-mail addresses: [jkarim@taltech.ee](mailto:jkarim@taltech.ee) (J. Karimi), [kgprashanth@gmail.com](mailto:kgprashanth@gmail.com) (K.G. Prashanth).



## 2. Experimental methods

FeCoNiCrAl-based HEA specimens with equimolar composition were manufactured using a Realizer SLM50 equipped with a 120 W Yb-YAG laser with a spot size of  $\sim 30 \mu\text{m}$ . HEA powders were manufactured using gas atomization process. A layer thickness of  $25 \mu\text{m}$  and varying hatch distance  $50\text{--}80 \mu\text{m}$  was used for the experiments [48]. A Zeiss FEG scanning electron microscope was used for the characterization of microstructure. The crystalline structure was characterized using X-ray diffractometer Bruker-axes D5005 with a  $0.05^\circ$  step size along the direction of deposition. The microhardness measurements were performed on a MICRO-MET 2001 machine with 200 g and 50 g loads for SLM sample and powders respectively with 10 s dwell time. The powder particles are embedded with cold mount and the surface was polished to have a smooth surface, before the hardness of the powders were measured. The hardness of the bulk samples were measured along the edges to maintain the integrity of the samples. HORIBA LA-950 used to measure the powder particle size.

## 3. Results and discussion

Powder morphology and their size distribution are shown in Fig. 1. The powder is nearly spherical and some satellite particles are also observed (Fig. 1(a)). From the frequency vs. particle diameter plot (Fig. 1(b)), it can be observed that the powder show a narrow distribution with  $D_{10} \sim 27 \mu\text{m}$  and  $D_{90} \sim 65 \mu\text{m}$ . Nearly, all of the particles are spherical and the diameter of most particles are equivalent to or below  $44 \mu\text{m}$  ( $D_{50}$ ).

Fig. 2 shows the diffraction pattern of the HEA powder and SLM sample, where both of the patterns show the presence of single bcc phase, corroborating HEA structure [49,50]. However, the presence of a weak crystallographic texture is observed between the two patterns. The crystallite size and lattice strain of the powder and the SLM samples are observed to be  $120 \pm 10 \text{ nm}$ ,  $16.8 \pm 12 \text{ nm}$  and  $0.21 \pm 0.10$ ,  $0.47 \pm 0.11\%$ , respectively. Both the reduction of crystallite size and the increase in the strain of the material led to the broadening of the XRD peaks in the SLM sample. In addition, the dislocation density in the SLM sample was found to be in the order of  $3 \times 10^{14} \text{ m}^{-2}$ , which is approximately two orders of magnitude higher than in the cast counterparts, which also corroborates to the high internal strain in the SLM processed material.

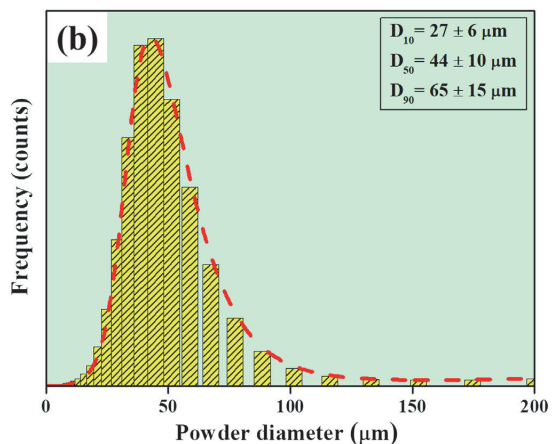
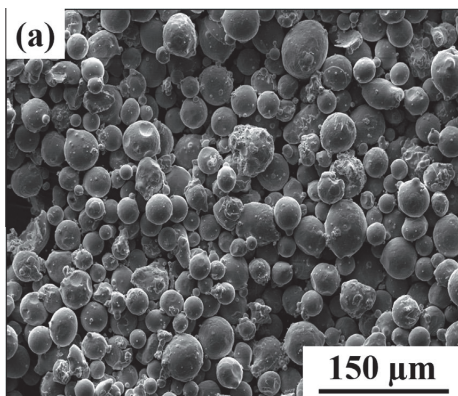


Fig. 1. (a) Scanning electron microscopy image of the AlCoCrFeNi powder, (b) High entropy alloy powder histogram showing frequency vs. particle diameter.

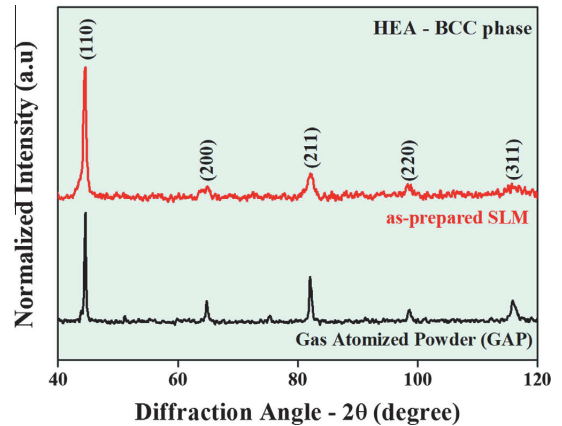


Fig. 2. X-ray diffraction patterns of the high entropy alloy gas atomized powder and SLM processed sample.

Fig. 3 shows the presence of a layered/porous microstructure with defined gap between the melt tracks/hatches. The width of the melt pool was found to be  $\sim 80 \pm 5 \mu\text{m}$  and a gap of  $\sim 66 \pm 3 \mu\text{m}$  was placed between the two melt tracks. The melt tracks are connected with their subsequent layers and hence do not fall apart. The characteristic of such layered/porous structure is that the gap between the melt pools can be controlled precisely using the hatch distance and hatch overlaps, which indirectly related with volumetric energy density (VED) [48]. The VED is inversely proportional to the hatch distance provided laser power, laser scan speed and layer thickness are help constant. The average microhardness for the powder and fabricated samples are found to be  $400 \pm 40$ ,  $541 \pm 18 \text{ Hv}$ , respectively. The hardness of SLM sample is found to be much higher than their cast and EBM counterparts [51].

The SEM images of FeCoNiCrAl SLM samples produced as a function of varying hatch distance ( $50\text{--}80 \mu\text{m}$ ) and hatch offset of  $50 \mu\text{m}$  is shown in Fig. 4. In the first three samples (Fig. 4(a-c)), the hatch distance was kept constant, but the VED was varied. The sample in Fig. 4(a) was fabricated with the highest VED and the sample in Fig. 4(c) with the least VED. The samples in Fig. 4(a,b)

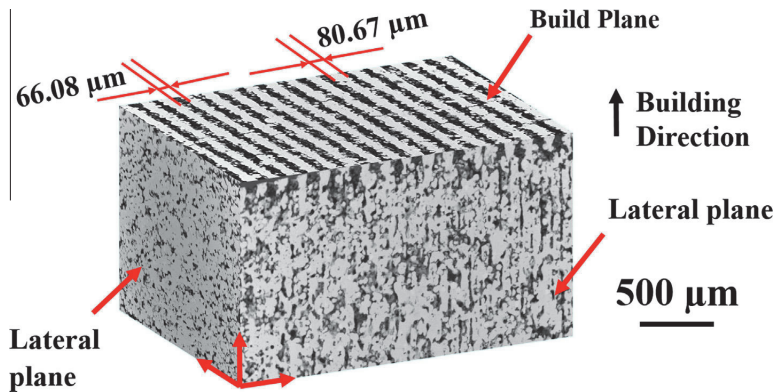


Fig. 3. 3-Dimensional scanning electron microscopy section of the high entropy alloy sample fabricated by SLM. The arrow (upped right) indicated the building direction.

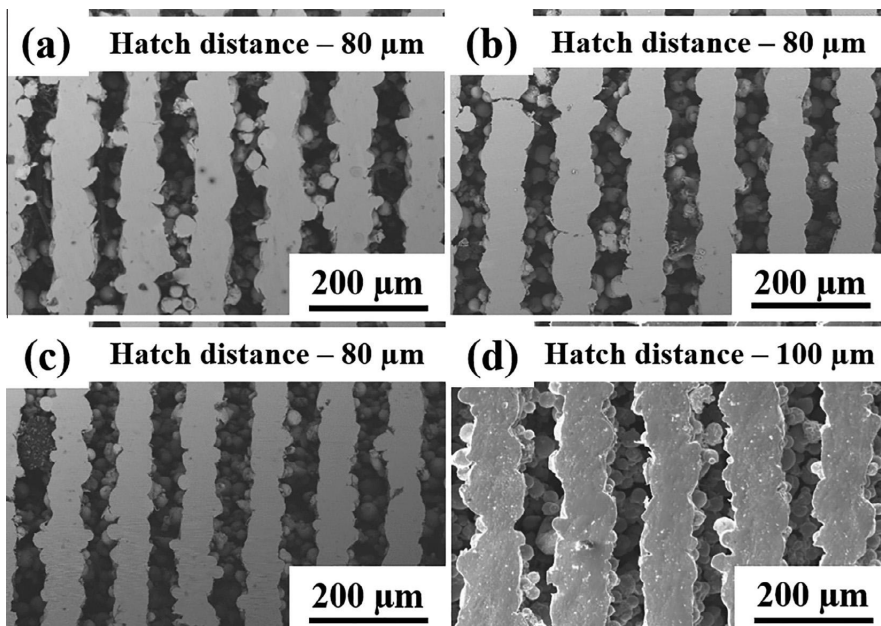


Fig. 4. Scanning electron microscopy images of the FeCoNiCrAl high entropy alloy SLM samples obtained at: hatch distance of 80  $\mu\text{m}$  for (a), (b), and (c) but varying volumetric energy density and (d) hatch distance is increased to 100  $\mu\text{m}$ .

show similar laser track width ( $\sim 80 \pm 5 \mu\text{m}$ ) and the sample in Fig. 4(c) show slightly thinner laser track width ( $\sim 70 \pm 5 \mu\text{m}$ ). Since the laser tracks are thinned in sample with lower VED, the gaps are wider ( $\sim 80 \pm 3 \mu\text{m}$ ) and are more uniform. The sample with least VED (Fig. 4(c)) show more amount of porosity than then other two samples with higher VED. On the other hand, the samples in Fig. 4(a,b) show the presence of some minor cracks, which is absent in sample with least VED (Fig. 4(c)), which may be corroborated to the fact that increase in the VED increase the cooling rate and hence prone to cracking. Fig. 4(d) shows the SEM images of FeCoNiCrAl SLM sample with increase hatch distance (100  $\mu\text{m}$ ). It can be observed that the width of the laser track increases ( $\sim 100 \pm 8 \mu\text{m}$ ) reducing the size of the gap to  $\sim 25 \pm 5 \mu\text{m}$ . It can be observed from these samples that the hatch distance has a direct influence on the

width of the laser tracks. The changes in the VED just have a minor influence on the laser track width. This suggests that the width of the gap and the laser track can be predominantly manipulated by changing the width of the hatch and the overlap between two hatches.

The present results suggest that SLM can not only produce HEA (with single bcc phase), but also can define the space/gaps between two melt tracks/laser track in an accurate fashion – linear patterning. Typical additive manufacturing structures were not used to create gaps between the laser melt tracks. SLM has a cutting edge advantage over other manufacturing processes for fabricating such that HEA filters with defined gaps, where the parameter combination of hatch distance and hatch overlap, especially hatch overlap (in a positive or negative way) to either increase the gap between

the laser melt tracks or to decrease the gaps. Such HEA sample with added functionalities, fabricated with defined gap widths can be used for filter application in extreme environments (corrosion, temperature and nuclear) to reap the benefits of both HEA (in terms of properties) and additive manufacturing (in terms of gaps).

#### 4. Summary

The present study explores the possibility of fabricating HEA using an additive manufacturing process like the SLM with linear patterns. The prepared high-entropy alloy is featured by the characteristics of a layered/porous microstructure, with a defined and controllable gap size of ~66 µm between two melt tracks. The size of the gap has a touching relation with the width of the hatch, which defines the size of the melt pool (laser tracks). Such materials with definable gap between laser tracks can be effectively used as filters in extreme environments, reaping the benefits of both additive manufacturing (creating defined gaps between laser tracks) and HEA (sluggish diffusion and hence resistant to corrosion and high temperature). Additive manufacturing can be the only technology that can produced parts with such defined gaps between two melt tracks. The present results open the door for novel next generation filters for extreme environments (oxidation, temperature, nuclear, etc.) by combining HEA and additive manufacturing.

#### Declaration of Competing Interest

The authors declare that they have no known competing financial interests or personal relationships that could have appeared to influence the work reported in this paper.

#### Acknowledgements

The authors would like to thank Mr. Rainer Traksmas and Ms. Laivi Väiljaots for technical assistance. The financial assistance from the European Regional Development Fund through project MOBERC15 is acknowledged.

#### References

- DebRoy T, Wei HL, Zuback JS, Mukherjee T, Elmer JW, Milewski JO, et al. Additive manufacturing of metallic components – Process, structure and properties. *Prog Mater Sci* 2018;92:112–224.
- Herzog D, Seyda V, Wycisk E, Emmelmann C. Additive manufacturing of metals. *Acta Mater* 2016;117:371–92.
- Prashanth KG, Scudino S, Klauss HJ, Surreddi KB, Löber L, Wang Z, et al. Microstructure and mechanical properties of Al-12Si produced by selective laser melting: Effect of heat treatment. *Mater Sci Eng A* 2014;590:153–60.
- Schwab H, Prashanth KG, Löber L, Kühn U, Eckert J. Selective laser melting of Ti-45Nb alloy. *Metals* 2015;5:686–94.
- Prashanth KG. Design of next-generation alloys for additive manufacturing. *Mater Des Process Comm* 2019;1:19–22.
- Prashanth KG, Damodaram R, Scudino S, Wang Z, Prasad Rao K, Eckert J. Friction welding of Al-12Si parts produced by selective laser melting. *Mater Des* 2014;57:632–7.
- Prashanth KG, Scudino S, Chaubey AK, Löber L, Wang P, Attar H, et al. Processing of Al-12Si-TiNi composites by selective laser melting and evaluation of compressive and wear properties. *J Mater Res* 2016;31:55–65.
- Ma P, Jia Y, Prashanth KG, Scudino S, Yu Z, Eckert J. Microstructure and phase formation in Al-20Si-5Fe-3Cu-1Mg synthesized by selective laser melting. *J Alloys Compd* 2016;657:430–5.
- Attar H, Prashanth KG, Zhang LC, Calin M, Okulov IV, Scudino S, et al. Effect of powder particle shape on the properties of in situ Ti-TiB composite materials produced by selective laser melting. *J Mater Sci Technol* 2015;31:1001–5.
- Attar H, Löber L, Funk A, Calin M, Zhang LC, Prashanth KG, et al. Mechanical behavior of porous commercially pure Ti and Ti-TiB composite materials manufactured by selective laser melting. *Mater Sci Eng A* 2015;625:350–6.
- Prashanth KG, Damodaram R, Maity T, Wang P, Eckert J. Friction welding of selective laser melted Ti6Al4V parts. *Mater Sci Eng A* 2017;704:66–71.
- Jia Q, Gu D. Selective laser melting additive manufacturing of Inconel 718 superalloy parts: Densification, microstructure and properties. *J Alloys Compd* 2014;585:713–21.
- Konečná R, Nicoletto G, Kunz L, Bača A. Microstructure and directional fatigue behavior of Inconel 718 produced by selective laser melting. *Procedia Struct Integr* 2016;2:2381–8.
- Jung HY, Choi SJ, Prashanth KG, Stoica M, Scudino S, Yi S, et al. Fabrication of Fe-based bulk metallic glass by selective laser melting: A parameter study. *Mater Des* 2015;86:703–8.
- Prashanth KG, Löber L, Klauss HJ, Kühn U, Eckert J. Characterization of 316L steel cellular dodecahedron structures produced by selective laser melting. *Technologies* 2016;4:34.
- Casati R, Lemke J, Vedani M. Microstructure and fracture behavior of 316L austenitic stainless steel produced by selective laser melting. *J Mater Sci Technol* 2016;32:738–44.
- Scudino S, Unterdorfer C, Prashanth KG, Attar H, Ellendt N, Uhlenwinkel V, et al. Additive manufacturing of Cu-10Sn bronze. *Mater Lett* 2015;156:202–4.
- Qian B, Saeidi K, Kvetková L, Lofaj F, Xiao C, Shen Z. Defects-tolerant Co-Cr-Mo dental alloys prepared by selective laser melting. *Dental Mater* 2015;31:1435–44.
- Pauly S, Löber L, Petters R, Stoica M, Scudino S, Kühn U, et al. Processing metallic glasses by selective laser melting. *Mater Today* 2013;16:37–41.
- Xu Z, Zhang H, Li W, Mao A, Wang L, Song G, et al. Microstructure and nanoindentation creep behavior of CoCrFeMnNi high-entropy alloy fabricated by selective laser melting. *Additive Manuf* 2019;28:766–71.
- Rao H, Giet S, Yang K, Wu X, Davies CHJ. The influence of processing parameters on aluminum alloy A357 manufactured by selective laser melting. *Mater Des* 2016;109:334–46.
- Thijs L, Verhaeghe F, Craeghs T, Humbeek VJ, Kruth JP. A study of the microstructural evolution during selective laser melting of Ti-6Al-4V. *Acta Mater* 2010;58:3303–12.
- Cantor B. Multicomponent and high entropy alloys. *Entropy* 2014;16:4749–68.
- Yang HH, Tsai WT, Kuo JC. Effect of pre-oxidation on increasing resistance of Fe-Al-Ni-Cr-Co-Mn high-entropy alloys to molten Al attack. *Corr Eng Sci Technol* 2013;49:124–9.
- Munitz A, Salhov S, Hayun S, Frage N. Heat treatment impacts the microstructure and mechanical properties of AlCoCrFeNi high entropy alloy. *J Alloys Compd* 2016;683:221–30.
- Tang Z. Processing, microstructures, and mechanical behavior of high-entropy alloys master's dissertation. Knoxville: The University of Tennessee; 2012.
- Tsai MH. Physical properties of high entropy alloys. *Entropy* 2013;15:5338–45.
- MacDonald BE, Fu Z, Zheng B, Chen W, Lin Y, Chen F, et al. Recent progress in high entropy alloy research. *JOM* 2017;69:2024–31.
- Tsai MH, Yeh JW. High-entropy alloys: A critical review. *Mater Res Lett* 2014;2:107–23.
- Eißmann N, Klöden B, Weißgärber T, Kieback B. High-entropy alloy CoCrFeMnNi produced by powder metallurgy. *Powder Metall* 2017;60:184–97.
- Zhou Y, Zhang Y, Wang Y, Chen G. Microstructure characterization of Al<sub>x</sub>(TiVCrMnFeCoNiCu)<sub>100-x</sub> high-entropy alloy system with multi-principal elements. *Rare Met Mater Eng* 2007;36:2136–9.
- Chuang MH, Tsai MH, Wang WR, Lin SJ, Yeh JW. Microstructure and wear behavior of Al<sub>x</sub>Co<sub>1.5</sub>CrFeNi<sub>1.5</sub>Ti<sub>y</sub> high-entropy alloys. *Acta Mater* 2011;59:6308–17.
- Laplanche G, Volkert UF, Eggeler G, George EP. Oxidation behavior of the CrMnFeCoNi high-entropy alloy. *Oxid Met* 2016;85:629–45.
- Butler TM, Weaver ML. Oxidation behavior of arc melted AlCoCrFeNi multi-component high-entropy alloy. *J Alloys Compd* 2016;674:229–44.
- Shafeie S, Guo S, Hu Q, Fahliquist H, Erhart P, Palmqvist A. High entropy alloys as high-temperature thermoelectric materials. *J Appl Phys* 2015;118:184905.
- Kao YF, Chen SK, Sheu JH, Lin JT, Lin WE, Yeh JW, et al. Hydrogen storage properties of multi-principal-component CoFeMnTi<sub>x</sub>V<sub>y</sub>Zr<sub>z</sub> alloys. *Int J Hydrogen Energy* 2010;35:9046–59.
- MacDonald BE, Fu Z, Wang X, Li Z, Chen W, Zhou Y, et al. Influence of phase decomposition on mechanical behavior of an equiatomic CoCuFeMnNi high entropy alloy. *Acta Mater* 2019;181:25–35.
- Fujieda T, Shiratori H, Kuwabara K, Hirota M, Kato T, Yamanaka K, et al. CoCrFeNiTi-based high-entropy alloy with superior tensile strength and corrosion resistance achieved by a combination of additive manufacturing using selective electron beam melting and solution treatment. *Mater Lett* 2017;189:148–51.
- Lee C, Song G, Gao MC, Feng R, Chen P, Brechtl J, et al. Lattice distortion in a strong and ductile refractory high entropy alloy. *Acta Mater* 2018;160:158–72.
- Chao Q, Guo T, Jarvis T, Wu X, Hodgson P, Fabijanic D. Direct laser deposition cladding of AlxCoCrFeNi high entropy alloys on a high-temperature stainless steel. *Surf Coatings Technol* 2017;332:440–51.
- Chou HP, Chang YS, Chen SK, Yeh JW. Microstructure, thermophysical and electrical properties in Al<sub>x</sub>CoCrFeNi (0 ≤ x ≤ 2) high entropy alloys. *Mater Sci Eng B* 2009;163:184–9.
- Joseph J, Jarvis T, Wu X, Stanford N, Hodgson P, Fabijanic DM. Comparative study of the microstructures and mechanical properties of direct laser fabricated and arc-melted AlxCoCrFeNi high entropy alloys. *Mater Sci Eng A* 2015;633:184–93.
- Chen W, Fu Z, Fang S, Xiao H, Zhu D. Alloying behavior, microstructure and mechanical properties in a FeNiCrCo<sub>3</sub>Al<sub>10</sub>7 high entropy alloy. *Mater Des* 2013;51:854–60.
- Fu Z, Chen W, Wen H, Chen Z, Lavernia EJ. Effects of Co and sintering method on microstructure and mechanical behavior of a high-entropy Al<sub>0.6</sub>NiFeCrCo alloy prepared by powder metallurgy. *J Alloys Compd* 2015;646:175–82.

- [45] Wang R, Zhang K, Davies C, Wu X. Evolution of microstructure, mechanical and corrosion properties of AlCoCrFeNi high-entropy alloy prepared by direct laser fabrication. *J Alloys Compd* 2017;694:971–81.
- [46] Chen S, Tang Y, Liaw PK. Additive Manufacturing of High-entropy alloys: A review. *Entropy* 2018;20:937.
- [47] Haj Ibrahim S, Skibinski J, Oliver GJ, Wejrzanowski T. Microstructure effect on the permeability of the tape-cast open-porous materials. *Mater Des* 2019;167:1–7.
- [48] Prashanth KG, Scudino S, Maity T, Das J, Eckert J. Is energy density a reliable parameter for materials synthesis by selective laser melting?. *Mater Res Lett* 2017;5:386–90.
- [49] Karlsson D, Marshal A, Johansson F, Schuisky M, Sahlberg M, Schneider JM, et al. Elemental segregation in an AlCoCrFeNi high-entropy alloy – A comparison between selective laser melting and induction melting. *J Alloys Compd* 2019;784:195–203.
- [50] Niu PD, Li RD, Yuan TC, Zhu SY, Chen C, Wang MB, Huang L. Microstructures and properties of an equimolar AlCoCrFeNi high entropy alloy printed by selective laser melting. *Intermetallics* 2019;104:24–32.
- [51] Shiratori H, Fujieda T, Yamanaka K, Koizumi Y, Kuwabara K, Kato T, et al. Relationship between the microstructure and mechanical properties of an equiatomic AlCoCrFeNi high-entropy alloy fabricated by selective electron beam melting. *Mater Sci Eng A* 2016;656:39–46.



**Paper II**

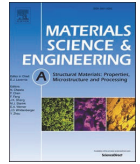
**Karimi, J.,** Suryanarayana, C., Okulov, I., & Prashanth, K. G. (2021). Selective laser melting of Ti6Al4V: Effect of laser re-melting. *Materials Science and Engineering: A*, 802, 140558.





Contents lists available at ScienceDirect

## Materials Science &amp; Engineering A

journal homepage: <http://www.elsevier.com/locate/msea>

## Selective laser melting of Ti6Al4V: Effect of laser re-melting

J. Karimi<sup>a</sup>, C. Suryanarayana<sup>b</sup>, I. Okulov<sup>c,d</sup>, K.G. Prashanth<sup>a,e,f,\*</sup><sup>a</sup> Department of Mechanical and Industrial Engineering, Tallinn University of Technology, Tallinn, Estonia<sup>b</sup> Department of Mechanical and Aerospace Engineering, University of Central Florida, Orlando, FL, 32816-2450, USA<sup>c</sup> Ural Federal University, Institute of Natural Sciences and Mathematics, 620002, Yekaterinburg, Russia<sup>d</sup> Leibniz Institute for Materials Engineering - IWT, Badgasteiner Str. 3, Bremen, 28359, Germany<sup>e</sup> Erich Schmid Institute of Materials Science, Austrian Academy of Sciences, Leoben, Austria<sup>f</sup> CBCMT, School of Mechanical Engineering, Vellore Institute of Technology, Vellore, Tamil Nadu, India

## ARTICLE INFO

## Keywords:

Additive manufacturing  
Selective laser melting  
Laser remelting  
Microstructure  
Ti6Al4V

## ABSTRACT

Microstructural inhomogeneity in additively manufactured materials affects the material properties. The present study aims in minimizing such microstructural inhomogeneity in Ti6Al4V alloy fabricated using selective laser melting (SLM) from the gas atomized powder. A detailed and systematic study of the effect of remelting on the microstructure and mechanical properties of Ti6Al4V was undertaken. Acicular  $\alpha'$  martensite was present in all the samples (both in the as-built SLM and remelted) and the dimensions of the  $\alpha'$  phase change with the number of melting steps. The hardness of the as-built SLM sample increased and the material got homogenized with an increasing number of meltings. The ultimate tensile strength was higher in the double- and triple-melted samples while the ductility was lower than the single-melted sample. The present results clearly prove that the number of remeltings play a significant role in determining the microstructure (homogenization of the microstructure) and the mechanical properties of the SLM-built materials.

## 1. Introduction

Recently, Additive Manufacturing (AM) has experienced significant growth and is becoming the manufacturing technology of the future [1–3]. AM techniques like the laser-based powder bed fusion process (LPBF)/selective laser melting (SLM) can fabricate near-net-shaped components with added functionality and of any shape [4,5]. SLM can fabricate a wide spectrum of materials such as Al-based [6–8], Co-based [9], Ni-based [10], Fe-based [11,12], Cu-based [13,14], Cr-based [15], Ti-based alloys [16], and other classes of materials like high entropy alloys [17] and quasicrystalline materials [18]. In addition, the SLM process has the capability of fixing the process parameters easily for the new generation alloys, which are rather difficult to fabricate using other AM processes [19].

Ti6Al4V alloys are commonly used in several industries because of their high specific strength, desirable tribological properties, and excellent corrosion resistance [20,21]. Further, LPBF/SLM with a flexible layer-by-layer control strategy is attracting the attention of materials scientists in the manufacturing of Ti-based alloys. The as-built SLM Ti6Al4V alloy consists of acicular  $\alpha'$  martensite due to the rapid cooling rates obtained during the SLM process [22–24], resulting in high tensile

strength but poor ductility [25]. Yang et al. [26] reported the effects of SLM process parameters including laser scan speed and hatch spacing on the martensitic size, as well as the formation mechanisms. Yang et al. [26] varied the laser scan speed (between 600 and 1100 mm/sec) and the hatch spacing (70–120  $\mu\text{m}$ ) and kept the laser power constant at 194 W to manufacture the Ti6Al4V samples. They have observed that the size of the martensitic phase could be controlled by the SLM process parameters (changing laser scan speed and hatch distance). Moreover, they have observed the hierarchical microstructure of acicular  $\alpha'$  martensite (four different types of  $\alpha'$  martensite based on their size scales) due to the peculiar thermal cycles observed during the SLM process. The results indirectly show that the martensite sizes may be controlled by controlling the thermal cycles. However, there was very little information on the effects of martensitic size on the microstructure and the resultant mechanical properties.

The laser melting sequence is a novel melting strategy that may be effectively employed during the SLM process to avail further benefits of the technology. During the laser melting sequence, the same layer may be melted several times with the same or different process parameters between two layers. It may also be possible that the first sequence is used to heat (partially sinter) the powder bed and the second sequence is used

\* Corresponding author. Department of Mechanical and Industrial Engineering, Tallinn University of Technology, Tallinn, Estonia.  
E-mail address: [kgrashanth@gmail.com](mailto:kgrashanth@gmail.com) (K.G. Prashanth).

<https://doi.org/10.1016/j.msea.2020.140558>

Received 17 July 2020; Received in revised form 12 November 2020; Accepted 15 November 2020

Available online 19 November 2020

0921-5093/© 2020 Elsevier B.V. All rights reserved.



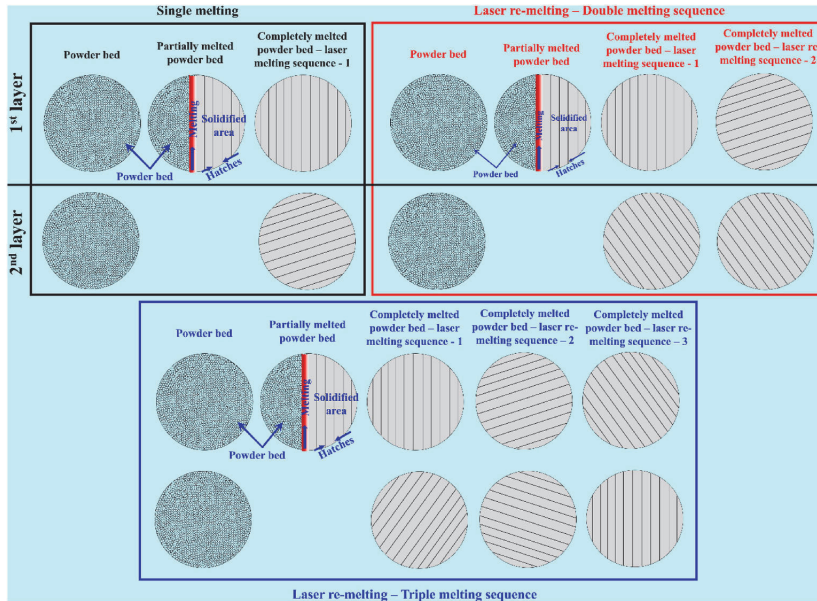


Fig. 1. Schematics illustrating the three melting sequences used in the present study.

to melt the powder bed and vice-versa. In the present study, three different melting sequences have been utilized as shown in Fig. 1. In this manuscript, three different melting sequences were utilized, namely: (1) Single melting, where the laser scans the powder bed once and it melts the powder bed selectively. After solidification of the melt pool, the next layer of powder is deposited and the process iterates until the finish of the component.

(2) Double melting, where the laser scans the powder bed selectively to melt the powder, and the solidified surface is scanned again by the laser with the same process parameters (excepting 72° rotated hatch style) again to re-melt the solidified part. Up-on re-solidification of the powder bed, the second layer of the powder will be deposited and the process iterates until the part is complete. (3) Triple melting, where the laser scans the powder bed once to melt the powders selectively. The solidified layer is again scanned by the laser (with the same process parameters, expecting 72° hatch style rotation), which melts the solidified layer again. Hence, re-solidification takes place. Finally, the re-solidified laser is scanned by the laser (with the same process parameters, excepting 72° hatch style rotation), which again melts the re-solidified layer. Hence, the solidification takes place at the designed parts for the third time without the addition of powder. After the same

position is solidified the third time, the next layer of powder will be deposited. Since the same layer is melted and solidified three times, the heat extraction (usually through the substrate plate) will have an influence along with the energy absorption at the same surface, which may alter the solidification conditions and in turn the cooling rate.

Several studies [27–29] have reported the application of laser melting sequence in an SLM process, which was primarily employed to reduce residual stress, increase density, modify the microstructure, and surface finish of the SLM produced parts. Vaithilingam et al. [27] employed surface remelting/skin scanning during SLM to improve the surface quality of the components. In addition, they have also observed that surface remelting not only helps in improving the surface quality of the parts, but it also influences its surface chemistry (which is altered) along with the surface oxide layer. Shiomi et al. [28] while trying to reduce the residual stresses within the SLM produced parts, attempted laser re-scanning on the following powder mixture: Standard chrome-molybdenum steel + Nickel + Copper Phosphate. The laser re-scanning was performed with varying energy density and it has been observed that with an increase in the energy density to 150% for re-scanning (12.4 J/mm<sup>2</sup> – energy per unit area), the residual stress is reduced to about 55% with the re-scanned layer.

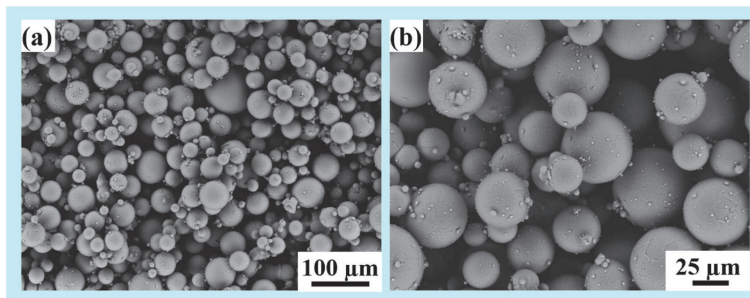


Fig. 2. Scanning electron microscopy images of the gas atomized Ti6Al4V powder used for the SLM fabrication process.

**Table 1**

The process parameters used to fabricate the Ti6Al4V samples using the selective laser melting process.

Laser	120 W Yb-YAG laser
Laser spot size	39 $\mu\text{m}$
Hatch distance	60 $\mu\text{m}$
Hatch rotation angle	73°
Laser scan speed	1 m/s
Layer thickness	25 $\mu\text{m}$
Laser power	60 W

Ali et al. [29] have reported the effect of melting sequence (re-scanning) by varying the scanning strategy and energy density in the SLM Ti6Al4V parts. In spite of the variations in the melting sequence, the SLM Ti6Al4V samples show an acicular  $\alpha'$  martensite due to rapid solidification conditions. Accordingly, the density and hardness vary with the melting sequence (varying power). It has been demonstrated that the re-scanning (with 150% energy density) can reduce the residual stresses up to 33.6%. However, the effect of melting sequence/re-melting on the cooling rate, thermal penetration depth, and consequently the microstructure and properties of SLM Ti6Al4V has not been investigated systematically. Accordingly, the present contribution deals with the effect of re-melting on the microstructure and mechanical behavior of the SLM Ti6Al4V samples. The influence of re-melting scan strategy on the evolution of microstructure (in terms of texture, crystallite size, dislocation density, the lattice parameter of the acicular martensitic phase ( $a$  and  $c$ ), the morphology of the acicular martensitic phase, and porosity level in the microstructure), changes in the absorbed energy density, thermal penetration depth, and in turn the mechanical properties will be evaluated and discussed in detail.

## 2. Experimental methods

Ti6Al4V gas atomized powder from Realizer GmbH was used in the present study. The morphology of the powder particles was furnished in Fig. 2, which shows that the powder particles are spherical in shape. However, several satellites are attached to the powder particles. The average diameter of the powder particles is observed to be  $21 \pm 5 \mu\text{m}$ . The original composition of the Ti6Al4V powders was found to be: Al – 6.01 wt%, V – 4.02 wt%, Si < 0.1 wt%, C < 0.08 wt%, N < 0.03 wt%, other – 0.10 wt%, Ti – rest.

The Ti6Al4V bulk samples were manufactured using a ReaLizer SLM-50. It is equipped with a 120 W Yb-YAG laser (spot size of  $\sim 39 \mu\text{m}$ ). Table 1 lists the experimental parameters. Each layer is melted either once or twice or thrice to study the influence of laser re-scanning. In the single melting sequence, the powder bed is melted once with the process parameters given in Table 1. During double melting, the same layer is melted twice. After the first melting and solidification sequence, the second melting and solidification sequence was carried out without the addition of powder. The process parameter was kept the same excepting

a hatch style rotation of 72° between the first and second melting cycles unlike in the published reports [30,31]. Hence, a total of 144° hatch rotation was observed between single and double melted samples. During triple melting, the following melting sequence was carried out: (1) initial melting of the powder bed and solidification. (2) Re-melting of the solidified layer and re-solidification with the same set of process parameters excepting a hatch style rotation of 72° and without the introduction of the powder and (3) re-melting of the re-solidified layer and again solidification with the same set of process parameters excepting a hatch style rotation of 72°. Accordingly, a hatch style rotation of 288° is observed between single and triple melted samples. The laser re-melting sequence is also illustrated in detail in Fig. 1.

The possible oxygen contamination in the SLM parts was avoided using a constant flow of high purity argon gas. The specimens were fabricated on a 20 mm thick Ti6Al4V platform. Tensile samples with the dimensions shown in Fig. 3 (according to ASTM standard: ASTM E8/E8M – 13a, where the dimensions are modified to suit the length of 52 mm as per the ratio mentioned in the standard) were prepared for the experiments. The microstructure and the properties obtained from the single melted sample, which corresponds to the as-melted condition and it is taken as a reference to compare with double and triple melted samples.

Standard metallographic practices were used for the mounting and polishing of the samples. Kroll's reagent consisting of 5 ml of  $\text{HNO}_3$ , 3 ml of HF, and 100 ml of distilled water was used as an etchant. The microstructural characterization was carried out using a Zeiss FEG scanning electron microscope fitted with an energy dispersive X-ray (EDX). The structural analysis of the alloys was performed using X-ray diffractometer Brucker-axis D5005 in reflection mode with a step size of 0.01. The Scherer equation was used to determine the crystallite size [32], using the equation:

$$D = \frac{K\lambda}{\beta \cos\theta} \quad (1)$$

where  $D$  is the crystallite size,  $\lambda$  is the wavelength of the X-ray beam (i.e.  $\lambda_{\text{Cu-K}\alpha} = 1.5406 \text{ \AA}$ ),  $K$  is the shape factor,  $\beta$  is the full width at half maximum of the diffraction peak and  $\theta$  is the Bragg angle. Lattice parameters were calculated using Bragg's law [33] along with the plane spacing equation, respectively, as follows:

$$\lambda = 2d \sin \theta \quad (2)$$

$$\frac{1}{d^2} = \frac{4}{3} \left( \frac{h^2 + hk + k^2}{a^2} \right) + \frac{l^2}{c^2} \quad (3)$$

where  $d$  is interplanar spacing,  $a$  and  $c$  are the lattice constants, and  $h$ ,  $k$ , and  $l$  are the Miller indices. The dislocation density,  $\rho$ , was estimated by the Williamson-Hall approach [34], using the equation:

$$\rho = 14.4 \frac{\epsilon^2}{b^2} \quad (4)$$

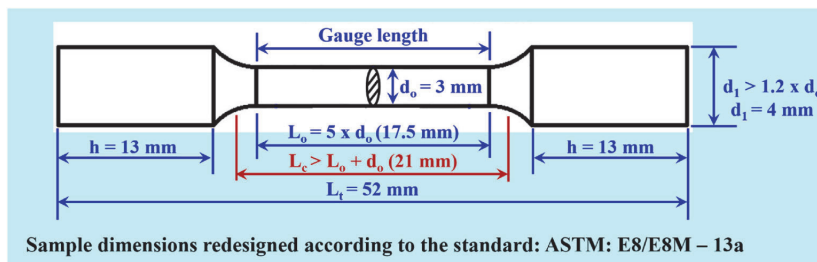


Fig. 3. A schematic sketch of the tensile samples fabricated for testing with the dimensions modified to have a length of 52 mm as per the ratio from the standard ASTM: E8/E8M – 13a.

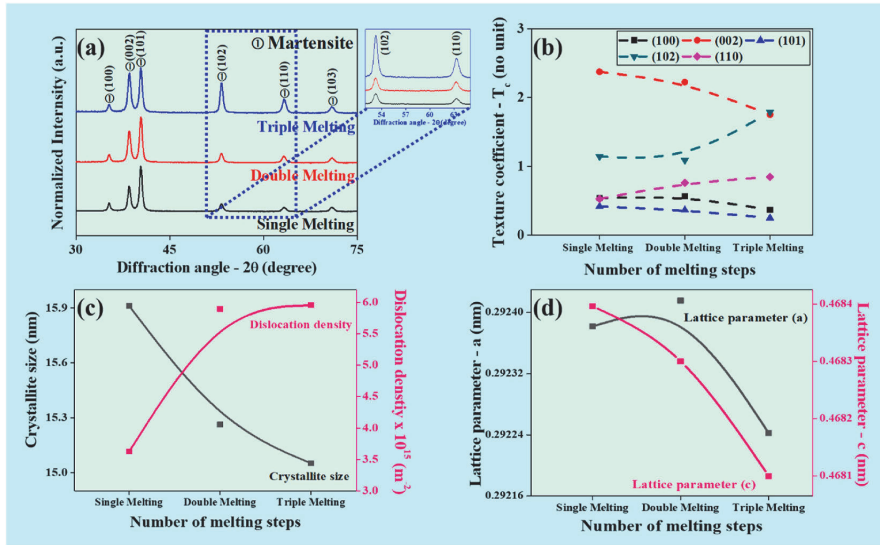


Fig. 4. (a) X-ray diffraction patterns for the SLM processed Ti6Al4V samples as a function of the number of melting steps, (b) texture coefficient of the SLM Ti6Al4V samples calculated from the X-ray diffraction data, (c) crystallite size and the dislocation density of the SLM Ti6Al4V samples, and (d) the corresponding lattice parameters *a* and *c*.

where *ε* is the lattice strain and *b* is the magnitude of the Burgers vector. The lattice strain, *ε*, is obtained using the relationship [35,36]:

$$\beta \frac{\cos \theta}{\lambda} = \frac{0.9}{D} + 2\epsilon \frac{\sin \theta}{\lambda} \tag{5}$$

By plotting  $\beta \cos \theta$  against  $\sin \theta$ , a straight line is obtained, the slope of which gives the lattice strain, *ε*.

The density of the samples was measured using the Archimedes method. In addition, the distribution and size of the voids were

measured using the Image J software using contrast difference measurements. The dimensions of the acicular  $\alpha'$  martensite platelets were measured using Image J software. Around 50 readings for each dimension were measured from several optical/scanning electron microscopy images and only the average values are reported. The hardness test was carried out over 10 rows with 10 indents in each row using a Vickers INDENTEC 5030SKV machine with 5 kgf load and 10 s dwell time. Room temperature tensile tests were performed on a servo-hydraulic Instron 8516 machine with a strain rate of 0.001 mm/s. At least three samples

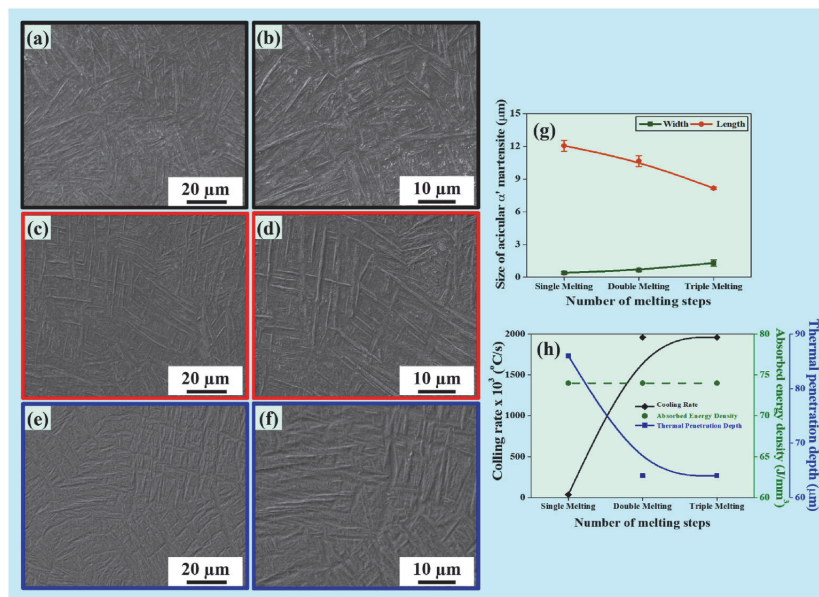


Fig. 5. Scanning electron microscopy images of the SLM Ti6Al4V specimens as a function of the number of melting steps: (a, b) single melting, (c, d) double melting, and (e, f) triple melting; (g) length and width of the acicular  $\alpha'$  martensite phase for a different number of melting steps calculated from the scanning electron microscopy images, and (h) cooling rate, absorbed effective energy density ( $\delta_{th}$ ), and thermal penetration depth ( $\delta_{th}$ ) observed during the SLM process as a function of the melting sequence.

**Table 2**  
Chemical composition of the SLM Ti6Al4V samples fabrication samples measured using the energy dispersive X-ray (EDX).

Melting Sequence	Concentration of the elements (wt.%)			
	Ti	Al	V	Fe
Single Melting	89.72 ± 0.41	5.98 ± 0.06	3.99 ± 0.06	0.31 ± 0.03
Double Melting	89.62 ± 0.33	6.05 ± 0.11	4.05 ± 0.05	0.11 ± 0.10
Triple Melting	89.78 ± 0.36	5.91 ± 0.05	4.02 ± 0.07	0.29 ± 0.04

were tested in each condition (single, double, and triple melting) to evaluate the reproducibility of the results and the representative tensile curves are presented where necessary.

### 3. Results

Fig. 4(a) presents the XRD patterns of the SLM Ti6Al4V samples with different numbers of melting steps. The patterns show the presence of the  $\alpha'$  martensite phase, similar to other earlier reports [26,37]. It may be observed that the intensity of the (002), (102), and (110) peaks of the triple-melted sample are stronger compared to the single-melted sample suggesting texture (preferred orientation) in the material.

The texture in the SLM samples can be modified by changing the scanning strategy [38], cooling rate [39,40], or by building the samples with certain angles to the base plate [41]. The extent of texture in the (100), (002), (101), (102), and (110) planes was quantified (Fig. 4(b)) using the following formula [42]:

$$T_c(hkl) = \frac{I(hkl)/I_0(hkl)}{(1/N) \left[ \sum_N I(hkl)/I_0(hkl) \right]} \quad (6)$$

where  $T_c$  is the texture coefficient of the  $(hkl)$  plane,  $I_0$  is the standard intensity from the reference (JCPDS data [43]),  $I$  is the measured intensity, and  $N$  is the number of diffraction peaks. If the texture coefficient is  $0 < T_c(hkl) < 1$ , it indicates a lack of texture (preferred orientation) in the given planes; this is true for the planes including (110), (100), and (101). The higher value of  $T_c$  (for example  $>1$  for the (002) plane) means that the samples show a higher degree of preferred orientation. With an increasing number of melting steps, the  $T_c(hkl)$  of the (110) plane tends to approach unity, while  $T_c(hkl)$  of the (002) plane decreases, and the (102) plane shows a strong crystallographic texture. The effects of the number of melting steps on the structural data including crystallite size and the dislocation density were evaluated (Fig. 4(c)).

The number of melting steps influences the crystallite size; the crystallite size decreases with an increasing number of melting steps, evaluated from the peak broadening of the (102) and (110) planes, as shown in the magnified view of Fig. 4(a). A dislocation density in the order of  $6 \pm 2 \times 10^{15} \text{ m}^{-2}$  was calculated for the triple-melted sample, which is higher than in the single-melted sample ( $3.5 \pm 1 \times 10^{15} \text{ m}^{-2}$ ). The dislocation densities in these SLM processed samples were significantly (two orders of magnitude) higher than the conventional Ti-6Al-4V alloy, as reported by Babu et al. [44]. Also, Hayes et al. [45] reported a dislocation density of  $\sim 10^{15} \text{ m}^{-2}$  for Ti-6Al-4V produced by using directed energy deposition, another AM process, which is similar to the value in the present samples. Furthermore, the lattice parameters  $a$  and  $c$  decrease with an increasing number of melting steps (Fig. 4(d)), and the values for single-melted samples are similar to the results of Thijs et al. [23]. Fig. 5(a–f) shows the SEM images of the Ti6Al4V SLM samples with an increasing number of melting steps from single to double to triple melting. The microstructure in general consists of the acicular  $\alpha'$  martensite phase (observed from XRD patterns). Even though the acicular  $\alpha'$  martensite phase shows the plate morphology, the size of the acicular  $\alpha'$  martensite changes with the number of melting steps. Accordingly, the dimensions (length and width) of the  $\alpha'$  acicular martensite were measured and summarized in Fig. 5(g). The width of the

**Table 3**  
Change in the penetration depth as a function of laser power.

Laser power	Bed condition	Average penetration depth ( $\mu\text{m}$ )	Reference
P50 – 50 W	Powder	45.0	Bayat et al. [56]
P80 – 80 W	Powder	66.2	Bayat et al. [56]
P110 – 110 W	Powder	101.0	Bayat et al. [56]
60 W	Powder	86.0	Present study
60 W	Bulk	64.0	Present study

acicular  $\alpha'$  martensite increased ( $0.40 \pm 0.05 \mu\text{m}$ ,  $0.65 \pm 0.05 \mu\text{m}$ , and  $1.31 \pm 0.12 \mu\text{m}$ ) and the length decreased ( $12 \pm 6 \mu\text{m}$ ,  $10 \pm 4 \mu\text{m}$ , and  $8 \pm 4 \mu\text{m}$ ) with an increasing number of melting steps from single to triple melting. The chemical composition of the single, double, and triple melted samples measured using the EDX point scan were tabulated in Table 2. It can be observed from Table 2 that the chemical composition of the samples does not vary with an increase in the remelting (see Table 3).

During the SLM process, when the laser beam is projected onto the powder bed or the bulk sample, the laser energy will be either absorbed or reflected. Although the reflectivity of the metal is vital when quantifying the input energy, it drops significantly within microseconds as the melting begins [46]. On the other hand, absorptivity (the ratio of the absorbed laser radiation to the incident laser radiation [47]) of Ti6Al4V powder (at room temperature) at  $\sim 1 \mu\text{m}$  laser wavelength is  $\sim 77\%$  [48]. The absorbed effective energy density  $E_{d\text{-eff}}$  is defined with the following formulas, given by Ref. [2]:

$$E_d = \left( \frac{P}{vht} \right) \quad (7)$$

$$E_{d\text{-eff}} = \alpha E_d \quad (8)$$

where  $E_d$  is the energy density in  $\text{J}/\text{mm}^3$ ,  $P$  is the power expressed in W,  $v$  is the laser scanning speed in  $\text{mm}/\text{s}$ ,  $h$  is hatch spacing in mm,  $t$  is the layer thickness in mm,  $E_{d\text{-eff}}$  is absorbed effective energy density in  $\text{J}/\text{mm}^3$ , and  $\alpha$  is the energy absorption coefficient.

The thermal conductivity, which depends on the coordination number (of powder particles), density, and temperature [49], affects the cooling rate of the considered medium [50]. In comparison with the bulk sample, the powder bed shows decreased thermal conductivity due to the presence of voids between the powder particles [49]. The thermal conductivity at room temperature of Ti6Al4V powder (particle size of 20–63  $\mu\text{m}$ ) and the bulk sample is 0.13  $\text{W}/\text{K}\cdot\text{m}$  [51] and 7.1  $\text{W}/\text{K}\cdot\text{m}$  [52], respectively. Rosenthal [53] used some assumptions (a point heat source is used with constant thermal properties, no heat losses, and no convection in the pool) to derive analytical equations for the heat flow, which is as follows:

$$\frac{2\pi(T - T_0)kR}{Q} = \exp \left[ \frac{-V(R - x)}{2A} \right] \quad (9)$$

where  $T$  ( $^\circ\text{C}$ ) is the temperature of the melt pool,  $T_0$  ( $^\circ\text{C}$ ) is the temperature before laser exposure,  $k$  is the thermal conductivity in  $\text{W}/\text{K}\cdot\text{m}$ ,  $Q$  is the heat transferred from the heat source and is expressed in W,  $V$  is the scan speed expressed in  $\text{m}/\text{s}$ ,  $A$  is the thermal diffusivity in  $\text{m}^2/\text{s}$ , and  $R$  is the radial distance in m:  $R = \text{SQRT}(x^2 + y^2 + z^2)$ , where  $x$ ,  $y$ , and  $z$  are the coordinates along the X, Y, and Z-axes respectively. Due to the increase in the thermal conductivity of the bulk samples as compared to the powder bed, the cooling rate in the bulk counterpart is higher and increases with an increasing number of melting steps (Fig. 5(h)). This increasing trend in the cooling rate with an increasing number of melting steps is in agreement with the results reported earlier [29], where they reported the cooling rate of the SLM Ti6Al4V sample

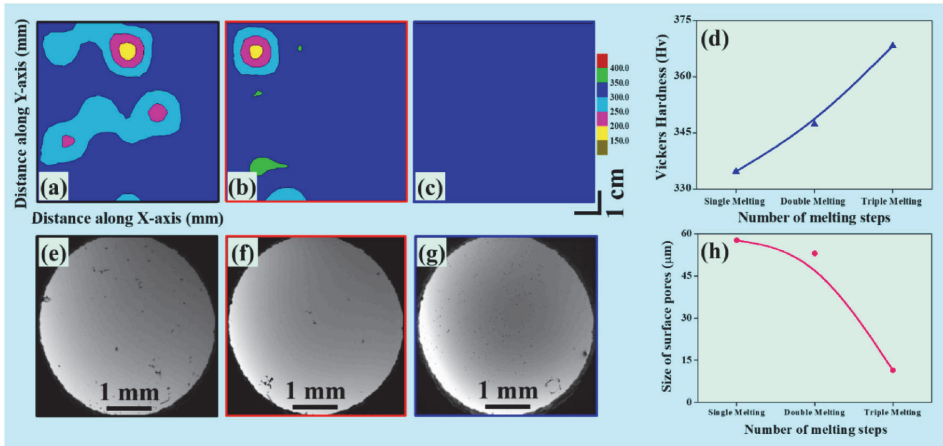


Fig. 6. Hardness distribution maps for the SLM Ti6Al4V samples fabricated as a function of the number of melting steps: (a) single, (b) double, and (c) triple melting; (d) Vickers hardness plot for the SLM Ti6Al4V sample produced with single, double and triple melting; Surface porosity of samples as a function of the melting sequence: (e) single, (f) double, and (g) triple melting; (h) plot showing the average size of surface pores as a function of the number of melting steps.

produced with single melting and double melting as  $7.8 \times 10^5$  and  $13.8 \times 10^5$  °C/s, respectively. A maximum melt pool temperature of ~2300 °C was observed with 1 m/s laser scan speed, and as the laser beam moved away, the temperature of the melt pool decreased to room temperature in milliseconds [1]. Irrespective of the number of the melting steps, Ti6Al4V alloys show a fully acicular  $\alpha'$  martensite phase, since the cooling rate is higher than 410 °C/s [54].

The thermal penetration depth which is an approximation for the heat distribution in a considered medium depends on thermal diffusivity and conductivity, exposure time, etc. and (in a semi-infinite material) is defined as [55]:

$$\delta_{th} = 2\sqrt{A\Delta t} \tag{10}$$

where  $\Delta t$  is the laser exposure time in s and  $A$  is the thermal diffusivity in  $m^2/s$  of the considered medium. The thermal penetration depth (Fig. 5 (h)) for the powder and bulk samples were observed to be ~86  $\mu m$  and ~64  $\mu m$ , respectively, where the powders with particle size ranging between 20 and 63  $\mu m$  exhibited an apparent density of ~57%. Bayat et al. [56] reported similar penetration depths for Ti6Al4V SLM samples when fabricated with similar laser power.

Hardness mapping, which is a tool to quantify heterogeneity of the fabricated parts and to understand the material behavior [57], was used to reveal the variation in hardness across the sample surface (Fig. 6 (a-c)). It may be observed from the hardness distribution maps (Fig. 6 (a-c)) that the SLM Ti6Al4V samples became more uniform and showed homogeneous distribution of hardness with an increasing number of melting steps. In fact, the sample was completely homogeneous when the sample was melted thrice. On the other hand, in single- and double-melted samples, some degree of non-uniformity was still observed in terms of hardness distribution. In addition, the average Vickers hardness values increased from  $334 \pm 10$  H<sub>v</sub> for the as-built single melted SLM sample to  $347 \pm 7$  H<sub>v</sub> for the sample with double melting, and it finally reached  $368 \pm 12$  H<sub>v</sub> for the triple-melted sample (Fig. 6(d)). The change in the number of melting steps effectively altered the microstructure of the SLM Ti6Al4V samples in terms of the acicular  $\alpha'$  martensite dimensions (Fig. 5), which subsequently led to the differences in the hardness and their distribution (Fig. 6(a-c)).

The theoretical density of these samples is found to be  $98.0 \pm 0.5\%$ ,  $98.8 \pm 0.3\%$ , and  $99.5 \pm 0.2\%$  for single, double, triple melted samples respectively. In a rapid solidification process like what happens in the SLM process, where sufficient time is not available for conductive

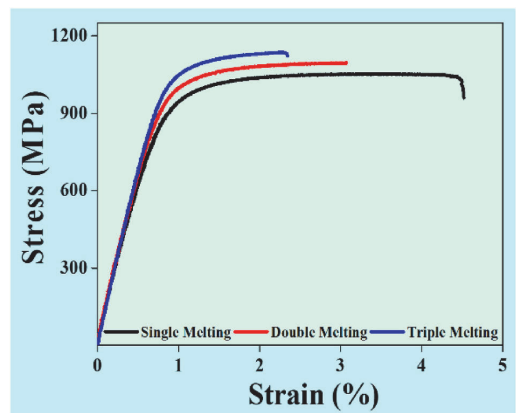


Fig. 7. Room-temperature tensile stress-strain curves for the SLM Ti6Al4V samples as a function of laser remelting sequence.

homogenization of the input energy and subsequently the heat distribution in the powder bed, pore formation occurs due to lack of fusion. The pores that form during the SLM process may be categorized into two: (1) lack of fusion pores (irregularly shaped) that form due to improper SLM process parameters and (2) metallurgical pores (spherical in shape), which form due to the presence of adsorbed/entrapped gases. Moreover, metallurgical pores appear in parts fabricated by SLM [58]. The morphology of surface pores in SLM Ti6Al4V samples with an

Table 4  
Room temperature tensile properties of the Ti6Al4V SLM samples as a function of the number of melting steps.

	Melting number		
	Single	Double	Triple
$\sigma_{0.2\%}$ (MPa)	$930 \pm 0.2$	$985 \pm 8$	$1027 \pm 5$
$\sigma_u$ (MPa)	$1055 \pm 3$	$1104 \pm 12$	$1135 \pm 3$
Elongation (%)	$4.3 \pm 0.5$	$3 \pm 0.1$	$2 \pm 0.1$
E (GPa)	$120 \pm 1$	$128 \pm 0.9$	$134 \pm 5$

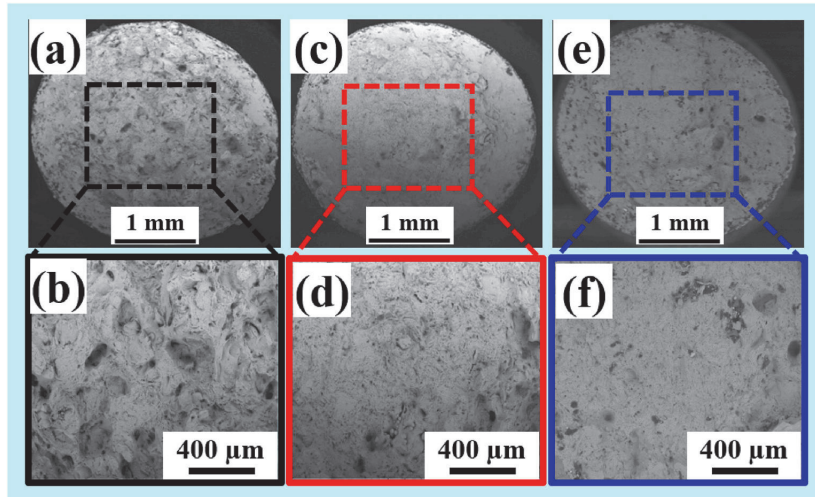


Fig. 8. Scanning electron microscopy images showing the fracture surface for the SLM samples as a function of the number of melting steps: Single melting: (a) low magnification and (b) high magnification images, double melting (c) low magnification and (d) high magnification images, and triple melting (e) low magnification and (f) high magnification images.

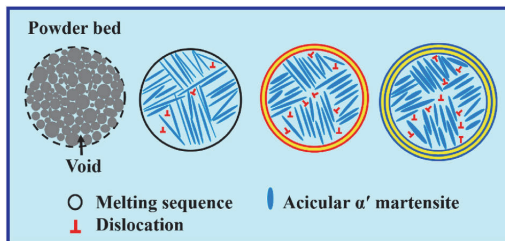


Fig. 9. Schematic illustration of the powder bed and the effect of the number of melting steps on the microstructure of the Ti6Al4V alloy.

increasing number of melting steps is illustrated in Fig. 6(e–g). With an increasing number of melting steps, fusion pores may be eliminated, but metallurgical (spherical) pores are still observed (Fig. 6(g)). However, the size of these pores is reduced significantly with an increasing number of melting steps from single to triple melting (Fig. 6(h)).

The room-temperature tensile stress-strain curves for the SLM Ti6Al4V samples as a function of the number of melting steps are shown in Fig. 7 and the mechanical properties are listed in Table 4. The ultimate tensile strength of the samples increased from single to triple melting, mainly due to the presence of the acicular  $\alpha'$  martensite microstructure. These values are higher than the tensile values observed for the wrought Ti6Al4V counterpart [59,60]. However, this improvement in the ultimate tensile strength is at the expense of ductility, which decreased with an increasing number of melting steps. Accordingly, the triple-melted sample exhibited the maximum yield ( $\sigma_{0.2\%}$ ) and ultimate tensile strengths ( $\sigma_u$ ) compared to the double- and single-melted samples. But, the ductility was significantly lower in the triple-melted sample, which is inferior to the single- and double-melted samples. Fig. 8(a–f) show the fracture surfaces of the tensile samples. The fracture surface of the single-melted sample (Fig. 8(a)), and its high magnification image (Fig. 8(b)), exhibit the presence of deep dimples, indicating appreciable ductility in the sample. On the other hand, the fracture surface of the double- and triple-melted samples (Fig. 8(c–f)), exhibit shallow and small size dimples, suggesting that the samples are more

brittle than the sample produced by single melting. In addition, the sample fabricated with triple melting shows less porosity (in both number and size) than the single-melted sample.

#### 4. Discussion

The schematic representation showing the effect of single, double, and triple melting on the acicular  $\alpha'$  martensite size is shown in Fig. 9. As illustrated in Fig. 5(d), the width of acicular  $\alpha'$  martensite increased more than three-fold, but its length decreased by  $\sim 30\%$  with increasing the number of melting steps. In addition, the dislocation density increased from  $3.5 \pm 1 \times 10^{15} \text{ m}^{-2}$  for single melting to  $5 \pm 1 \times 10^{15} \text{ m}^{-2}$  and  $6 \pm 2 \times 10^{15} \text{ m}^{-2}$ , respectively, for double- and triple-melted samples, which is a direct consequence of the metastable rapid solidification processing and the anisotropic solidification conditions [61–63]. In the SLM process, the heat is extracted from the melt pool at different rates in different directions. Generally, the melt pool is surrounded by powder on one side, solidified metal on the other side, inert gas on the top, and solid material at the bottom. Hence, heat extraction is maximum from the bottom since it is solid and has a bigger contact area with the melt pool.

Let us neglect the marginal heat extraction during solidification from the two sides and the top of the melt pool and assume that heat extraction is only from the bottom, where the melt pool is in contact with the solid material. We can then propose the following arguments as a function of the number of melting steps. During the single melting process, the temperature of the melt pool decreases by heat extraction through the bottom, and hence, the material underneath the melt pool gets heated up [64]. During the second melting sequence, the area underneath the melt pool, which is already at slightly above the ambient temperature needs to conduct the heat (transfer) from the melt pool and therefore the cooling rate is significantly reduced. This is because the material at a higher temperature than the ambient temperature cannot transfer the heat at the same rate as in ambient conditions and hence is expected to decrease the cooling rate of the process. Hence, as per the discussion, the cooling rate is expected to decrease with increasing melting sequence from single to triple melting.

On the other hand, the XRD and microstructural features show the opposite trend, which is corroborated by mechanical properties. With

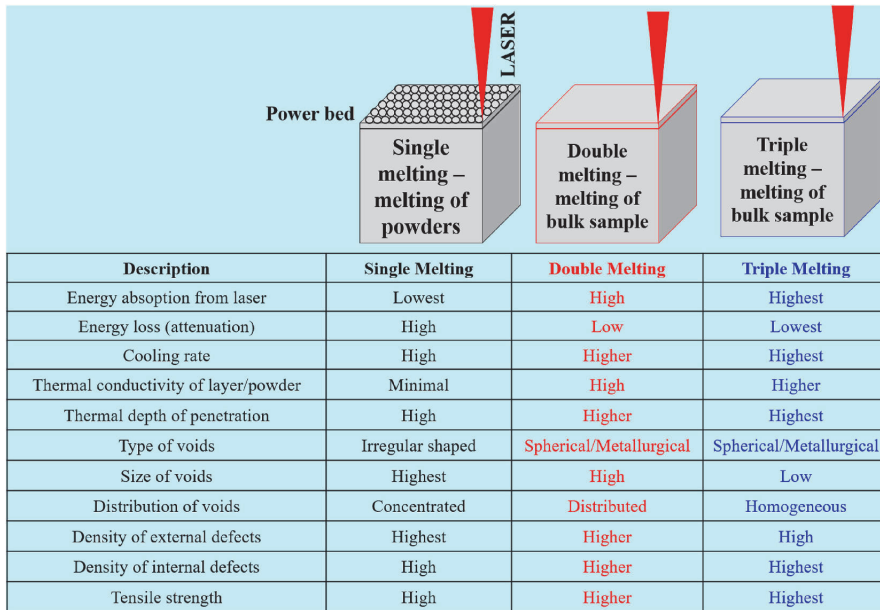


Fig. 10. Schematics illustrating the different effects that takes place during laser re-melting.

increasing the number of melting steps from single to double to triple, the effective energy absorbed in the exposed area increases. For instance, the powder during single melting has maximum voids and hence minimum energy is absorbed from the laser since the voids dissipate the heat (do not absorb the heat). During double melting, the solid area exposed to the laser has minimum voids, compared to the powder bed and hence the energy absorbed will be much higher without much attenuation. Continuing with triple melting, the voids are further reduced after double melting and the solid surface exposed by the laser will have the least voids in it and hence absorbs the maximum energy. With an increase in the absorbed energy, the temperature of the melt pool increases, which finally leads to an increase in the cooling rate of the process. Thus, the effective cooling rate at different stages of melting will be the sum of these two effects (heat dissipation through the bottom and energy absorption rate at the exposed area) discussed above. Effectively, as observed, the cooling rate increased with an increasing number of melting steps.

Similarly, the thermal conductivity of the bulk material (7.1 W/K.m) is more than an order of magnitude higher than the powder particles (0.13 W/K.m), which helps in increasing the thermal penetration depth of the melt pool. The increased thermal penetration depth with an increase in the number of melting events also plays a role in the homogenization of the microstructure. Even though the solidification of the melt pool in an SLM process is considered as the solidification of thin films (neglecting the effect of gravity) [64], the increase in the melt pool size (because of an increase in the thermal penetration depth) will help in the homogenization of the microstructure due to Bernard-Marangoni convection. The deeper the melt pool, the vortex in the melt pool will be severe, which helps in liquid movement causing the homogenization along with the Bernard-Marangoni convection. In addition, the repeated melting of the same layer will lead to successive melting and solidification events at different rates and lead to complete homogenization and uniform distribution of the elements within the melt volume, similar to the arc melting methods, where the material is melted and remelted multiple times to have a homogeneous microstructure. This opens a new direction, where elemental powder mixtures can be employed as raw

materials instead of pre-alloyed powders, which can drastically reduce the material costs involved.

Scanning over a solid (double and triple melted sample), the conductive dissipation of thermal energy away from the melt pool will be faster. Fourier number ( $F_0$ ) is used to obtain a relative measure of heat dissipation rate to heat storage rate during SLM, which can be determined as [65]:

$$F_0 = \left( \frac{At}{L^2} \right) \tag{11}$$

where  $A$ ,  $t$ , and  $L$  refer to thermal diffusivity ( $m^2/s$ ), the characteristic time (s), and the length through which conduction occurs (m), respectively. Higher  $F_0$  signifies a rapid heat dissipation, which helps in faster cooling of the sample since the thermal diffusivity of bulk ( $\sim 3 \times 10^{-6} m^2/s$  [66,67]) is higher than powder ( $\sim 0.5 \times 10^{-6} m^2/s$  [66]). With an increase in the thermal conductivity and conductive dissipation of thermal energy, the cooling rate of the process increases leading to a refined microstructure corroborating with the SEM results (refined martensitic platelets). In this respect, the refinement of the microstructure during SLM is somewhat similar to the microstructural refinement observed during traditional rapid solidification processing of metallic melts. Since the melt cools rapidly, the time allowed for the redistribution of solute atoms in the alloy will be very short and hence the homogeneity of the liquid will be carried down to the solidified material.

The homogeneous hardness maps (hardness uniformity all over the samples) also indirectly confirm that the samples were homogenized with an increasing number of melting steps (Fig. 10). Hence, the present results prove that increasing the melting sequence from single to double to triple melting, refines the microstructure and subsequently improves the mechanical strength. This process will be associated with an increased number of internal defects (like dislocations), essentially due to the residual stresses introduced during solidification, which also contribute to the strength, albeit small in magnitude. On the other hand, the number of external defects (voids/pores) decreases both in size and number with an increasing number of melting steps. With single melting, the large pores are mainly irregular in shape (fusion pores) and

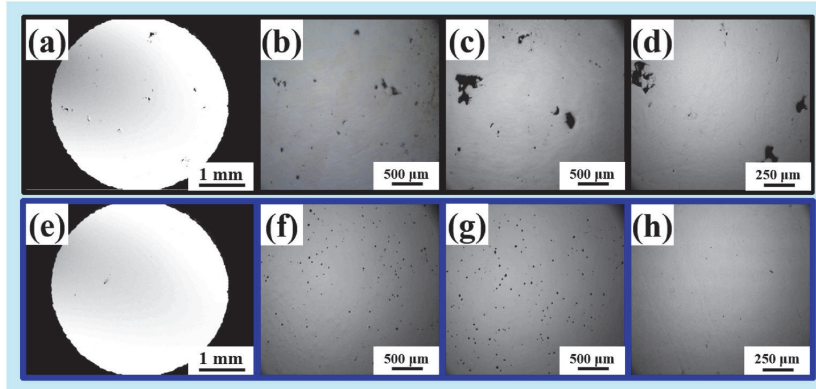


Fig. 11. (a) Scanning electron microscopy and (b–d) optical microscopy images of the single melted Ti6Al4V samples. (e) Scanning electron microscope and (f–h) optical microscopy images of the triple melted Ti6Al4V samples.

with an increasing number of melting steps, spherical shaped pores (metallurgical pores) with significantly reduced size were observed that were characteristic of gas entrapment (Fig. 11). Even though increasing the melting sequence will cost time and money, the present results clearly suggest that it will homogenize the material (in terms of porosity), reduce the number of external defects like porosity, and refine the microstructure thereby improving the mechanical strength of the SLM processed materials.

## 5. Conclusion

In this study, the microstructure and mechanical properties of Ti6Al4V SLM alloys were studied as a function of an increasing number of melting steps. The important observations are as follows:

- Increasing the number of melting steps from single to triple melting resulted in an increase in the cooling rate, which refined the microstructure. The length of the acicular  $\alpha'$  martensite decreased, whereas its width increased marginally resulting in improved mechanical strength at the expense of ductility.
- The number of internal defects in the samples (dislocations) increased with an increasing melting sequence from single to triple melting.
- The single-melted sample showed the presence of fusion pores, whereas by increasing the number of melting steps, they disappeared and only spherical pores existed. Both the size and number of pores decreased with increasing number of melting steps.
- Finally, the sample surface shows a homogeneous distribution of hardness with reduced porosity as the melting sequence is increased from single to triple melting.

The present results suggest that even though the successive re-melting of the same layers increases the time of production and subsequently the cost of processing the parts, the increase in the mechanical strength and homogenization of the samples can compensate for the cost increase. In addition, this opens a new pathway, where elemental powder may be directly used as a raw material instead of pre-alloyed powder. Successive melting of the same layer multiple times may improve homogenizing the powder bed, which will be considered as an economic benefit and a huge relief and breakthrough in the field of additive manufacturing.

## Data availability statement

The data that support the findings of this study are available from the

corresponding author [KGP], upon reasonable request.

## CRediT authorship contribution statement

**J. Karimi:** Formal analysis, Investigation, Data curation, Writing - original draft. **C. Suryanarayana:** Methodology, Writing - review & editing. **I. Okulov:** Methodology, Writing - review & editing. **K.G. Prashanth:** Conceptualization, Methodology, Formal analysis, Investigation, Resources, Data curation, Writing - review & editing, Supervision, Funding acquisition, Project administration.

## Declaration of competing interest

The authors declare that they have no known competing financial interests or personal relationships that could have appeared to influence the work reported in this paper.

## Acknowledgements

The authors would like to thank Mrs. Laivi Väljaots, Messrs. Rainer Traksmaa, Mart Viljus, and Endel Esinurm for technical assistance. Financial assistance through European Regional Development Fund (ASTRA6-6) is greatly acknowledged.

## References

- [1] S. Liu, Y.C. Shin, Additive manufacturing of Ti6Al4V alloy: a review, *Mater. Des.* 164 (2019) 107552, <https://doi.org/10.1016/j.matdes.2018.107552>.
- [2] K.G. Prashanth, S. Scudino, T. Maity, J. Das, J. Eckert, Is the energy density a reliable parameter for materials synthesis by selective laser melting? *Mater. Res. Lett.* 5 (2017) 386–390, <https://doi.org/10.1080/21663831.2017.1299808>.
- [3] K. Prashanth, L. Löber, H.-J. Klauß, U. Kühn, J. Eckert, Characterization of 316L steel cellular dodecahedron structures produced by selective laser melting, *Technologies* 4 (2016) 34, <https://doi.org/10.3390/technologies4040034>.
- [4] F. Li, P. Hao, J. Yi, K.G. Prashanth, T. Maity, J. Eckert, Strengthening effects in nano-/ultrafine-grained carbon nanotube reinforced-titanium composites investigated by finite element modeling, *Metall. Mater. Trans. A Phys. Metall. Mater. Sci.* 49 (2018) 6469–6478, <https://doi.org/10.1007/s11661-018-4945-0>.
- [5] K.G. Prashanth, S. Scudino, A.K. Chaubey, L. Löber, P. Wang, H. Attar, F. P. Schimansky, F. Pyczak, J. Eckert, Processing of Al-12Si-Ti-Ni composites by selective laser melting and evaluation of compressive and wear properties, *J. Mater. Res.* 31 (2016) 55–65, <https://doi.org/10.1557/jmr.2015.326>.
- [6] Y.D. Jia, P. Ma, K.G. Prashanth, G. Wang, J. Yi, S. Scudino, F.Y. Cao, J.F. Sun, J. Eckert, Microstructure and thermal expansion behavior of Al-50Si synthesized by selective laser melting, *J. Alloys Compd.* 699 (2017) 548–553, <https://doi.org/10.1016/j.jallcom.2016.12.429>.
- [7] K.G. Prashanth, R. Ramodaram, S. Scudino, Z. Wang, K. Prasad Rao, J. Eckert, Friction welding of Al-12Si parts produced by selective laser melting, *Mater. Des.* 57 (2014) 632–637, <https://doi.org/10.1016/j.matdes.2014.01.026>.



- [8] Z. Wang, R. Ummethala, N. Singh, S. Tang, C. Suryanarayana, J. Eckert, K. G. Prashanth, Selective laser melting of aluminum and its alloys, *Materials* **13** (2020) 1–67, <https://doi.org/10.3390/ma13204564>.
- [9] B. Qian, K. Saeidi, L. Kvetková, F. Lofaj, C. Xiao, Z. Shen, Defects-tolerant Co-Cr-Mo dental alloys prepared by selective laser melting, *Dent. Mater.* **31** (2015) 1435–1444, <https://doi.org/10.1016/j.dental.2015.09.003>.
- [10] W. Huang, J. Yang, H. Yang, G. Jing, Z. Wang, X. Zeng, Heat treatment of Inconel 718 produced by selective laser melting: microstructure and mechanical properties, *Mater. Sci. Eng. A* **750** (2019) 98–107, <https://doi.org/10.1016/j.msea.2019.02.046>.
- [11] J. Suryawanshi, K.G. Prashanth, U. Ramamurthy, Mechanical behavior of selective laser melted 316L stainless steel, *Mater. Sci. Eng. A* **696** (2017) 113–121, <https://doi.org/10.1016/j.msea.2017.04.058>.
- [12] H.Y. Jung, S.J. Choi, K.G. Prashanth, M. Stoica, S. Scudino, S. Yi, U. Kühn, D. H. Kim, K.B. Kim, J. Eckert, Fabrication of Fe-based bulk metallic glass by selective laser melting: a parameter study, *Mater. Des.* **86** (2015) 703–708, <https://doi.org/10.1016/j.matdes.2015.07.145>.
- [13] S. Scudino, C. Unterdörfer, K.G. Prashanth, H. Attar, N. Ellendt, V. Uhlenwinkel, J. Eckert, Additive manufacturing of Cu-10Sn bronze, *Mater. Lett.* **156** (2015) 202–204, <https://doi.org/10.1016/j.matlet.2015.05.076>.
- [14] S. Zhou, Y. Zhao, X. Wang, W. Li, D. Chen, T.B. Sercombe, Enhanced corrosion resistance of Ti-5 wt.% TiN composite compared to commercial pure Ti produced by selective laser melting in HCl solution, *J. Alloys Compd.* **820** (2020) 153422, <https://doi.org/10.1016/j.jallcom.2019.153422>.
- [15] A. Aramian, Z. Sadeghian, K.G. Prashanth, F. Berto, In situ fabrication of TiC-NiCr cermets by selective laser melting, *Int. J. Refract. Metals Hard Mater.* **87** (2020) 105171, <https://doi.org/10.1016/j.jrmm.2019.105171>.
- [16] N. Singh, P. Hameed, R. Ummethala, G. Manivasagam, K.G. Prashanth, J. Eckert, Selective laser manufacturing of Ti-based alloys and composites: impact of process parameters, application trends, and future prospects, *Mater. Today Adv.* **8** (2020) 100097, <https://doi.org/10.1016/j.mtdadv.2020.100097>.
- [17] J. Karimi, P. Ma, Y.D. Jia, K.G. Prashanth, Linear patterning of high entropy alloy by additive manufacturing, *Manuf. Lett.* **24** (2020) 9–13, <https://doi.org/10.1016/j.mfglet.2020.03.003>.
- [18] K.G. Prashanth, S. Scudino, Quasicrystalline composites by additive manufacturing, *Key Eng. Mater.* **818 KEM** (2019) 72–76, <https://doi.org/10.4028/www.scientific.net/KEM.818.72>.
- [19] P. Konda Gokuldoss, Design of next-generation alloys for additive manufacturing, *Mater. Des. Process. Commun.* **1** (2019) 19–22, <https://doi.org/10.1002/mdp2.50>.
- [20] L.C. Zhang, L.Y. Chen, A review on biomedical titanium alloys: recent progress and prospect, *Adv. Eng. Mater.* **21** (2019) 1–29, <https://doi.org/10.1002/adem.201801215>.
- [21] R. Rahmani, M. Antonov, L. Kollo, Y. Holovenko, K.G. Prashanth, Mechanical behavior of Ti6Al4V scaffolds filled with CaSiO<sub>3</sub> for implant applications, *Appl. Sci.* **9** (2019) 3844, <https://doi.org/10.3390/app9183844>.
- [22] L.E. Murr, S.A. Quinones, S.M. Gaytan, M.I. Lopez, A. Rodela, E.Y. Martinez, D. H. Hernandez, E. Martinez, F. Medina, R.B. Wicker, Microstructure and mechanical behavior of Ti-6Al-4V produced by rapid-layer manufacturing, for biomedical applications, *J. Mech. Behav. Biomed. Mater.* **2** (2009) 20–32, <https://doi.org/10.1016/j.jmbmm.2008.05.004>.
- [23] L. Thijs, F. Verhaeghe, T. Craeghs, J. Van Humbeeck, J.P. Kruth, A study of the microstructural evolution during selective laser melting of Ti-6Al-4V, *Acta Mater.* **58** (2010) 3303–3312, <https://doi.org/10.1016/j.actamat.2010.02.004>.
- [24] L.M. Viespoli, S. Bressan, T. Itoh, N. Hiroyoshi, K.G. Prashanth, F. Berto, Creep and high temperature fatigue performance of as build selective laser melted Ti-based 6Al-4V titanium alloy, *Eng. Fail. Anal.* **111** (2020) 104477, <https://doi.org/10.1016/j.engfailanal.2020.104477>.
- [25] C. Qiu, N.J.E. Adkins, M.M. Attallah, Microstructure and tensile properties of selectively laser-melted and of HIPed laser-melted Ti-6Al-4V, *Mater. Sci. Eng. A* **578** (2013) 230–239, <https://doi.org/10.1016/j.msea.2013.04.099>.
- [26] J. Yang, H. Yu, J. Yin, M. Gao, Z. Wang, X. Zeng, Formation and control of martensite in Ti-6Al-4V alloy produced by selective laser melting, *Mater. Des.* **108** (2016) 308–318, <https://doi.org/10.1016/j.matdes.2016.06.117>.
- [27] J. Vaithilingam, R.D. Goodridge, R.J.M. Hague, S.D.R. Christie, S. Edmondson, The effect of laser remelting on the surface chemistry of Ti6Al4V components fabricated by selective laser melting, *J. Mater. Process. Technol.* **232** (2016) 1–8, <https://doi.org/10.1016/j.jmatprotec.2016.01.022>.
- [28] M. Shiomoto, K. Osakada, K. Nakamura, T. Yamashita, F. Abe, Residual stress within metallic model made by selective laser melting process, *CRP Ann. - Manuf. Technol.* **53** (2004) 195–198, [https://doi.org/10.1016/S0007-8506\(07\)60677-5](https://doi.org/10.1016/S0007-8506(07)60677-5).
- [29] H. Ali, H. Ghadbeigi, K. Mumtaz, Effect of scanning strategies on residual stress and mechanical properties of Selective Laser Melted Ti6Al4V, *Mater. Sci. Eng. A* **712** (2018) 175–187, <https://doi.org/10.1016/j.msea.2017.11.103>.
- [30] J. Guan, Y. Jiang, X. Zhang, X. Chong, Microstructural evolution and EBSD analysis of AlSi10Mg alloy fabricated by selective laser remelting, *Mater. Char.* **161** (2020) 110079, <https://doi.org/10.1016/j.matchar.2019.110079>.
- [31] W. Yu, S.L. Sing, C.K. Chua, X. Tian, Influence of re-melting on surface roughness and porosity of AlSi10Mg parts fabricated by selective laser melting, *J. Alloys Compd.* **792** (2019) 574–581, <https://doi.org/10.1016/j.jallcom.2019.04.017>.
- [32] C. Suryanarayana, M.G. Norton, C. Suryanarayana, M.G. Norton, X-rays and Diffraction, Springer US, New York, 1998, <https://doi.org/10.1007/978-1-4899-0148-4>.
- [33] G.E.M. Janccy, The scattering of X-rays and bragg's law, *Proc. Natl. Acad. Sci. Unit. States Am.* **10** (1924) 57–60, <https://doi.org/10.1073/pnas.10.2.57>.
- [34] V. Mote, Y. Purushotham, B. Dole, Williamson-Hall analysis in estimation of lattice strain in nanometer-sized ZnO particles, *J. Theor. Appl. Phys.* **6** (2012) 1, <https://doi.org/10.1186/2251-7235-6-6>.
- [35] K. Venkateswarlu, M. Sandhyarani, T.A. Nellaippan, N. Rameshbabu, Estimation of crystallite size, lattice strain and dislocation density of nanocrystalline carbonate substituted hydroxyapatite by X-ray peak variance analysis, *Procedia Mater. Sci.* **5** (2014) 212–221, <https://doi.org/10.1016/j.mspro.2014.07.260>.
- [36] M. Amaya, J. Nakamura, T. Fuketa, Measurements of crystal lattice strain and crystallite size in irradiated UO<sub>2</sub> pellet by X-ray diffractometry, *J. Nucl. Sci. Technol.* **45** (2008) 244–250, <https://doi.org/10.1080/18811248.2008.9711433>.
- [37] X. Zhao, S. Li, M. Zhang, Y. Liu, T.B. Sercombe, S. Wang, Y. Hao, R. Yang, L. E. Murr, Comparison of the microstructures and mechanical properties of Ti-6Al-4V fabricated by selective laser melting and electron beam melting, *Mater. Des.* **95** (2016) 21–31, <https://doi.org/10.1016/j.matdes.2015.12.135>.
- [38] K.G. Prashanth, S. Scudino, J. Eckert, Defining the tensile properties of Al-12Si parts produced by selective laser melting, *Acta Mater.* **126** (2017) 25–35, <https://doi.org/10.1016/j.actamat.2016.12.044>.
- [39] S.H. Sun, K. Hagihara, T. Nakano, Effect of scanning strategy on texture formation in Ni-25 at.%Mo alloys fabricated by selective laser melting, *Mater. Des.* **140** (2018) 307–316, <https://doi.org/10.1016/j.matdes.2017.11.060>.
- [40] P. Wang, J. Eckert, K. Gokuldoss Prashanth, M. wei Wu, I. Kaban, L. xia XI, S. Scudino, A Review of Particulate-Reinforced Aluminum Matrix Composites Fabricated by Selective Laser Melting, 2020, [https://doi.org/10.1016/S1003-6326\(20\)65357-2](https://doi.org/10.1016/S1003-6326(20)65357-2).
- [41] K.G. Prashanth, S. Scudino, H.J. Klauss, K.B. Surreddi, L. Löber, Z. Wang, A. K. Chaubey, U. Kühn, J. Eckert, Microstructure and mechanical properties of Al-12Si produced by selective laser melting: effect of heat treatment, *Mater. Sci. Eng. A* **590** (2014) 153–160, <https://doi.org/10.1016/j.msea.2013.10.023>.
- [42] R. Ummethala, P.S. Karamched, S. Rathinavelu, N. Singh, A. Aggarwal, K. Sun, E. Ivanov, L. Kollo, I. Okulov, J. Eckert, K.G. Prashanth, Selective laser melting of high-strength, low-modulus Ti-35Nb-7Zr-5Ta alloy, *Materials* **14** (2020), <https://doi.org/10.1016/j.mta.2020.100941>.
- [43] H.F. Memurdie, M.C. Morris, E.H. Evans, B. Paretzkin, W. Wongng, C.R. Hubbard, Standard X-ray diffraction powder patterns from the jcpsds research association, *Powder Diffr.* **1** (1986) 265–275, <https://doi.org/10.1017/S0885715600011829>.
- [44] B. Babu, L.E. Lindgren, Dislocation density based model for plastic deformation and globalization of Ti-6Al-4V, *Int. J. Plast.* **50** (2013) 94–108, <https://doi.org/10.1016/j.jiplas.2013.04.003>.
- [45] B.J. Hayes, B.W. Martin, B. Welk, S.J. Kuhr, T.K. Ales, D.A. Brice, I. Ghamarian, A. H. Baker, C.V. Haden, D.G. Harlow, H.L. Fraser, P.C. Collins, Predicting tensile properties of Ti-6Al-4V produced via directed energy deposition, *Acta Mater.* **133** (2017) 120–133, <https://doi.org/10.1016/j.actamat.2017.05.025>.
- [46] G. Casalino, F. Curcio, F.M.C. Minutolo, Investigation on Ti6Al4V laser welding using statistical and Taguchi approaches, *J. Mater. Process. Technol.* **167** (2005) 422–428, <https://doi.org/10.1016/j.jmatprotec.2005.05.031>.
- [47] S.R. Sabuj, M. Hamamura, Random cognitive radio network performance in Rayleigh-lognormal environment, *2017 14th, IEEE Annu. Consum. Commun. Netw. Conf. CCNC* **6** (2017) 992–997, <https://doi.org/10.1109/CCNC.2017.7983268>.
- [48] D. Zhang, W. Wang, Y. Guo, S. Hu, D. Dong, R. Poprawe, J.H. Schleißenbaum, S. Ziegler, Numerical simulation in the absorption behavior of Ti6Al4V powder materials to laser energy during SLM, *J. Mater. Process. Technol.* **268** (2019) 25–36, <https://doi.org/10.1016/j.jmatprotec.2019.01.002>.
- [49] M. Rombouts, L. Froyen, A.V. Gusarov, E.H. Benetfour, C. Glorieux, Photopyroelectric measurement of thermal conductivity of metallic powders, *J. Appl. Phys.* **97** (2005), 024905, <https://doi.org/10.1063/1.1832740>.
- [50] D. Zhang, P. Zhang, Z. Liu, Z. Feng, C. Wang, Y. Guo, Thermo-fluid field of molten pool and its effects during selective laser melting (SLM) of Inconel 718 alloy, *Addit. Manuf.* **21** (2018) 567–578, <https://doi.org/10.1016/j.addma.2018.03.031>.
- [51] K. Bartsch, F. Lange, M. Grawol, C. Emmelmann, Novel approach to optimized support structures in laser beam melting by combining process simulation with topology optimization, *J. Laser Appl.* **31** (2019), 022302, <https://doi.org/10.2351/1.5096096>.
- [52] G. Vastola, Q.X. Pei, Y.W. Zhang, Predictive model for porosity in powder-bed fusion additive manufacturing at high beam energy regime, *Addit. Manuf.* **22** (2018) 817–822, <https://doi.org/10.1016/j.addma.2018.05.042>.
- [53] J. Metelkova, Y. Kinds, K. Kempen, C. de Formanoir, A. Witvrouw, B. Van Hooreweder, On the influence of laser defocusing in Selective Laser Melting of 316L, *Addit. Manuf.* **23** (2018) 161–169, <https://doi.org/10.1016/j.addma.2018.08.006>.
- [54] T. Ahmed, H.J. Rack, Phase transformations during cooling in  $\alpha + \beta$  titanium alloys, *Mater. Sci. Eng. A* **243** (1998) 206–211, [https://doi.org/10.1016/S0921-5093\(97\)00802-2](https://doi.org/10.1016/S0921-5093(97)00802-2).
- [55] P. Fischer, V. Romano, H.P. Weber, N.P. Karapatis, E. Boillat, R. Glardon, Sintering of commercially pure titanium powder with a Nd:YAG laser source, *Acta Mater.* **51** (2003) 1651–1662, [https://doi.org/10.1016/S1359-6454\(02\)00567-0](https://doi.org/10.1016/S1359-6454(02)00567-0).
- [56] M. Bayat, A. Thanki, S. Mohanty, A. Witvrouw, S. Yang, J. Thorborg, N.S. Tiedje, J. H. Hattel, Keyhole-induced porosities in laser-based powder bed fusion (L-PBF) of Ti6Al4V: high-fidelity modelling and experimental validation, *Addit. Manuf.* **30** (2019), <https://doi.org/10.1016/j.addma.2019.100835>.
- [57] T. Maity, N. Chawake, J.T. Kim, J. Eckert, K.G. Prashanth, Anisotropy in local microstructure – does it affect the tensile properties of the SLM samples? *Manuf. Lett.* **15** (2018) 33–37, <https://doi.org/10.1016/j.mfglet.2018.02.012>.
- [58] C. Meier, R.W. Penny, Y. Zou, J.S. Gibbs, A.J. Hart, Thermophysical Phenomena in Metal Additive Manufacturing by Selective Laser Melting: Fundamentals,

- Modeling, Simulation and Experimentation, 2017, pp. 241–316, <https://doi.org/10.1615/AnnualRevHeatTransfer.2018019042>. ArXiv. 20.
- [59] L. Facchini, E. Magalini, P. Robotti, A. Molinari, S. Höges, K. Wissenbach, Ductility of a Ti-6Al-4V alloy produced by selective laser melting of prealloyed powders, *Rapid Prototyp. J.* 16 (2010) 450–459, <https://doi.org/10.1108/13552541011083371>.
- [60] F.J. Gil, M.P. Ginebra, J.M. Manero, J.A. Planell, Formation of  $\alpha$ -Widmanstätten structure: effects of grain size and cooling rate on the Widmanstätten morphologies and on the mechanical properties in Ti6Al4V alloy, *J. Alloys Compd.* 329 (2001) 142–152, [https://doi.org/10.1016/S0925-8388\(01\)01571-7](https://doi.org/10.1016/S0925-8388(01)01571-7).
- [61] C. Zhao, Z. Wang, D. Li, L. Kollo, Z. Luo, W. Zhang, K.G. Prashanth, Cu-Ni-Sn alloy fabricated by melt spinning and selective laser melting: a comparative study on the microstructure and formation kinetics, *J. Mater. Res. Technol.* 9 (2020) 13097–13105, <https://doi.org/10.1016/j.jmrt.2020.09.047>.
- [62] Z. Wang, M. Xie, Y. Li, W. Zhang, C. Yang, L. Kollo, J. Eckert, K.G. Prashanth, Premature failure of an additively manufactured material, *NPG Asia Mater.* 12 (2020) 1–10, <https://doi.org/10.1038/s41427-020-0212-0>.
- [63] P. Wang, H.C. Li, K.G. Prashanth, J. Eckert, S. Scudino, Selective laser melting of Al-Zn-Mg-Cu: heat treatment, microstructure and mechanical properties, *J. Alloys Compd.* 707 (2017) 287–290, <https://doi.org/10.1016/j.jallcom.2016.11.210>.
- [64] K.G. Prashanth, J. Eckert, Formation of metastable cellular microstructures in selective laser melted alloys, *J. Alloys Compd.* 707 (2017) 27–34, <https://doi.org/10.1016/j.jallcom.2016.12.209>.
- [65] T. DebRoy, H.L. Wei, J.S. Zuback, T. Mukherjee, J.W. Elmer, J.O. Milewski, A. M. Beese, A. Wilson-Heid, A. De, W. Zhang, Additive manufacturing of metallic components – process, structure and properties, *Prog. Mater. Sci.* 92 (2018) 112–224, <https://doi.org/10.1016/j.pmatsci.2017.10.001>.
- [66] J.J. Hurly, Thermophysical properties of gaseous CF<sub>4</sub> and C<sub>2</sub>F<sub>6</sub> from speed-of-sound measurements, *Int. J. Thermophys.* 20 (1999) 455–484, <https://doi.org/10.1007/s10765-005-0001-6>.
- [67] A.N. Arce, Thermal modeling and simulation of electron beam melting for rapid prototyping of Ti6Al4V alloys. <https://repository.lib.ncsu.edu/handle/1840.16/8202>, 2012. (Accessed 11 November 2020).



**Paper III**

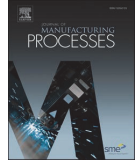
**Karimi, J.,** Xie, M. S., Wang, Z., & Prashanth, K. G. (2021). Influence of substructures on the selective laser melted Ti-6Al-4V alloy as a function of laser re-melting. *Journal of Manufacturing Processes*, 68, 1387–1394.





Contents lists available at ScienceDirect

## Journal of Manufacturing Processes

journal homepage: [www.elsevier.com/locate/manpro](http://www.elsevier.com/locate/manpro)

Technical paper

## Influence of substructures on the selective laser melted Ti-6Al-4V alloy as a function of laser re-melting

J. Karimi<sup>a,\*</sup>, M.S. Xie<sup>b</sup>, Z. Wang<sup>b,\*</sup>, K.G. Prashanth<sup>a,c,d</sup><sup>a</sup> Department of Mechanical and Industrial Engineering, Tallinn University of Technology, Ehitajate tee 5, 19086 Tallinn, Estonia<sup>b</sup> Guangdong Key Laboratory for Advanced Metallic Materials Processing, South China University of Technology, Guangzhou, 510640 Guangdong, China<sup>c</sup> Erich Schmid Institute of Materials Science, Austrian Academy of Sciences, Jahnstraße 12, A-8700 Leoben, Austria<sup>d</sup> CBCMT, School of Engineering, Vellore Institute of Technology, Vellore, 632014 Tamil Nadu, India

## ARTICLE INFO

## Keywords:

Selective laser melting  
Microstructure  
Substructure  
Twin  
Dislocation density  
Ti6Al4V

## ABSTRACT

This study investigates the effects of melting sequence on the microstructure, substructure, and mechanical properties of SLM Ti6Al4V alloys. Acicular  $\alpha'$  martensite was observed in all the SLM samples, and the dimensions of the  $\alpha'$  phase were changed with the melting sequence. Twins appear between acicular  $\alpha'$  martensite, and a large number of dislocations were observed in the material and within  $\alpha'$  martensite. The density of twins and dislocations increased with increasing melting sequence from single melting to triple melting. Tensile strength properties including ultimate tensile strength and yield stress, and hardness increased with increasing melting sequence from single melting to triple melting. The present results clearly prove that the melting sequence plays a significant role in determining the microstructure, substructure, and mechanical properties of the SLM as-built materials.

## 1. Introduction

Ti6Al4V has been widely used in many industries due to the superior properties like corrosion resistance, high strength, and low density [1,2]. Laser powder bed fusion (L-PBF) process/selective laser melting (SLM) can be used to manufacture Ti6Al4V components with complex shapes [3,4]. However, due to the complexity of the SLM process, the mechanical property of the Ti6Al4V can vary depending on the microstructure (phase constitution, morphology, distribution, etc.) [5], and substructure (i.e., dislocation, twinning, etc.) [6]. Therefore, a considerable volume of research has been carried out on the effect of the microstructure on the mechanical properties of SLM Ti6Al4V alloys. Although further understanding of the substructure of SLM Ti6Al4V alloys and studying its effect on the mechanical properties is vital, it has not been studied systematically and in-depth yet.

It is well known that the grain boundaries act as barriers to the dislocations motion, where it may effectively increase the hardness and tensile strength of the material, according to the Hall–Petch relation [7,8]. Twin boundary similar to grain boundary may also act as barriers to dislocation motion [9]. Shen et al. [10] investigated the effect of nano-scale twins on the tensile strength and reported that increasing the twinning density led to an increase in the tensile strength. In another

work, Cao et al. [11] studied the effect of quenching rate to understand twin formation mechanism in Ti6Al4V alloys, and concluded that the density of twins increased with increasing the quenching rate. They used their result of the quenching effect on the substructure to explain the tension and compression twin in the SLM process, where the process nature such as the thermal effects of the melt pool on the solidified layer (s) was ignored. The thermal effects of the melt pool and the cooling rate on microstructure and substructure have not been investigated in depth.

Many studies have reported the application of a melting sequence to increase the density and improve the surface finish of the components fabricated by the SLM. In our previous work [12], we have studied the effect of melting sequence on the inhomogeneity in the microstructure and the mechanical properties, including hardness of SLM Ti6Al4V alloys. In addition, the mechanical properties obtained from the tensile test of the SLM samples with remelting were discussed in detail, which exhibited a reduction in ductility with increasing the melting sequence from single melting to triple melting. We concluded that the melting sequence improved the mechanical properties, and reduced the inhomogeneity in the microstructure and mechanical properties of the SLM parts. However, the effects of melting sequence on the substructure have not been studied. In this work, we manufactured Ti6Al4V samples by the SLM with melting sequence, where increasing melting sequence

\* Corresponding authors.

E-mail addresses: [jkarim@taltech.ee](mailto:jkarim@taltech.ee) (J. Karimi), [wangzhi@scut.edu.cn](mailto:wangzhi@scut.edu.cn) (Z. Wang).<https://doi.org/10.1016/j.jmapro.2021.06.059>

Received 17 August 2020; Received in revised form 1 June 2021; Accepted 19 June 2021

Available online 2 July 2021

1526-6125/© 2021 The Society of Manufacturing Engineers. Published by Elsevier Ltd. All rights reserved.

from single melting to double and triple melting increased the cooling rate of the melt pool [13]. The main purpose of this study is to understand clearly the effects of melting sequence on phase morphologies as well as substructure (dislocation and twin), and the effects on mechanical properties, particularly hardness and tensile properties.

## 2. Experimental methods

### 2.1. Materials and SLM process

Bulk specimens were fabricated by SLM from spherical gas-atomized powder with an average size of  $21 \pm 5 \mu\text{m}$ . The SLM process was carried out by a Realizer SLM-50 equipped with a 120 W fiber laser, and a spot size of  $\sim 39 \mu\text{m}$ . The SLM processing parameters used for fabricating the samples are as follows: hatch distance  $60 \mu\text{m}$ , scanning speed  $1000 \text{ mm/s}$ , layer thickness  $25 \mu\text{m}$ , and hatch rotation  $73^\circ$ . However, variation was carried out in such a way that each layer of powder was melted either once, twice, or thrice with the energy density of  $40 \text{ J/mm}^3$ . The volumetric energy density (VED) was used to measure input energy, which is defined as follows:

$$VED = \frac{P}{v_s \cdot h \cdot d} \quad (1)$$

where VED is the energy input ( $\text{J/mm}^3$ ),  $P$  is the laser power (W),  $v_s$  is the scanning speed ( $\text{mm/s}$ ),  $h$  is the hatch space (mm) and  $d$  is the layer thickness of the powder bed (mm) [14]. All the SLM samples were fabricated on a 20 mm thick Ti platform in a high purity argon gas.

### 2.2. Material characterization

The crystalline structure of the Ti6Al4V alloys was characterized using X-ray diffractometer (Bruker-axs D5005, Germany) with Cu-K $\alpha$  radiation ( $\lambda = 0.154056 \text{ nm}$ ). A step size of  $0.01^\circ$  was used with an exposure time of 5 s per step along the direction of deposition. The Scherer equation was used to determine the crystallite size, as follows:

$$D = \frac{K\lambda}{\beta \cos\theta} \quad (2)$$

where  $D$  is the crystallite size,  $\beta$  is the breadth of the X-ray diffraction peak,  $\theta$  is the Bragg angle for the peak,  $K$  is the shape factor, and  $\lambda$  is the wavelength of the X-ray (i.e.,  $\lambda_{\text{Cu-K}\alpha} 1.5406 \text{ \AA}$ ). The dislocation density of the XRD data was estimated using the Williamson-Hall approach, using the equation:

$$\beta \frac{\cos\theta}{\lambda} = \frac{0.9}{D} + 2\epsilon \frac{\sin\theta}{\lambda} \quad (3)$$

$$\rho = 14.4 \frac{\epsilon^2}{b^2} \quad (4)$$

where  $\epsilon$  is lattice strain,  $\rho$  is dislocation density, and  $b$  is the magnitude of the Burgers vector. Lattice parameters calculated based on the Bragg's law and plane spacing equation are as follows:

$$\frac{1}{d^2} = \frac{4}{3} \left( \frac{h^2 + hk + k^2}{a^2} \right) + \frac{l^2}{c^2} \quad (5)$$

$$\lambda = 2d\sin\theta \quad (6)$$

where  $h$ ,  $k$ , and  $l$  are miller indices,  $a$  and  $c$  are the lattice constants, and  $d$  is inter-planar spacing. The microstructure was characterized by scanning electron microscopy (SEM, Zeiss FEG, Germany) and transmission electron microscopy (TEM, Tecnai G2 F20, FEI, Germany) coupled with energy-dispersive X-ray spectroscopy (EDS). Standard metallographic practices were used for the mounting and polishing of the samples. The samples were etched with Kroll reagent (91 ml distilled water, 6 ml nitric acid, and 3 ml hydrofluoric acid). The average

dislocation density of the TEM data was determined using the equations, as follow [15]:

$$l = \frac{4}{\pi} \rho \quad (7)$$

$$\rho = \frac{l}{tA} \quad (8)$$

where  $l_p$  is the projected length of dislocation lines,  $l$  is the length of dislocation lines,  $A$  is the area, and  $t$  is the sample thickness, approximated by application of the approach suggested by Allen [16]. The average number and width of twins and dislocation density of the TEM images were measured in an area of  $\sim 100 \mu\text{m}^2$  in each sample using an image analyzer software. The hardness tests were conducted on a Vickers INDENTEC 5030SKV machine with a load of 5 kgf and a dwell time of 10 s. The uniaxial tensile tests were carried out according to ASTM standard: ASTM E8/E8M-13a (where the dimensions are modified to suit the length of 52 mm as per the ratio mentioned in the standard) using a servo-hydraulic Instron 8516 machine at room temperature with a strain rate of  $0.001 \text{ mm/s}$ . At least three specimens for each condition were tested to evaluate the reproducibility of the results.

## 3. Results

### 3.1. Phase analysis

Fig. 1 exhibits the X-ray diffraction (XRD) of the SLM Ti6Al4V samples with melting sequence, where the patterns show the presence of  $\alpha'$  martensite phase. Similar positions and intensities of XRD peaks can be observed among the diffraction patterns of single, double, and triple melted samples. Table 1 shows the crystallite size and lattice strain of single, double, and triple melted samples. Moreover, the lattice parameter ( $\alpha$ ) of the SLM samples is  $0.2925 \pm 0.0008 \text{ nm}$ ,  $0.2926 \pm 0.0009 \text{ nm}$ , and  $0.2927 \pm 0.0009 \text{ nm}$  for single, double, and triple melting, respectively (Table 1).

### 3.2. SEM and TEM observations

Fig. 2a shows the SEM micrograph of the Ti6Al4V sample prepared by the SLM, where the microstructure consists of acicular  $\alpha'$  martensite (hcp), in agreement with Vrancken et al. [17]. The average width and the average length of the acicular  $\alpha'$  martensite are  $0.41 \pm 0.12 \mu\text{m}$  and  $14 \pm 6 \mu\text{m}$ , respectively. In the as-built SLM sample, a large number of

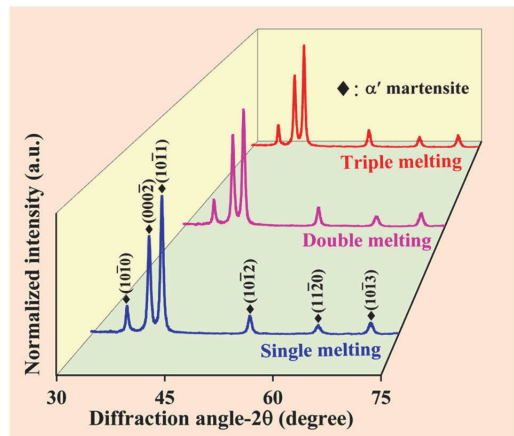


Fig. 1. X-ray diffraction patterns for the SLM processed Ti6Al4V sample as a function of melting sequence.

**Table 1**

Crystallite size, lattice strain, lattice parameter, the twins' dimension, and the average inter-planar spacing of the Ti6Al4V SLM samples as a function of the number of melting steps.

	Melting number		
	Single	Double	Triple
Crystallite size (nm)	13 ± 1	12 ± 0.6	14 ± 0.9
Lattice strain (%)	0.7 ± 0.1	0.7 ± 0.2	0.6 ± 0.1
Lattice parameter (a) (nm)	0.2925 ± 0.0008	0.2926 ± 0.0009	0.2927 ± 0.0009
Twin length (µm)	0.8 ± 0.2	0.9 ± 0.9	1 ± 0.6
Distance between twins (µm)	0.15 ± 0.06	0.07 ± 0.03	0.15 ± 0.1
Inter-planar spacing (twin/ α') (nm)	0.285	0.233	0.248
Inter-planar spacing (matrix) (nm)	0.259	0.233	0.285

the acicular α' martensite are twined, shown in the magnified view inserted in Fig. 2a. The average thickness of the twined acicular α' martensite, which exhibits parallel lens-shaped acicular, is 0.31 ± 0.1 µm. Lu et al. [9] also reported the twined acicular α' martensite in the as-built SLM Ti6Al4V.

The microstructural features of the fabricated sample by the SLM are also characterized by the TEM. Acicular α' martensite is observed in the TEM image of the as-built SLM (Fig. 2b), where the distance between α' martensite is ~0.8 µm (Fig. 2b). As shown in Fig. 2b (and its higher magnification image of the rectangle in 2c), the twins existed almost uniformly between acicular α' martensite with an angle, where the average length and distance between them are 0.8 ± 0.2 and 0.15 ± 0.06 µm, respectively. Moreover, high-density dislocations arraying in tangles were observed inside the acicular α' martensite (Fig. 2c). Dislocation lines are observed on the edge of the acicular α' martensite (Fig. 2e), where the average length and average width are 13 ± 2 and 2 ± 0.6 nm, respectively. Fig. 2d shows the high-resolution HR-TEM image

from the rectangle in Fig. 2e, where the average inter-planar spacing of the α' martensite and matrix is 0.285 nm and 0.259 nm, respectively (Table 1). The difference in the inter-planar spacing in the region between the acicular α' martensite and matrix is may probably a Moiré pattern, similar to the report by Li et al. [18]. Besides, the corresponding selected area electron diffractions (SAEDs) in Fig. 2f exhibit hcp crystal structure.

Fig. 3a shows the SEM micrograph of the Ti6Al4V sample prepared by the SLM with double melting, where the average width and the average length of acicular α' martensite are 0.56 ± 0.1 and 6 ± 1 µm, respectively. TEM images of the double melted sample show a large number of uniformly distributed twins, where the average length and average distance between twins are 0.9 ± 0.9 and 0.07 ± 0.03 µm, respectively (Table 1). High-density dislocations arraying in tangles were observed in the double melted sample, as shown in Fig. 3b. Furthermore, dislocation lines were also observed in the double melted sample (Fig. 3e), in which the average length and the average width are 50 ± 10 and 4 ± 1 nm, respectively. A close observation of the substructure in the surface layer was carried out by using HR-TEM, as depicted in Fig. 3d, where the average inter-planar spacing of the twin and matrix is 0.233 nm (Table 1). The misorientation angle between the twin and matrix is determined to be ~36° (Fig. 3d), and Shockley partial dislocations appear on the twin boundary. The corresponding SAEDs in Fig. 3f identifies the twinning mode as  $\bar{1}011$  type twin. Manero, Gil, and Planell [19] studied the Ti6Al4V alloys with α' martensitic structure and noted  $\bar{1}011$  type twin as compression and the easiest twin type to produce.

Fig. 4a shows the SEM micrograph of the Ti6Al4V sample prepared by the SLM with triple melting, where the average width and the average length of acicular α' martensite are 0.6 ± 0.14 and 5 ± 2 µm, respectively. Similar to the single melted sample, the twins appear between acicular α' martensite with an angle (Fig. 4b). A large number of twins were observed in the TEM images of the triple melted sample, of which the average length and distance between them are 1 ± 0.6 and 0.15 ±

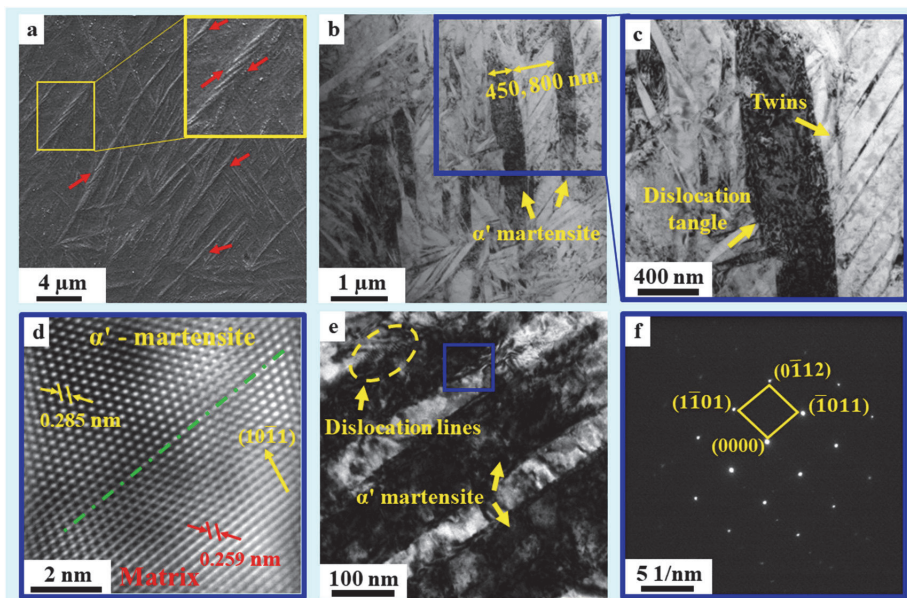


**Fig. 2.** Microstructure and substructure of SLM with single melting. a SEM image showing the acicular α' martensite microstructure. The red arrows indicate twined acicular α' martensite. b TEM image showing acicular α' martensite and twins. c TEM image showing a high magnification image of the rectangle in b. d HR-TEM image showing the matrix and acicular of the rectangle in e. e TEM image showing acicular α' martensite and dislocation lines. f SAED pattern of the rectangle in e, which exhibits hcp crystal structure. (For interpretation of the references to color in this figure legend, the reader is referred to the web version of this article.)



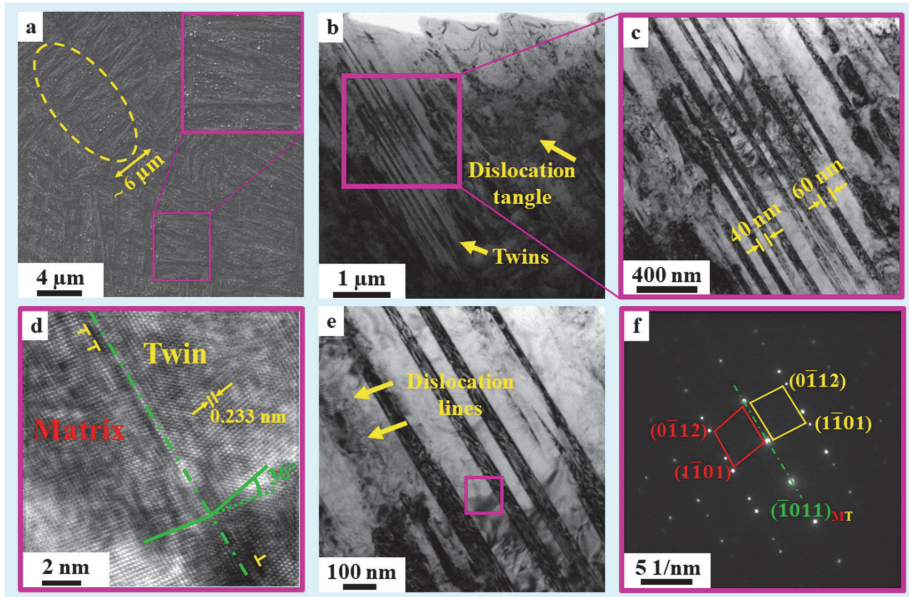


Fig. 3. Microstructure and substructure of SLM with double melting. a SEM image showing the acicular  $\alpha'$  martensite microstructure. b TEM image showing uniformly distributed twins. c TEM image showing a high magnification image of the rectangle in b. d HR-TEM image showing the matrix and twin of the rectangle in e. e TEM image showing twin and dislocation lines. f SAED pattern of the rectangle in e, which indicates the compression twin type.

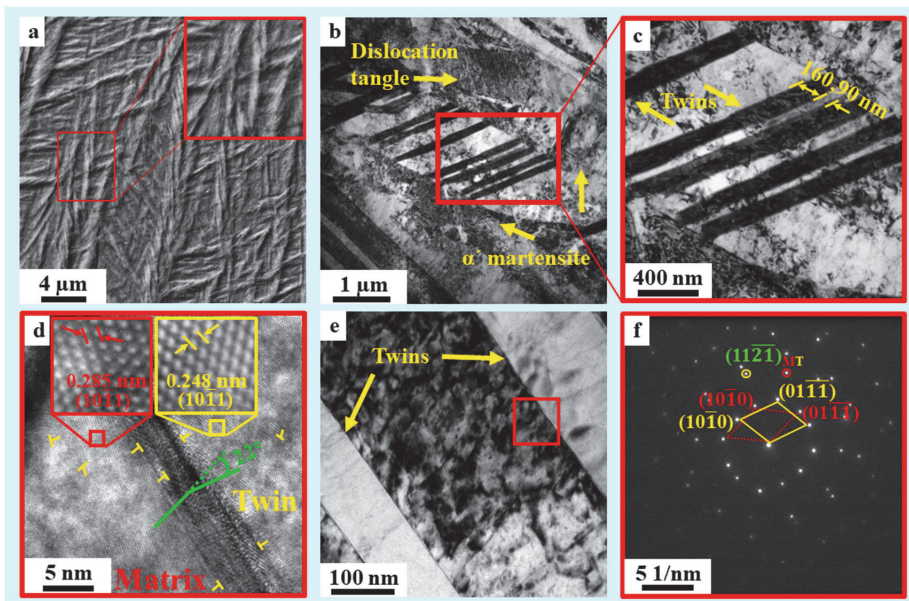


Fig. 4. Microstructure and substructure of SLM with triple melting a SEM image showing the acicular  $\alpha'$  martensite microstructure. b TEM image showing uniformly distributed twins. c TEM image showing a high magnification image of the rectangle in b. d HR-TEM image showing the matrix and twin of the rectangle in e. e TEM image showing twin and dislocation lines. f SAED pattern of the rectangle in e, which indicates the tensile twin type.

0.1  $\mu\text{m}$ , respectively (Table 1). High-density dislocations arraying in tangles were also observed inside the matrix and acicular  $\alpha'$  martensite (Fig. 4b). A close observation of the substructure in the surface layer was

carried out by using HR-TEM, as depicted in Fig. 4d, where the average inter-planar spacing of the twin and matrix is 0.248 and 0.285 nm, respectively. The misorientation angle between twin and matrix is

determined to be 22° on the twin boundary, and a large number of Shockley partial dislocations appear on the twin boundaries, and in the matrix and twin zone. The corresponding SAEDs in Fig. 4f identifies the 112̄1 as tensile twin mode, which is frequently observed in high strain conditions, as noted by Lainé et al. [20].

### 3.3. Tensile properties and hardness measurement

Fig. 5 shows the surface hardness and its deviation of SLM specimens with melting sequence, where it increased from 330 ± 10 HV for the single melted sample to 370 ± 12 HV for the triple melted sample. In addition, the ultimate tensile strength (UTS) and the yield stress (YS) of the specimens increased from single to triple melting. However, the elongation decreased by ~50% from single to triple melting (Fig. 5).

SEM images illustrated that the distance between acicular α' martensite decreases from single melting to triple melting, and the surface in the double and triple melted sample consists of thicker acicular α' martensite. In addition, TEM images show as the melting sequence increases from single to triple melting, the substructure (twin size and dislocation density) changes. It is difficult to determine the effect of process parameters or melting sequence on the material properties in the SLM since there are several factors that influence the microstructure as well as the substructure of the fabricated samples. However, it would be logical to say that the cooling rate is one of the most important factors that may cause the change in the density and size of twins and dislocation in the SLM process with melting sequence.

## 4. Discussion

### 4.1. Microstructure features

Fig. 6a shows the schematic representation showing the microstructural evolution of SLM Ti6Al4V alloys as a function of the melting sequence. Based on the SEM observation (Figs. 2a, 3a, and 4a), the microstructure of all the fabricated samples by the SLM with melting sequence consists of acicular α' martensite, which is a result of rapid cooling rate (~10<sup>6</sup> C/s [13]) of molten metal during the SLM. The already solidified layer is re-melted during double, and triple melting sequence, where the thermal conductivity of the double, and the triple melted (bulk) samples is higher than the single melted sample (loose powder) [21]. Consequently, the cooling rate of the melt pool in double, and triple melted samples is higher than in single melted samples [22]. Hence, the average width of acicular α' martensite increased from 0.405 ± 0.12 μm for the single melted sample to 0.6 ± 0.137 for the triple melted sample. However, the length of the acicular α' martensite decreased by ~65% with increasing the re-melting step. In addition, a

large number of long and thin acicular α' martensite were twined with the same angle, which is probably due to the ununiformed heat distribution in the powder bed, and the high internal strain of the produced sample by the SLM.

### 4.2. Change in the substructure during melting sequence

#### 4.2.1. Twinning in acicular α' martensite

In the SLM process, the material is subjected to the large thermal gradient (10<sup>7</sup> K/m [23]) because of an extremely short duration of laser-material interaction (rapid heating by the laser beam), accompanying highly localized heat input (<2600 °C [24]), and low thermal conductivity of powder bed (two orders of magnitude smaller than thermal conductivity in solid). During depositing the first layer, a bending moment is generated with equal forces, and this process becomes more complex as more layers build up [25]. When the laser beam melts the material, the top layer expands (with the thermal expansion coefficient of ~8.5 × 10<sup>-6</sup>/K for Ti6Al4V) due to the large thermal gradient, while the preceding (solidified) layer restricts it. This induces elastic compressive stress in the top layer of the component that can rise above the yield stress of the material. When the upper layers cool off, plastically compressed upper layers start shrinking, since their thermal contraction is restrained; consequently, the compressive stresses change to tensile stresses. Each successive SLM layer will generate stresses near the molten pool, generating a complicated superposition of stresses and strains [26]. Therefore, plastic deformations may occur in the material and the solidifying layer. Boruah et al. [25] proposed a model with assumptions to measure residual stresses of layer by layer building up of SLM, take into consideration the force and moment equilibrium and they concluded that the residual stresses increase with increasing the number of deposited layer (or melting sequence), using:

$$\Delta\sigma(y) = k - 6ky\Delta h \sum_{m+1}^n \left\{ \frac{h+n\Delta h}{\{h+(n-1)\Delta h\}^3} \right\} + k\Delta h \sum_{m+1}^n \left\{ \frac{2h+(2n+1)\Delta h}{\{h+(n-1)\Delta h\}^2} \right\} \quad (9)$$

where Δσ(y) is the stress increase in the mth layer because of depositing the nth layer, m is an individual deposited layer, n is the number of deposited layers, y is space from the substrate surface, and k is residual stress of the deposited layer. Due to the higher cooling rate in the double and triple melted samples than the as-built sample, tensile/compressive stresses are higher in the double and triple melted samples compared to the as-built sample. Shiomi et al. [27] investigated the effect of re-melting on residual stress and reported that the average residual stress in the re-melted sample is higher than the as-built SLM sample.

Plastic deformation by slip and twinning are considered as competitive mechanisms, where twinning can form in a few microseconds, whereas for the formation of a slip band there is a delay time of several milliseconds [28]. In addition, twinning may occur due to the limitation of the slip systems or increasing of the critical resolved shear stress. Hence, the stress needed for the twinning is lower than the stress needed for the slip. The compressive and tensile stresses cause plastic deformation in the material to relieve the stress when the applied stress is above the yield stress of the material. Several studies have addressed strain accommodation and stress relief by twinning. Both the compressive and tensile twinning types accommodate strains inside the matrix, where the stress concentration can be relaxed either by a slip or by twinning. In addition, increasing cooling rate, from single melting to double and triple melting, has been suggested to be one of the most important factors that can enhance twinning probably because of the changes in the critical resolved shear stresses for twinning that favour twinning formation [29]. Based upon the TEM observation, the substructure of acicular α' martensite changes with melting sequence from single melting to triple melting, schematically described in Fig. 6a. Accordingly, the number and width of twins were measured and summarized in Fig. 6b. The number of twins increases with increasing

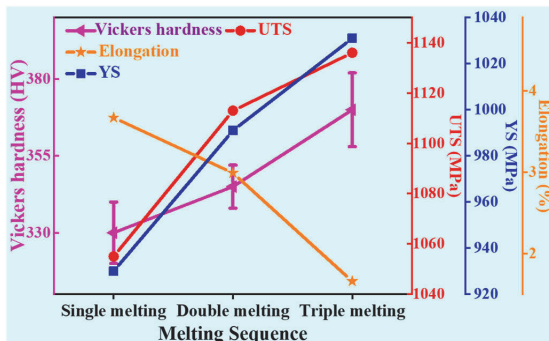


Fig. 5. Comparison of surface hardness, ultimate tensile strength (UTS), yield stress (YS), and elongation of the SLM Ti6Al4V alloys as a function of the melting sequence.

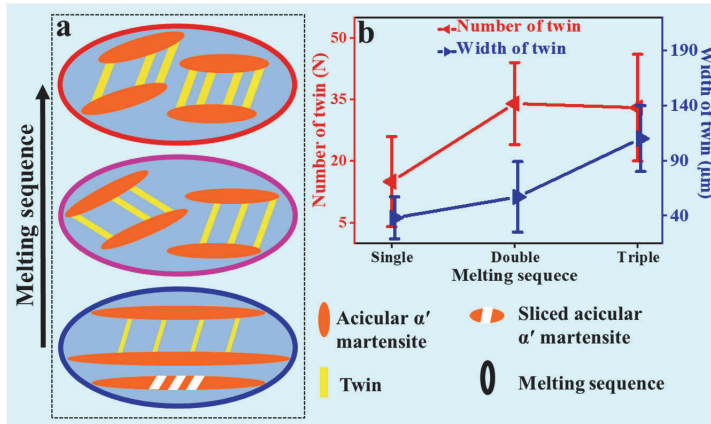


Fig. 6. Effect of melting sequence on microstructure and substructure. a Schematic illustration showing the development of the microstructure and substructure. Note that the blue, purple, and red oval indicate the single, double and triple melting. b The average number and the average width of twins, measured in the area of  $\sim 100 \mu\text{m}^2$ . (For interpretation of the references to color in this figure legend, the reader is referred to the web version of this article.)

melting sequence from single to triple melting, which is probably due to the higher residual stress and cooling rate in the double and triple melted samples. Cao et al. [30] investigated the effect of heat treatment of samples produced with SLM and concluded that annealing (6 h at  $800^\circ\text{C}$ ) led to removing the twins. In comparison with SLM, in laser metal deposition with the cooling rate in the range of  $\sim 10^3 \text{K/s}$  twinning is rarely reported [31]. In addition, the width of twins increased with increasing melting sequence from single to triple melting, where the size of martensite may influence twin morphology, whereby a thicker acicular  $\alpha'$  martensite promotes the formation of thicker twins. However, the

average length and distance of twins fluctuate with the melting sequence.

#### 4.2.2. Dislocation density in acicular $\alpha'$ martensite

Dislocations are formed due to the plastic deformation and rapid solidification in the SLM process, similar to deformation substructures that occurred after plastic deformation [32], which help to accommodate high internal stresses of the melted material. The substructure of acicular  $\alpha'$  martensite consists of a high density of tangled dislocations within the acicular, which is difficult and time-consuming to quantify.

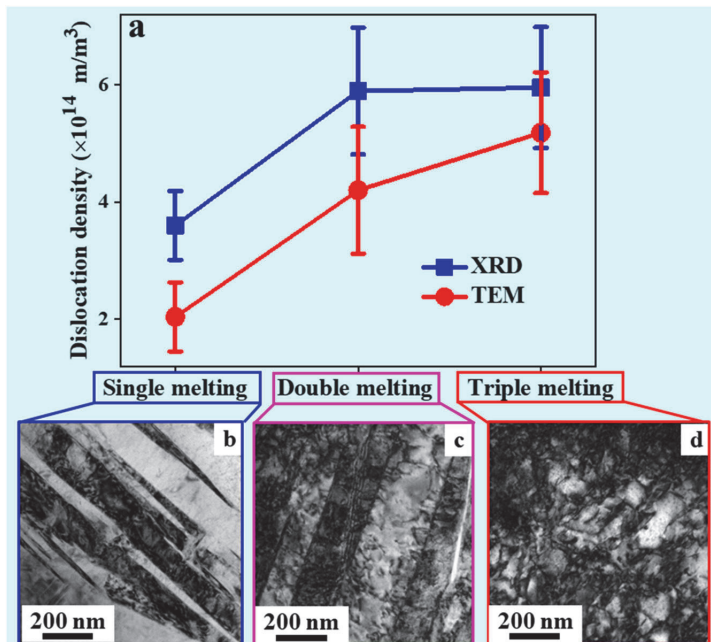


Fig. 7. The dislocation density of SLM Ti6Al4V samples obtained from TEM images and XRD data. a Comparison of dislocation densities of TEM and XRD data. The dislocation density in the SLM Ti6Al4V samples as a function of melting sequence: b single, c double, and d triple.

Dislocation lines are also observed in the sample, mostly near the boundary of acicular  $\alpha'$  martensite and twins (Figs. 2e and 3e), where the average length is  $\sim 30$  nm. As illustrated in the TEM micrograph (in Figs. 2–4), the dislocation density in the SLM Ti6Al4V is quite high and may change with the melting sequence. Accordingly, the dislocation density in SLM samples was measured and illustrated in Fig. 7a, where the dislocation density increases from single melting to triple melting. In addition, the dislocation density of the XRD data is also measured and illustrated in Fig. 7a, to compare with the amount obtained from the TEM images, where a similar pattern may be observed between the average dislocation densities and their deviations. However, XRD analysis provides information from significantly larger material volumes than TEM measurements. Fig. 7b–d also shows the increase of dislocation density as a function of melting sequence from single melting to triple melting.

#### 4.3. Mechanical properties

As illustrated, the density of dislocation and twins in the acicular  $\alpha'$  martensite phase increases with increasing melting sequence from single melting to triple melting. In addition, a high-density dislocation was observed within the twins and acicular  $\alpha'$  martensite, where the melting sequence led to an increase in the width of acicular martensite and twins. Twinning can serve as a barrier to the motion of dislocation during plastic deformation, and may effectively strengthen a material, according to Hall-Petch relation. Fig. 5 illustrated an increase in the surface hardness, the ultimate tensile strength, and the yield stress of SLM specimens with melting sequence from single melting to triple melting. However, the elongation decreased from single melting to triple melting.

The present work investigated the microstructure and substructure of SLM samples with melting sequence. The melting sequence strategy of the SLM specimen has contributed to the improvement in tensile properties (UTS and YS) and hardness. However, further research is needed to quantify the dislocation density inside twins and acicular  $\alpha'$  martensite. This information is vital to advance knowledge about the influence of substructure on mechanical properties, which is ignored in much research.

#### 5. Conclusion

This paper has described a detailed investigation of the microstructure and substructure of acicular  $\alpha'$  martensite of SLM Ti6Al4V alloys with the melting sequence. The following conclusions can be drawn.

- (1) The microstructure of the all SLM Ti6Al4V samples consists of acicular  $\alpha'$  martensite, where the average width of acicular  $\alpha'$  martensite increases with increasing the melting sequence from single melting to triple melting. However, the average length of acicular  $\alpha'$  martensite decreases as a function of the melting sequence.
- (2) The  $\alpha'$  martensite phase contains a high density of dislocations due to the rapid heating/cooling and the repeated thermal cycle of the SLM process. A great number of dislocations is identified within the acicular  $\alpha'$  martensite. The melting sequence led to an increase in the dislocation density from single melting to triple melting.
- (3) Twins have been identified uniformly between the acicular  $\alpha'$  martensite, and in the material frequently. Due to the increase of the residual stress and the cooling rate, the average number and width of twins also increased from single melting to triple melting.
- (4) The tensile properties, including UTS and YS, as well as the hardness of the samples, increased with increasing the melting sequence from single melting to triple melting. The increase in the mechanical properties is due to an increase in the density of

dislocation and twins, where twins can block the dislocation motion. The present results suggest that increasing the cooling rate during the melting sequence may be responsible for the change in substructure in the acicular  $\alpha'$  martensite, and consequently increasing the tensile strength and hardness.

#### Funding

This work was supported by the European Regional Development Fund under Grant MOBERC15 and ASTRA6-6; and partially supported by the National Natural Science Foundation of China (Grant No. 51701075); the Science and Technology Program of Guangzhou (Grant No. 201804010365).

#### Declaration of competing interest

The authors declare that they have no known competing financial interests or personal relationships that could have appeared to influence the work reported in this paper.

#### References

- [1] Tan X, Kok Y, Tan YJ, Vastola G, Pei QX, Zhang G, et al. An experimental and simulation study on build thickness dependent microstructure for electron beam melted Ti-6Al-4V. *J Alloys Compd* 2015;646:303–9. <https://doi.org/10.1016/j.jallcom.2015.05.178>.
- [2] Singh N, Hameed P, Ummethala R, Manivasagam G, Prashanth KG, Eckert J. Selective laser manufacturing of Ti-based alloys and composites: impact of process parameters, application trends, and future prospects. *Mater Today Adv* 2020;8: 100097. <https://doi.org/10.1016/j.mtadv.2020.100097>.
- [3] Karimi J, Ma P, Jia YD, Prashanth KG. Linear patterning of high entropy alloy by additive manufacturing. *Manuf Lett* 2020;24:9–13. <https://doi.org/10.1016/j.mfglet.2020.03.003>.
- [4] Prashanth KG, Kolla S, Eckert J. Additive manufacturing processes: selective laser melting, electron beam melting and binder jetting – selection guidelines. *Materials* 2017;10:672. <https://doi.org/10.3390/ma10060672>.
- [5] Thijs L, Verhaeghe F, Craeghs T, Van Humbeeck J, Kruth JP. A study of the microstructural evolution during selective laser melting of Ti-6Al-4V. *Acta Mater* 2010;58:3303–12. <https://doi.org/10.1016/j.actamat.2010.02.004>.
- [6] Yang J, Yu H, Yin J, Gao M, Wang Z, Zeng X. Formation and control of martensite in Ti-6Al-4V alloy produced by selective laser melting. *Mater Des* 2016;108: 308–18. <https://doi.org/10.1016/j.matdes.2016.06.117>.
- [7] Wang Z, Palmer TA, Beese AM. Effect of processing parameters on microstructure and tensile properties of austenitic stainless steel 304L made by directed energy deposition additive manufacturing. *Acta Mater* 2016;110:226–35. <https://doi.org/10.1016/j.actamat.2016.03.019>.
- [8] Zhao C, Wang Z, Li D, Kollo L, Luo Z, Zhang W, et al. Selective laser melting of Cu-Ni-Sn: a comprehensive study on the microstructure, mechanical properties, and deformation behavior. *Int J Plast* 2021;138:102926. <https://doi.org/10.1016/j.ijplas.2021.102926>.
- [9] Lu J, Lu H, Xu X, Yao J, Cai J, Luo K. High-performance integrated additive manufacturing with laser shock peening – induced microstructural evolution and improvement in mechanical properties of Ti6Al4V alloy components. *Int J Mach Tool Manuf* 2020;148:103475. <https://doi.org/10.1016/j.ijmactools.2019.103475>.
- [10] Shen YF, Lu L, Lu QH, Jin ZH, Lu K. Tensile properties of copper with nano-scale twins. *Scr Mater* 2005;52:989–94. <https://doi.org/10.1016/j.scriptamat.2005.01.033>.
- [11] Cao S, Zhang B, Yang Y, Jia Q, Li L, Xin S, et al. On the role of cooling rate and temperature in forming twinned  $\alpha'$  martensite in Ti-6Al-4V. *J Alloys Compd* 2020; 813:152247. <https://doi.org/10.1016/j.jallcom.2019.152247>.
- [12] Karimi J, Suryanarayana C, Okulov I, Prashanth KG. Selective laser melting of Ti6Al4V: effect of laser re-melting. *Mater Sci Eng A* 2021;805:140558. <https://doi.org/10.1016/j.msea.2017.11.103>.
- [13] Ali H, Ghadbeigi H, Mumtaz K. Effect of scanning strategies on residual stress and mechanical properties of selective laser melted Ti6Al4V. *Mater Sci Eng A* 2018; 712:175–87. <https://doi.org/10.1016/j.msea.2017.11.103>.
- [14] Prashanth KG, Scudino S, Maity T, Das J, Eckert J. Is the energy density a reliable parameter for materials synthesis by selective laser melting? *Mater Res Lett* 2017; 5:386–90. <https://doi.org/10.1080/21663831.2017.1299808>.
- [15] Graça S, Colaço R, Carvalho PA, Vilar R. Determination of dislocation density from hardness measurements in metals. *Mater Lett* 2008;62:3812–4. <https://doi.org/10.1016/j.matlet.2008.04.072>.
- [16] Allen SM. Foil thickness measurements from convergent-beam diffraction patterns. *Matter Struct Defects Mech Prop* 1981;43:325–35. <https://doi.org/10.1080/014861810823942>.
- [17] Vrancken B, Thijs L, Kruth JP, Van Humbeeck J. Heat treatment of Ti6Al4V produced by selective laser melting: microstructure and mechanical properties.

- J Alloys Compd 2012;541:177–85. <https://doi.org/10.1016/j.jallcom.2012.07.022>.
- [18] Li C, Chen J, Li W, He JJ, Qiu W, Ren YJ, et al. Study on the relationship between microstructure and mechanical property in a metastable  $\beta$  titanium alloy. J Alloys Compd 2015;627:222–30. <https://doi.org/10.1016/j.jallcom.2014.12.100>.
- [19] Manero JM, Gil FJ, Planell JA. Deformation mechanisms of Ti-6Al-4V alloy with a martensitic microstructure subjected to oligocyclic fatigue. Acta Mater 2000;48:3353–9. [https://doi.org/10.1016/S1359-6454\(00\)00152-X](https://doi.org/10.1016/S1359-6454(00)00152-X).
- [20] Lainé SJ. The role of twinning in the plastic deformation of alpha phase titanium [PhD dissertation]. University of Cambridge; 2017.
- [21] Meier C, Penny RW, Zou Y, Gibbs JS, Hart AJ. Thermophysical phenomena in metal additive manufacturing by selective laser melting: fundamentals, modeling, simulation, and experimentation. Annu Rev Heat Transf 2018;20:241–316. <https://doi.org/10.1615/annualrevheattransfer.2018019042>.
- [22] Kempen K, Thijs L, Vrancken B, Buls S, Van Humbeeck J, Kruth JP. Producing crack-free, high density M2 HSS parts by selective laser melting: pre-heating the baseplate. In: 24th Int SFF Symp-An Addit Manuf Conf SFF; 2013 August.
- [23] Vrancken B, Cain V, Knutsen R, Van Humbeeck J. Residual stress via the contour method in compact tension specimens produced via selective laser melting. Scr Mater 2014;87:29–32. <https://doi.org/10.1016/j.scriptamat.2014.05.016>.
- [24] Liu S, Yung CS. Additive manufacturing of Ti6Al4V alloy: a review. Mater Des 2019;164:8–12. <https://doi.org/10.1016/j.matdes.2018.107552>.
- [25] Boruah D, Zhang X, Doré M. An analytical method for predicting residual stress distribution in selective laser melted/sintered alloys. Residual Stress 2018;6:283–8. <https://doi.org/10.21741/9781945291890-45>.
- [26] Yadroitsev I, Yadroitsava I. Evaluation of residual stress in stainless steel 316L and Ti6Al4V samples produced by selective laser melting. Virtual Phys Prototyp 2015;10:67–76. <https://doi.org/10.1080/17452759.2015.1026045>.
- [27] Shiomi M, Osakada K, Nakamura K, Yamashita T, Abe F. Residual stress within metallic model made by selective laser melting process. CIRP Ann Manuf Technol 2004;53:195–8. [https://doi.org/10.1016/S0007-8506\(07\)60677-5](https://doi.org/10.1016/S0007-8506(07)60677-5).
- [28] Dieter GE. Mechanical metallurgy. Maidenhead, Berkshire: McGraw-Hill Book Company; 1988.
- [29] Poorhaydari K, Patchett BM, Ivey DG. Transformation twins in the weld HAZ of a low-carbon high-strength microalloyed steel. Mater Sci Eng A 2006;435–436:371–82. <https://doi.org/10.1016/j.msea.2006.07.055>.
- [30] Cao S, Chu R, Zhou X, Yang K, Jia Q, Lim CVS, et al. Role of martensite decomposition in tensile properties of selective laser melted Ti-6Al-4V. J Alloys Compd 2018;744:357–63. <https://doi.org/10.1016/j.jallcom.2018.02.111>.
- [31] Azarniya A, Colera XG, Mirzaali MJ, Sovizi S, Bartolomeu F, St Węglowski MK, et al. Additive manufacturing of Ti-6Al-4V parts through laser metal deposition (LMD): process, microstructure, and mechanical properties. J Alloys Compd 2019;804:163–91. <https://doi.org/10.1016/j.jallcom.2019.04.255>.
- [32] Gorsse S, Hutchinson C, Gouné M, Banerjee R. Additive manufacturing of metals: a brief review of the characteristic microstructures and properties of steels, Ti-6Al-4V and high-entropy alloys. Sci Technol Adv Mater 2017;18:584–610. <https://doi.org/10.1080/14686996.2017.1361305>.

**Paper IV**

**Karimi, J.,** Antonov, M., Kollo, L., & Prashanth, K. G. (2022). Role of laser remelting and heat treatment in mechanical and tribological properties of selective laser melted Ti6Al4V alloy. *Journal of Alloys and Compounds*, 897, 163207.





Contents lists available at ScienceDirect

## Journal of Alloys and Compounds

journal homepage: [www.elsevier.com/locate/jalcom](http://www.elsevier.com/locate/jalcom)

# Role of laser remelting and heat treatment in mechanical and tribological properties of selective laser melted Ti6Al4V alloy

J. Karim<sup>a,b,\*</sup>, M. Antonov<sup>a</sup>, L. Kollo<sup>a</sup>, K.G. Prashanth<sup>a,c,d</sup><sup>a</sup> Department of Mechanical and Industrial Engineering, Tallinn University of Technology, Ehitajate tee 5, 19086 Tallinn, Estonia<sup>b</sup> Department of Mechatronics, Materials Science, Faculty of Engineering Sciences, University of Innsbruck, Technikerstrasse 13, 6020 Innsbruck, Austria<sup>c</sup> Erich Schmid Institute of Materials Science, Austrian Academy of Sciences, Jahnstraße 12, A-8700 Leoben, Austria<sup>d</sup> CBCMT, School of Engineering, Vellore Institute of Technology, Vellore, 632014 Tamil Nadu, India

## ARTICLE INFO

## Article history:

Received 8 November 2021

Received in revised form 7 December 2021

Accepted 8 December 2021

Available online 11 December 2021

## Keywords:

Additive manufacturing

Selective laser melting

Laser remelting

High cycle fatigue

Sliding wear

Ti6Al4V

## ABSTRACT

The reliability and quality of additively manufactured parts are questionable. The present study aimed to improve the surface quality and mechanical and tribological properties of a Ti6Al4V alloy manufactured using selective laser melting (SLM). The effects of the laser remelting on its surface topology, mechanical properties, and sliding wear in a ball-on-plate configuration with a ball either above or below the plate were investigated systematically. The influence of the laser remelting approach on the anisotropy of the mechanical and tribological properties was compared with that of the heat treatment approach. The surface quality and high cycle fatigue strength improved with an increase in the number of melting steps. The compressive and impact strengths also increased with an increase in the number of melting steps. The wear resistance in both configurations was higher in the remelted samples than in the samples after SLM. The results confirmed that laser remelting, as an affordable approach, could significantly improve the reliability of parts fabricated by the SLM process.

© 2021 Elsevier B.V. All rights reserved.

## 1. Introduction

Additive manufacturing (AM) technologies have a wide range of applications in various industries, including the automotive, aerospace, transportation, energy, and medical fields. The selective laser melting (SLM) process is one of the most commonly used AM processes, with the potential to fabricate complex shapes that are impossible to fabricate using traditional manufacturing processes, such as lattice structures [1,2], cellular porous structures (bone scaffolds) [3–5] and metamaterials [6–8], in a layer-wise manner from metallic powders. A wide range of materials can be fabricated using the SLM process, including Ti-, Al-, Ni-, Fe-, Cu-, and Co-based alloys, and high-entropy alloys [9–11].

Ti6Al4V alloys are some of the most widely investigated alloys produced using the SLM process, and have been commonly used in various industries because of their high corrosion resistance, high strength and elastic modulus, and biocompatibility [12]. Despite the progress in the SLM of Ti6Al4V, several challenges remain. The surface roughness of a three-dimensional (3D) fabricated net-shaped

part, which is one of the major challenges in SLM, is relatively high. It was reported to be close to ~12 μm, which is considerably higher than that of machined parts [13]. A significant number of studies have investigated the effects of the scanning strategy, post-processing, building direction, powder particle size, and laser power on the surface topography. Eyzat et al. [14] reported that the application of post-treatment (heat treatment, polishing, sandblasting, and chemical etching) could reduce the roughness. However, post-surface treatments are time-consuming and resource-intensive. Chen et al. [15] reported that the surface topology of parts fabricated using SLM exhibited an orientation dependence, which influenced the mechanical contact properties and mechanical properties. Furthermore, Han et al. [16] stated that the surface roughness improved with the application of laser remelting. However, a comprehensive study of the effects of the melting sequence on the surface topology and roughness in both the transverse cross-section (TCS) and longitudinal cross-section (LCS) of a component fabricated using SLM has yet to be presented in the literature.

Parts fabricated using the SLM process accumulate considerable residual stress as a result of their large thermal gradient and rapid solidification, and layer-by-layer fabrication generates a complicated superposition of stresses and strains. Many studies have reported the effects of SLM process parameters, including the scanning strategy,

\* Corresponding author at: Department of Mechanical and Industrial Engineering, Tallinn University of Technology, Ehitajate tee 5, 19086 Tallinn, Estonia.

E-mail address: [jkarim@taltech.ee](mailto:jkarim@taltech.ee) (J. Karim).



### Nomenclature

LOF	Lack of fusion
MP	Metallurgical pore
TCS	Transverse cross-section
LCS	Longitudinal cross-section
SV	Single melting (vertically fabricated)
DV	Double melting (vertically fabricated)
TV	Triple melting (vertically fabricated)

HT	Heat-treated single melting (vertically fabricated)
MV	Machined single melting (vertically fabricated)
SH	Single melting (horizontally fabricated)
DH	Double melting (horizontally fabricated)
TH	Triple melting (horizontally fabricated)
HH	Heat-treated single melting (horizontally fabricated)
R	Load ratio
$R_a$	Average surface roughness
BD	Building direction

scanning speed, hatch distance, layer thickness, preheating of the platform, support structures, and laser power on the residual stress [11,13–15]. Post-heat treatment can be applied to parts manufactured using SLM to reduce the residual stresses, but it increases the production time and cost. Ali et al. [17] studied the effects of the scanning strategy and remelting (re-scanning) on the residual stress and reported that remelting with a 150% energy density resulted in a 33.6% reduction in residual stress. However, the effects of the melting sequence and post-heat treatment on the residual stresses in both the TCS and LCS must be investigated in detail to complement the existing research on the subject.

The anisotropy of mechanical properties is a major issue facing additive manufacturing technologies such as SLM, with the potential for parts to be influenced by anisotropy in the microstructure, crystallographic texture, and spatial distribution of defects in the build direction. A significant number of studies have investigated the effects of the building orientation on the mechanical properties, including the tensile, compressive, and fatigue strengths. These have reported that parts fabricated in the horizontal orientation exhibited lower strength than those fabricated vertically. However, the effects of the melting sequence on the mechanical properties of parts fabricated horizontally have not yet been studied, although this can improve the mechanical properties and increase the density [18]. Furthermore, the effect of the melting sequence on the compressive behavior of parts has not been studied in detail, but the mechanical properties of parts additively manufactured using SLM show tension–compression asymmetry as a result of discontinuities such as pores [19].

A few studies have investigated the impact strength of a Ti6Al4V part fabricated using SLM, and have reported that it is relatively lower than that of a wrought counterpart because of the presence of a large quantity of pores and oxygen pick-up [20]. Grell et al. [21] studied the effects of the building orientation, hot isostatic pressing (HIP), defects (pores), and powder oxidation on the Charpy impact energy of Ti6Al4V parts fabricated by electron beam melting. However, to the best of our knowledge, no study has systematically and

thoroughly investigated the effects of the melting sequence and building orientation of Ti6Al4V parts fabricated using the SLM process.

The fatigue behavior of Ti6Al4V parts additively manufactured using SLM has been extensively investigated [22–27]. Because of the presence of defects and residual stresses, the SLM parts exhibited poor performance under cyclic loading [28] compared to their wrought counterparts, which limits the application of SLM parts. It has been reported that cracks are mainly initiated as a result of the presence of defects such as lack of fusion (LOF) pores and/or metallurgical pores (MP) [23,24,26]. Thus, post-processing strategies such as heat treatment and hot isostatic pressing (HIP) [23] and laser remelting can be applied to reduce the LOF pores and MP, and consequently improve the fatigue life. Despite the obvious importance of the remelting scan strategy on the mechanical properties of Ti6Al4V alloys [18], the effect of this strategy on the fatigue behavior has not yet been studied in-depth and systematically.

Therefore, the present study considered the effects of laser remelting and heat treatment on the mechanical properties, residual stresses, and surface morphology of SLM Ti6Al4V alloys. The influences of the remelting scan strategy and heat treatment on the surface topology and roughness, high cycle fatigue behavior, tensile/compressive strength, Charpy impact energy, and wear behavior were evaluated and are discussed in detail. In addition, the anisotropy of the surface topography, mechanical properties, residual stress, and mechanical contact properties (wear and coefficient of friction) were investigated in detail, and the results are compared with those for the heat treatment procedure.

## 2. Experimental details

### 2.1. Materials

Fig. 1 depicts scanning electron microscopy (SEM) images of the morphology of gas-atomized Ti6Al4V powder particles, which are spherical in shape, with some satellite particles attached to them.

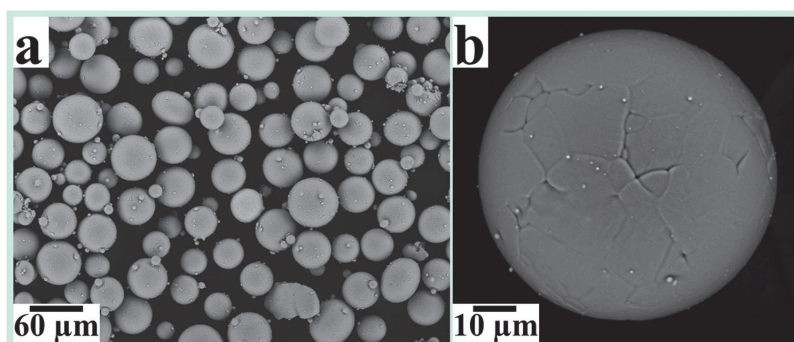


Fig. 1. SEM images of gas atomized Ti6Al4V powder, showing representative view of powder particles in (a), and close-up view of single particle in (b).

**Table 1**  
SLM process parameters used to fabricate Ti6Al4V parts.

Process parameter	
Laser power (W)	60
Laser spot size (mm)	0.039
Laser scan speed (mm/s)	1000
Layer thickness (mm)	0.025
Hatch distance (mm)	0.060
Hatch rotation angle (°)	67
Hatch overlap (mm)	0
Shielding gas	Argon
Shielding gas consumption (l/min)	2–3

The particle size distribution was measured using a laser particle size analyzer (HORIBA LA-950) in deionized water with a diffractive index of 1.72. The powder showed a  $D_{10} \sim 30 \mu\text{m}$  and  $D_{90} \sim 62 \mu\text{m}$ , and the diameter of most particles were equivalent to or below  $\sim 40 \mu\text{m}$  ( $D_{50}$ ).

## 2.2. Sample preparation

The SLM samples were fabricated using a Realizer SLM 50 machine (Realizer GmbH, Germany) equipped with a 120 W Yb-fiber laser with a wavelength of  $1.07 \mu\text{m}$ . Table 1 lists the SLM optimized process parameters used to fabricate the parts. The SLM samples were fabricated with vertical (V) and horizontal (H) building orientations to compare the mechanical properties such as the tensile strength and energy impact. The longest dimensions of the vertically and horizontally fabricated parts were parallel and perpendicular to the building direction (BD), respectively. Each layer of Ti6Al4V powder particles was melted once, twice, or three times using the same process parameters (Fig. 2a). Double and triple melting (scanning) were not performed in a consecutive order, and there was at least a 15 s time interval between the melting steps. The vertically fabricated samples included single melting or as-built SLM (SV), double melting (DV), triple melting (TV), heat-treated single melting (HV), and machined single melting (MV) specimens. The horizontally fabricated samples included single melting (SH), double melting (DH), triple melting (TH), and heat-treated single melting (HH) specimens. The second letter in each label (V or H) represents the vertical or horizontal building orientation, respectively. All of the horizontally fabricated samples were machined to remove the support structures using a turning machine, which was designed to prevent deformation during fabrication. The parts were fabricated under a protective argon atmosphere with a constant flow to avoid contamination.

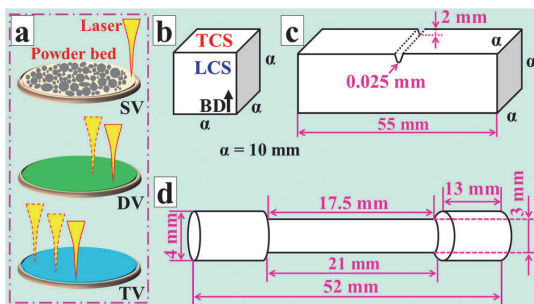


**Fig. 2.** Schematic representation of SLM samples: (a) increasing number of melting steps from one to three (note that SV, DV, and TV stand for single melting, double melting, and triple melting, with time interval of at least 15 s between melting steps), (b) cube with 10 mm dimensions, (c) Charpy test specimen according to ASTM test method E23, (d) tensile bar sample fabricated by SLM according to ASTM standard (E8/E8M-13a).

## 2.3. Post-processing of selective laser melted parts

The as-built SLM samples were heat-treated to study its effects on their mechanical and tribological properties. Based on previous studies on Ti6Al4V alloys [29], the heat treatment of the as-built SLM samples was conducted in a vacuum furnace (R. D. WEBB Co, USA) at  $750^\circ\text{C}$  for 3 h, with a heating rate of  $10^\circ\text{C}/\text{min}$  and furnace cooling. The absolute vacuum was less than  $\sim 1 \times 10^{-1}$  mbar. In addition, the parts fabricated using the SLM process were machined to reduce the surface roughness, with the thread sections of tensile and fatigue test specimens machined using a lathe machine. The horizontally fabricated tensile specimens were machined to remove the support structures.

## 2.4. Surface roughness measurement

The 3D characteristics were analyzed using a 3D optical profiler (BRUKER ContourGT-K0 +; Bruker, Billerica, USA), which included the Vision64 operation and analysis software. The 3D profiler could be moved in the X, Y, and Z planes for sample adjustment. The tabletop 3D profiler was capable of high-resolution ( $1 \mu\text{m}$ ) measurements of the features. The 3D surface profile and roughness ( $R_a$ ) of each sample were analyzed using a vertical scanning interferometry technique. Examinations were made of at least five images of each surface of 10 mm cubes (three cubes for each condition) that were acquired from the SLM samples (Fig. 2b). Subsequently, the surface roughness of each sample was characterized using a diamond stylus instrument (Perthometer Mahr PKG 120, Göttingen, Germany) with an MFW-250  $90^\circ/2 \mu\text{m}$  probe and a Gaussian filter according to ASME B46.1 (DIN 4288). At least three samples were tested with three readings for each dimension. For the longitudinal cross-section (sides) in both measurement methods, the experimental test was carried out parallel and perpendicular to the building direction (BD).

## 2.5. Residual stress measurement

The residual stress measurements of the SLM fabricated parts (Fig. 2b) at the transverse and longitudinal cross-sections of the sample surface were carried out using X-ray diffraction (XRD, Asenware AW-XDM300, HAOYUAN) with a Cu target,  $K\alpha$  radiation (wavelength of  $1.54184 \text{ \AA}$ ), a step size of 0.02, and a time per step of 1 s. The  $\sin^2\psi$  method was used at seven angles ( $\psi$ ), including  $0^\circ$ ,  $15^\circ$ ,  $30^\circ$ ,  $45^\circ$ ,  $-10^\circ$ ,  $-20^\circ$ , and  $-30^\circ$ . Eq. (2.1) was used to calculate the stress in the chosen direction from the inter-planar spacing, as follows:

$$\sigma_\psi = \frac{E}{(1 + \nu) + \sin^2\psi} \left\{ \frac{d_\psi - d_n}{d_n} \right\} \quad (2.1)$$

where  $\sigma_\psi$  is the single stress acting in a chosen direction (MPa),  $E$  is the elastic modulus (GPa),  $\nu$  is Poisson's ratio (-),  $\psi$  is the angle between the normal of the sample and the normal of the diffracting plane ( $^\circ$ ),  $d_\psi$  is the interplanar spacing of planes at an angle  $\psi$  to the surface ( $\text{\AA}$ ), and  $d_n$  is the interplanar spacing of planes normal to the surface ( $\text{\AA}$ ) (for further details, please read [30]).

## 2.6. Microstructural characterization

The structural characteristics of the fabricated parts were analyzed using an X-ray diffractometer (Rigaku SmartLab SE) with a D/teX Ultra 250 1D detector equipped with Cu- $K\alpha$  radiation with a wavelength of  $0.1542 \text{ nm}$ . The measurements were performed at room temperature ( $25 \pm 2^\circ\text{C}$ ) from  $20^\circ$  to  $120^\circ$  ( $2\theta$ ) using  $0.04^\circ$  steps, with 5 s per step. The fabricated parts were cross-sectioned, mounted, and polished. Then, the samples were etched using Kroll's reagent, which consisted of 5 ml of  $\text{HNO}_3$  (nitric acid), 3 ml of HF

(hydrofluoric acid), and 100 ml of distilled water. A microstructural characterization and fracture surface analysis were conducted using a tabletop scanning electron microscope (Hitachi TM1000, Tokyo, Japan). The wear zones of the samples were observed using SEM with high (cleaned samples) and low (with wear debris) vacuum modes. X-ray fluorescence (XRF) spectrometry (Rigaku Primus II) was used to determine the chemical composition of the elements.

### 2.7. Mechanical characterization and density measurements

Room-temperature tensile tests were carried out on a servo-hydraulic testing machine (Instron 8516, High Wycombe, UK) with a capacity of 100 kN. The strain rate of the tensile tests was set to 0.001 mm/s. The tensile bars were fabricated according to ASTM E8/E8M-13a. The dimensions of the tensile bars were modified to suit a length of 52 mm, as per the ratio mentioned in the ASTM standard (Fig. 2d). At least three samples were tested under each condition to evaluate the reproducibility of the results, and representative tensile curves are presented where necessary. The post-processing procedures (heat treatment and machining) of the tensile bars were described in Section 2.3. The compression test was carried out at room temperature (and a relative humidity of 58%) using a servo-hydraulic machine (Instron 8516, High Wycombe, UK) with a strain rate of 1 mm/min. Vickers microhardness tests were conducted using a Micromet 2001 (Buehler) machine with a 200 g load and 10 s dwell time. The average microhardness values were obtained from three samples, with at least 12 measurements for each sample. The Charpy test specimens were fabricated using the SLM process parameters described in Section 2.2, as shown in Fig. 2c. The room-temperature Charpy impact tests were conducted with a Pendulum impact tester (RKP 450, Zwick, Germany) using standard V-notch specimens (10 × 10 × 55 mm) in accordance with ASTM test method E23. The average Charpy absorbed impact energy values were obtained from at least three samples for each condition. Both the horizontally and vertically oriented specimens were polished to remove the support structure. The density of the fabricated SLM samples was measured using an analytical balance (Mettler Toledo ME204) with a precision of ± 0.0001 g, based on Archimedes' principle. The fatigue specimens (Fig. 2d) were fabricated using the optimized SLM process parameters described in Section 2.2. High-cycle fatigue tests were carried out on a universal fatigue tester (Instron 8516, High Wycombe, UK) with a Track8800D controller at room temperature, a frequency of 5 Hz, a stress ratio of  $R = -1$ , and under a sinusoidal loading at different stress ranges from 100 to 700 MPa at narrower intervals of 50 MPa. The fatigue test was stopped when failure occurred or when the sample survived at least one million cycles. Fractography investigations of the samples were conducted to determine the fatigue crack initiation source on at least three samples.

### 2.8. Tribological characterization

The tribological properties were investigated using a tribotester (CETR/Bruker UMT-2) under a dry reciprocating sliding condition, a frequency of 5 Hz, an amplitude of 1 mm, and a load of 0.3 N (~30.6 g). The test consisted of five steps of 1000 s each in air at room temperature (25 ± 2 °C), with a relative humidity (RH) of 45 ± 5%. The reciprocating sliding tests were carried out on at least three samples with grade 10 zirconia balls (zirconium oxide, ZrO<sub>2</sub>) with a diameter of Ø3 mm, which were fabricated by RGP BALLS (Cinisello Balsamo, Italy). The volume of the material loss (missing net volume) was determined using a 3D profiler (Bruker ContourGT-K0+; Bruker, Billerica, USA). To study the effect of the ball position on the tribological properties, two ball positions were investigated: the ball-above and ball-below positions. In the ball-above position, the ball was located above the sample, which is a typical position used in reciprocating sliding (standard configuration). In the ball-below

position, the ball was located below the sample, and the generated wear debris could easily escape from the wear zone as a result of gravity and could consequently affect the tribological properties. This information must be considered during the design of SLM Ti6Al4V parts used in different applications.

## 3. Results

### 3.1. Surface characteristics

The surface topography and average surface roughness ( $R_a$ ) values of the SV, DV, TV, and HV samples in the TCS and LCS obtained using the 3D optical (non-contact surface profile) and stylus (contact roughness meter) profilers are shown in Fig. 3a–i. The 3D topographies of the SV in both the TCS and LCS showed a rough surface associated with a relatively large number of balling defects (individual melt beads) and the adhesion of partially molten particles. While the DV and TV samples exhibited fewer balling defects and less adhesion of partially molten particles in the LCS, the TCS surfaces showed peaks at the center of the laser tracks with an average distance of ~60 µm (approximately equal to the hatch distance). However, the heat-treated sample showed lower balling defects and less adhesion of partially molten particles on both the TCS and LCS. It can be seen that the surface topographies of the samples depended on the number of melting steps and the heat treatment. Accordingly, the  $R_a$  values of the SLM samples, as a function of the melting sequence and heat treatment, were measured for both the TCS and LCS and compared, as shown in Fig. 3i. It can be seen that the  $R_a$  values for both the TCS and LCS decreased slightly with an increase in the number of melting steps from SV to TV. However, the surface roughness values of all the SLM samples were orders of magnitude higher than those of their cast Ti6Al4V counterparts [31], which could affect their tribological and mechanical properties. In addition, the heat-treated sample (HV) exhibited a reduction in  $R_a$  for both the TCS and LCS surfaces in comparison with the SV, in agreement with the findings of Majeed et al. [32]. It is worth mentioning that the  $R_a$  value obtained from the stylus was higher than the value obtained from the 3D profiler in both the TCS and LCS because of the different measurement techniques. Nevertheless, the stylus profiler provided information for a significantly larger zone than the 3D profiler.

### 3.2. Mechanical properties and residual stresses

Fig. 4a shows the tensile stress–strain curves for the vertically oriented specimens, including the SV, MV, and HV samples. The mechanical properties obtained from room-temperature tensile tests are summarized in Table 2. The tensile strength properties of DV and TV specimens have been discussed in detail elsewhere [18]. There was no significant difference in the tensile strength properties of the SV and MV specimens, with both samples exhibiting similar values for the ultimate tensile strength (UTS) and yield stress (YS). On the other hand, the HV sample showed a decrease of ~11% in the UTS and YS, but a 3-fold increase in the ductility compared to the SV and MV samples. In addition, the stress–strain curves for the horizontally oriented specimens, including the SH, DH, TH, and HH samples, are illustrated in Fig. 4e. The experimental results obtained from the room-temperature tensile tests for the horizontally oriented specimens are summarized in Table 2. It can be seen that the UTS, YS, and ductility decreased with an increase in the melting sequence from SH to TH. Moreover, the HH sample fabricated with a horizontal building orientation exhibited the lowest UTS among the samples, while it exhibited a significant increase in elongation (from ~2.7% for SH to ~5% for HH). The heat treatment procedure transformed the metastable acicular  $\alpha$  martensite microstructure into a biphasic  $\alpha + \beta$  matrix, which significantly improved the ductility, as reported by Facchini et al. [33].

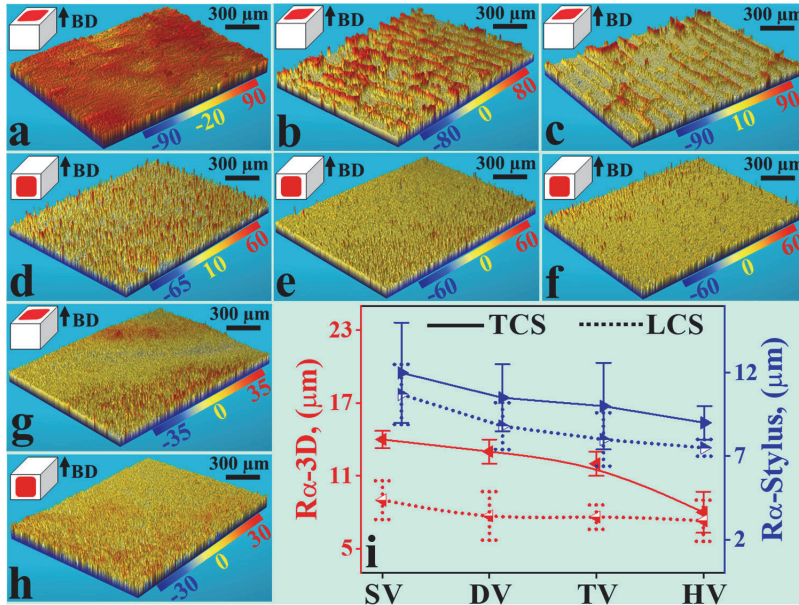


**Fig. 3.** Surface morphologies of TCS and LCS surfaces of fabricated parts: (a) and (d) SV; (b) and (e) DV; (c) and (f) TV; and (g) and (h) HV (note that arrow shows building direction (BD)); (i)  $R\alpha$  (roughness) values for LCS and TCS of samples obtained from 3D optical and stylus profilers (note that solid and dotted lines show roughness values for TCS and LCS surfaces, respectively).

The selected tensile fracture surfaces of the specimens fabricated using vertical and horizontal building orientations are shown in Fig. 4b–d and Fig. 4f–i, respectively. The SV and MV samples showed a layered fracture, dimples, and voids, indicating a quasi-cleavage

fracture. However, the fracture surface of the HV sample exhibited shallow and small dimples and voids, suggesting a ductile fracture. In addition, the fracture surface of the horizontally oriented SLM parts, including the SH, DH, and TH samples, presented cleavage and

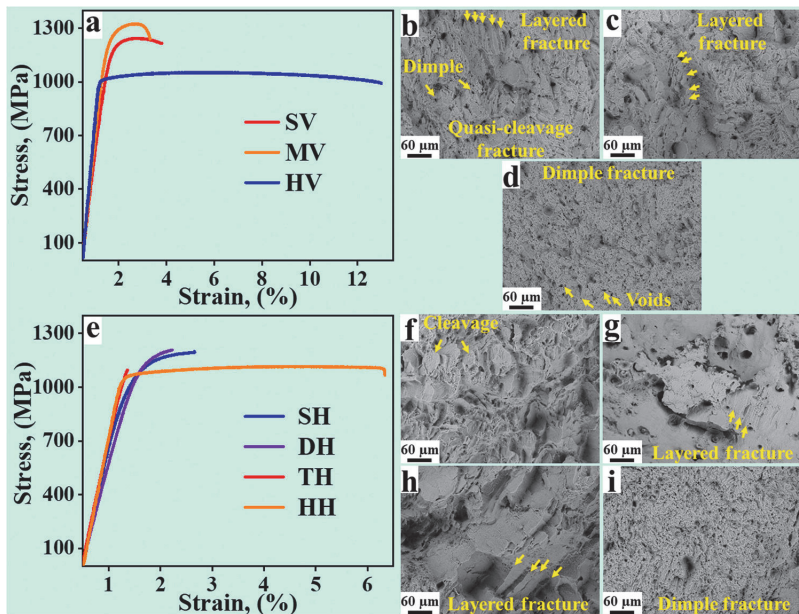


**Fig. 4.** (a) Experimental results of room-temperature tensile stress–strain tests of vertically fabricated specimens, including SV, MV, and HV specimens. SEM images of tensile fracture: (b) SV, (c) MV, and (d) HV specimens. (e) Stress–strain curves of horizontally fabricated specimens, including SH, DH, TH, and HH samples. SEM images of tensile fracture: (f) SH, (g) DH, (h) TH, and (i) HH samples.

**Table 2**  
Mechanical properties of tested specimens in tension (YS = yield strength, UTS = ultimate tensile strength, A = elongation, and E = Young's modulus).

	Vertically oriented specimens			Horizontally oriented specimens			
	SV	MV	HV	SH	DH	TH	HH
UTS, MPa	1208 ± 66	1198 ± 80	1043 ± 13	1155 ± 112	1133 ± 42	1063 ± 45	1047 ± 10
YS, MPa	1103 ± 32	1108 ± 43	1012 ± 4	1051 ± 40	1143 ± 41	997 ± 118	1008 ± 20
A, %	3.3 ± 0.0	2.81 ± 0.4	11.3 ± 1.7	2.7 ± 1.0	1.28 ± 0.4	0.8 ± 0.0	4.9 ± 1.4
E, GPa	123 ± 6	145 ± 25	147 ± 11	128 ± 26	127 ± 13	136 ± 6	147 ± 9

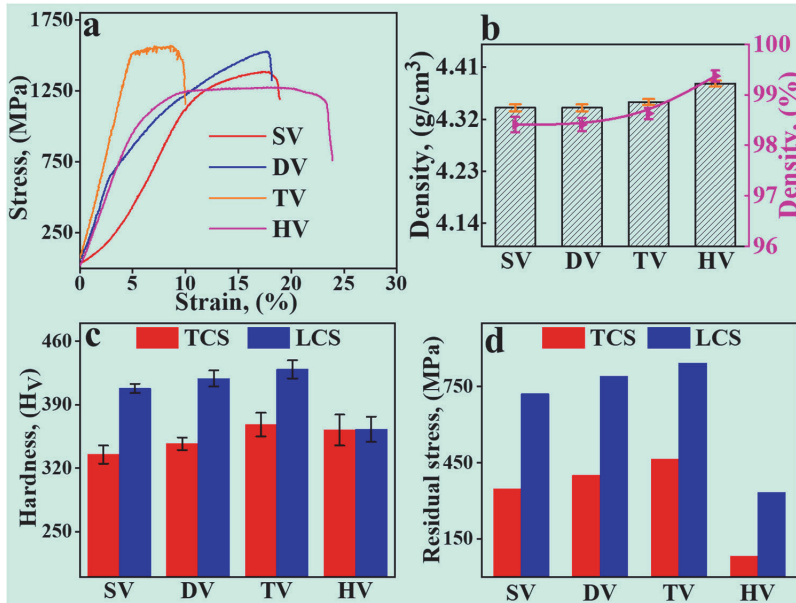


**Fig. 5.** (a) Compressive stress–strain curves of SLM and heat-treated samples obtained at room-temperature. (b) Average Archimedes densities of SLM and heat-treated samples. (c) Vickers hardness values of TCS and LCS of SLM and heat-treated samples. (d) Residual stress values of SLM and heat-treated samples.

layered fractures, indicating brittle fractures. Similar to the HV specimen, the HH specimen exhibited shallow and small dimples, suggesting a ductile fracture.

Compressive tests were carried out on the SV, DV, TV, and HV specimens to evaluate the effects of intrinsic defects (such as porosity and cracks) on the mechanical properties because these exhibited brittle fracture under tensile testing. The experimental compressive response curves of the SV, DV, TV, and HV specimens are presented in Fig. 5a. The mechanical properties, including the UCS, YCS, and fracture strain ( $\epsilon$ ), obtained from the room-temperature compression tests of the samples are presented in Table 3. It can be seen that the melting sequence improved the UCS and YCS from SV to TV, but it caused a significant decrease in ductility. In addition, the heat treatment process had a very pronounced effect on the

**Table 3**  
Compression property, hardness, and residual stress (RS) values of SLM and heat-treated samples.

Compressive property	Sample			
	SV	DV	TV	HV
UCS, MPa	1423 ± 159	1544 ± 23	1613 ± 62	1383 ± 39
YCS, MPa	1109 ± 96	1149 ± 86	1162 ± 92	805 ± 38
$\epsilon$ , (%)	23 ± 3	21 ± 3	15 ± 6	26 ± 0.5
Hardness-TCS ( $H_{vT}$ )	335 ± 10	347 ± 7	368 ± 13	362 ± 14
Hardness-LCS ( $H_{vL}$ )	408 ± 5	419 ± 9	429 ± 10	363 ± 17
RS-TCS (MPa)	348	400	465	81
RS-LCS (MPa)	722	790	843	333

compressive behavior of the sample, with this post-treatment process causing a substantial improvement in the ductility of the as-built SLM specimen, as shown in the results presented in Fig. 5a and Table 3. However, the HV sample exhibited a decrease in compressive strength compared to that of the SV sample.

The average Vickers hardness values of the LCS and TCS of the SLM and heat-treated samples are shown in Fig. 5c, where the hardness increases with an increase in the number of melting steps from the SV to the TV (Table 3). The hardness of the HV samples showed a significant reduction in the anisotropy of the hardness observed in the SLM samples. Fig. 5d shows the RS values of the SLM and heat-treated samples at the TCS and LCS surfaces. The RS values at both the TCS and LCS surfaces increased with an increase in the number of melting steps from the SV to the TV (Table 3). However, the HV sample showed reductions in RS for both the TCS and LCS. Because of the directional heat distribution in the SLM process, an anisotropy in the residual stress distribution of the parts could be created, with the residual stress value in the TCS lower than that in the LCS (Fig. 5d). Anisotropy in the residual stress could cause anisotropy in the mechanical properties and plastic deformation [34]. In addition, the average Archimedes density was observed to be ~98.6% for the as-built SLM and remelted samples, and 99.4% for the heat-treated sample (Fig. 5b). In a rapid solidification process such as SLM, there is not sufficient time available for the conductive homogenization of the input energy, and subsequently the heat distribution in the powder bed, which may lead to pore formation.

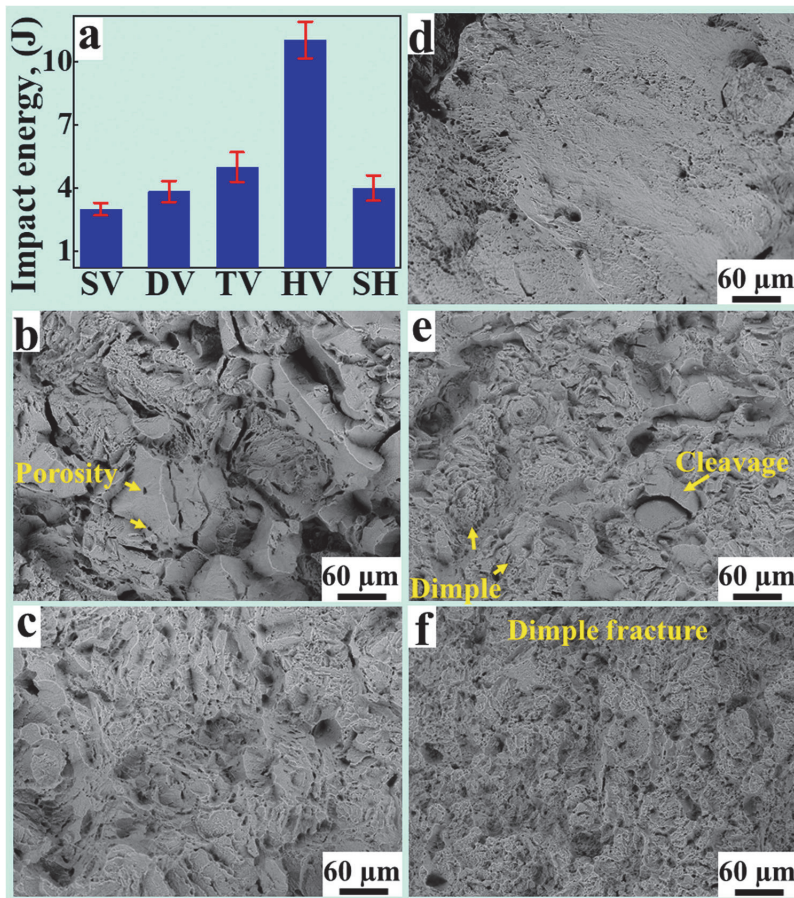


**Fig. 6.** (a) Absorbed energy values obtained from Charpy V-notch tests, and SEM fractographs of Charpy impact test results: (b) SV, (c) DV, (d) TV, (e) SH, and (f) HV (note that Charpy impact energy values for DV and TH are not presented because of deformations in test specimens during fabrication process).

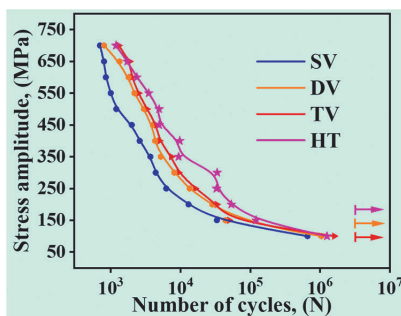


**Fig. 7.** S-N curves of SLM samples as function of melting sequence and heat treatment process. The arrows indicate the runout of the specimens. Note that the HCF behavior of horizontally oriented specimens is not presented because of deformations in the fabricated parts and failure at a very low number of cycles (N).

The Charpy impact test was carried out to determine the influences of the laser remelting, heat treatment, microstructure, defects (porosity), and building orientation on the capacity of the parts fabricated using SLM to absorb energy before failure. Fig. 6a shows

the average Charpy absorbed impact energy and its deviation in the vertically oriented specimens, including the SV, DV, TV, and HV specimens, along with the horizontally oriented specimens (SH). It can be observed that as the number of melting steps increased from single melting to triple melting, the Charpy absorbed impact energy increased. The SH sample showed a higher impact energy than the SV sample, indicating the anisotropy of the Charpy absorbed impact energy. Moreover, the heat-treated sample exhibited a significant increase in the Charpy absorbed impact energy (11 J) compared to the SV sample. However, the impact energy values in both building directions were lower than those of the cast counterpart [35]. In addition, the fractographic analysis results for the Charpy impact test of the samples is displayed in Fig. 6b–f. The fracture surfaces of the SV and SH samples (Fig. 6b and e, respectively) showed quasi-cleavage and micro-voids. Compared to the SV sample, the DV and TV samples exhibited smooth fracture surfaces, indicating less ductile fracture. Nevertheless, the heat-treated sample (Fig. 6f) exhibited the presence of shallow and small dimples on the surface, suggesting that the fracture was ductile.

Fig. 7 depicts the room-temperature high-cycle fatigue (HCF) testing results for the SLM specimens as a function of the melting sequence and heat-treatment. The runout specimens (i.e., the HCF test specimens that survived a stress amplitude of 100 MPa up to 10<sup>6</sup>

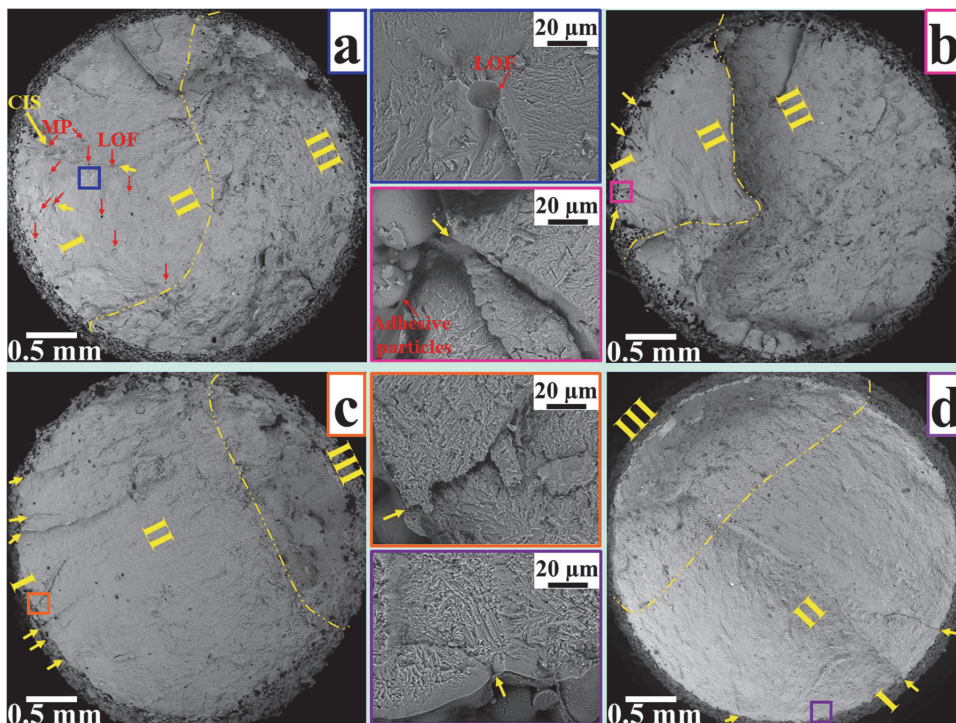


**Fig. 8.** SEM images of HCF fracture surfaces under stress amplitude of 150 MPa: (a) SV, (b) DV, (c) TV, and (d) HV. The magnified SEM images show the HCF crack initiation sources, which are marked with rectangles in the overall view of fracture surfaces. The yellow arrows indicate the CIS. (For interpretation of the references to color in this figure legend, the reader is referred to the web version of this article.)

cycles) are marked with arrows. The MV (machined SLM) samples exhibited HCF behaviors similar to the SV samples, with statistically negligible differences. This is probably why in the HCF tests, cracks typically initiated at the subsurface discontinuities (such as LOF pores, MP, and cracks) of the SLM specimens, in agreement with [36]. Hence, the HCF results of the MV samples are not included. The HCF strength of the fabricated specimens improved with an increase in the number of melting steps, with the TV samples exhibiting the best HCF performances, indicating an endurance limit of ~100 MPa at  $10^6$  cycles. On the other hand, the HCF failure of the SV samples occurred at a lower number of cycles (compared to the endurance limit of the TV sample). It has been reported that the HCF endurance limit of parts fabricated using SLM is considerably lower than that of their wrought counterparts [25], which could be due to the defects and/or residual stresses associated with the SLM process. However, the HCF strengths of the heat-treated samples were significantly better than those of the SV samples (Fig. 7). This was in agreement with the results of Gunther et al. [23] and Fotovvati et al. [25], who reported that post-processing treatment significantly improved the HCF behavior of SLM Ti6Al4V under cyclic loading. Appendix presents the number of cycles to failure/runout in a tabular format for each sample.

Fig. 8 illustrates the selected fracture surfaces of the HCF specimens of the remelted and heat-treated samples, indicating multiple HCF crack initiation sites. The fracture surfaces of the specimens contained three regions, including the crack initiation site (CIS, I), crack propagation area (II), and final fracture (III), with the crack growth area found in the HCF tests shown. It can be seen from Fig. 8a that the LOF pores and MP exist in region I of the SV sample. The existence of LOF pores and MP resulted in a stress concentration, in

which they acted as the main part of the HCF crack initiation site. It has been proven that the HCF life is notably influenced by the surface roughness in wrought and cast counterparts [24], while discontinuities play the dominant role in determining the HCF behavior in as-built SLM parts, because a large number of studies have shown that discontinuities can decrease the HCF strength [22]. On the other hand, the cracks in the remelted and heat-treated samples were initiated from the surface, as highlighted in Fig. 8b–c and their magnified images.

### 3.3. Phase identification and chemical composition

The XRD patterns of both the TCS and LCS surfaces are illustrated in Fig. 9, which show the presence of the  $\alpha/\alpha'$  phase in the as-built and remelted SLM samples. It is worth mentioning that the  $\alpha$  and  $\alpha'$  phases had hexagonal closed-packed (HCP) structures and similar lattice parameters ( $a$  and  $c$  were ~0.295 and ~0.461 nm, respectively), in agreement with Xie et al. [37]. The HV specimen had a biphasic  $\alpha + \beta$  microstructure in both the TCS and LCS as a result of the heat treatment, which was also noted by Li et al. [29]. In addition, the chemical compositions of the SLM specimens as a function of the melting sequence and heat treatment process for both the TCS and LCS surfaces are given in Table 4. It can be seen that these did not change with the remelting and heat treatment.

### 3.4. Tribological properties

Tribological tests with different configurations (ball above and ball below) were conducted to evaluate the wear resistance and coefficient of friction (COF) values of the SLM specimens as a

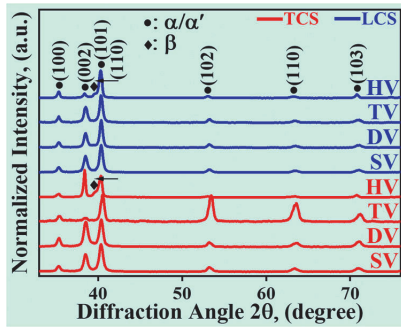


**Fig. 9.** XRD results for TCS and LCS of SLM processed samples with melting sequence and heat treatment. Note that the heat-treated sample exhibits a biphasic ( $\alpha + \beta$ ) microstructure.

**Table 4**  
Chemical composition (wt%) of SLM Ti6Al4V samples.

	Concentration, wt%			
	Al	V	Fe	Ti
SV-TCS	6.2	3.3	0.2	Balance
SV-LCS	6.1	3.3	0.2	Balance
DV-TCS	6.2	3.2	0.1	Balance
DV-LCS	5.7	3.2	0.2	Balance
TV-TCS	5.7	3.3	0.1	Balance
TV-LCS	5.8	3.1	0.2	Balance
HV-TCS	6.6	3.3	0.2	Balance
HV-LCS	6.2	3.3	0.2	Balance

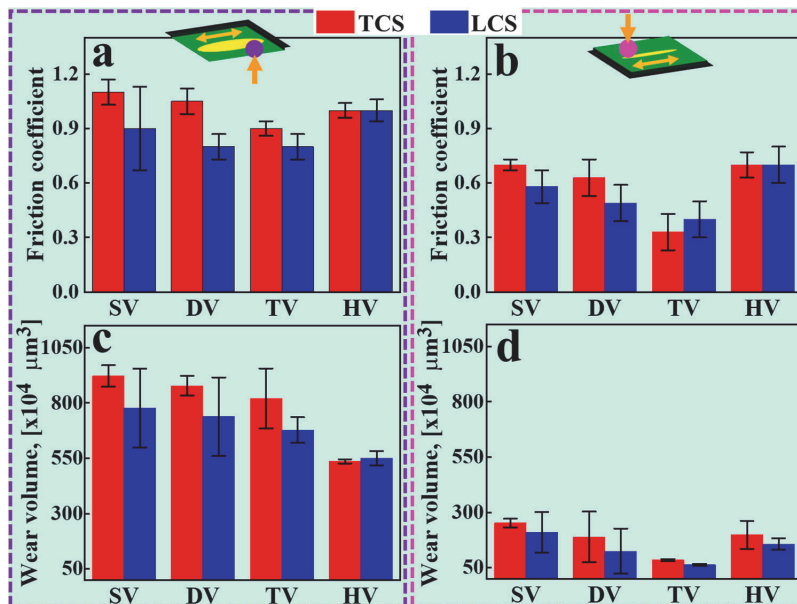
function of the melting sequence and heat treatment at different contact positions. The effects of the melting sequence and heat treatment process on the CoF under the ball-below and ball-above

conditions are summarized in Fig. 10a and b, respectively. It can be seen that the CoF values for both the TCS and LCS decreased with an increase in the number of melting steps, from SV to TV, under both conditions. In addition, the average wear volumes under the ball-below and ball-above conditions are shown in Fig. 10c and d, respectively. The average wear volume (under the ball-below and ball-above conditions) decreased with an increase in the number of melting steps from SV to TV for both the TCS and LCS surfaces. It can be seen that the as-built and remelted SLM samples exhibited anisotropy in the average wear volume and CoF. On the other hand, the heat-treated samples exhibited isotropic wear and friction behaviors. Moreover, depending on the ball position, the samples showed a significant difference in the average wear volume and CoF values, with the values obtained under the ball-below condition being greater than those under the ball-above condition for both the TCS and LCS surfaces.

#### 4. Discussion

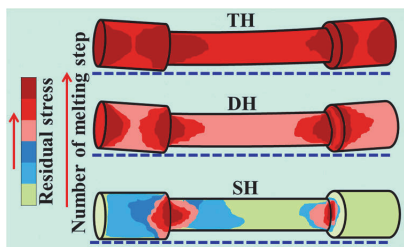
##### 4.1. Surface topology

Fig. 3 depicts the surface topographies of the SLM and heat-treated samples, where the surface topographical features, including the balling, adhesion of partially molten particles, porosities, and overlap of adjacent laser tracks are observed. In SLM, balling occurs mainly because the high surface tension of the molten material prevents it from wetting the substrate, and its formation can be affected by the building orientation, powder particle size, and SLM process parameters (laser parameters, layer thickness, scan speed, oxygen content, etc.) [38,39]. During the remelting, the laser melts the already solidified layer, but the width of the melt pool is smaller than that during the original SLM [18]. The remelted samples (DV and TV) showed better surface finishes because of the melting of the (metal) balls and adhered powder particles, which consequently reduced the surface roughness, in agreement with Li et al. [39]. This clearly demonstrated that one of the ways to control the surface



**Fig. 10.** CoF values for both TCS and LCS surfaces of SLM and heat-treated samples at different contact positions: (a) ball below, and (b) ball above. Average wear volumes for both TCS and LCS surfaces of SLM and heat-treated samples at different contact positions: (c) ball below, and (d) ball above.





**Fig. 11.** Schematic illustration of effect of number of melting steps on horizontally oriented specimens. Note that the deformations in the schematics of the DH and TH samples are exaggerated to make them more visible.

finish of parts fabricated by the SLM process is remelting, which can save money and time. Although the application of heat treatment reduced the roughness, it increased the total production time and cost. In addition, an anisotropic surface roughness in the samples fabricated by SLM was observed, where the surface roughness values obtained from both methods (optical and stylus) for the TCS surface were greater than those for the LCS surface. The anisotropic surface roughness of the SLM samples could affect their contact mechanical properties (wear and friction), mechanical properties (fatigue and strength), and the dimensions of fabricated parts.

#### 4.2. Mechanical properties

A schematic representation of the effect of remelting on the residual stress is shown in Fig. 11. As indicated in Fig. 4e, the UTS and ductility of the horizontally fabricated samples decreased with an increase in the number of melting steps from single melting to triple melting, which was probably due to the increases in the residual stresses (Fig. 5d) and deformation. In the SLM process with a small melt pool size ( $\sim 100 \mu\text{m}$ ), large thermal gradient, and very short (microsecond) laser-material interaction duration, when the laser beam melts the material, the melted and partially melted material expands, and this zone is restrained by the solidified material. After the laser beam moves away from the molten material, the small melt pool rapidly solidifies (which causes tensile stress), and consequently, residual stresses are produced in the solidified and adjacent metals. During layer-by-layer manufacturing using the SLM process, this mechanism occurs at each step (layer). Therefore, large residual stresses are generated in the fabricated parts, which influence the mechanical properties (strength, fatigue, hardness, etc.) and cause microcracks and plastic deformation [12]. On the other hand, in the remelted samples, because of the higher thermal conductivity of the bulk material and smaller melt pool size compared to the loose powder, and consequently the higher cooling rate (compared to the as-fabricated SLM specimens), the residual stresses in both the TCS and LCS increase (Fig. 5d), which can cause plastic deformation and reduce the tensile strength (Fig. 4e).

The Ti6Al4V samples fabricated using SLM exhibited a significant anisotropy in their mechanical properties, where the SH samples exhibited lower UTS, YS, and ductility values than the SV samples, which was ascribed to the intrinsic anisotropy in the properties of the parts fabricated by the SLM process due to columnar grain growth along the building direction. Furthermore, the horizontally oriented specimens that were laser remelted exhibited lower UTS, YS, and ductility values than those fabricated vertically [18], probably because of plastic deformation. Moreover, it is worth mentioning that no significant asymmetry in the strength behavior under tensile and compressive stresses (strength differential (SD) effect) was observed.

The results obtained from the Charpy tests suggested that the laser remelting improved the impact energy. Hrabe et al. [40]

studied the effect of porosity on the Charpy absorbed energy values of additively manufactured Ti6Al4V parts using electron beam melting (EBM). They reported that porosity had a deleterious influence on the impact energy. In our previous work [18], we investigated the effect of laser remelting on the quantity of LOF pores. We concluded that by increasing the number of melting steps from single melting to triple melting, the LOF pores were reduced. Furthermore, fractography showed pores on the fracture surfaces of the HV samples. Moreover, the Charpy absorbed energy of the HV samples was found to be higher than that of SV samples because of the presence of a biphasic ( $\alpha + \beta$ ) microstructure and consequently higher ductility. In addition, the porosities (mainly the LOF pores) were reduced by the application of the heat treatment process because of the strong bonding between the powder particles [41]. Subsequently, the Charpy absorbed energy increased significantly with the post-heat treatment procedure.

SLM parts usually exhibit a much lower (over 75% [25]) HCF life compared to their wrought counterparts, mainly as a result of the presence of discontinuities such as pores (LOF pores and MP), which may act as nuclei for cracks. LOF pores, which refer to zones of non-processed powder particles, are irregular in shape and large in size because of the insufficient consolidation of the powder particles. LOF pores are the main factor in the irregularity of the HCF, and can initiate cracks as a result of the induced stress and accumulated plastic strain [42], which may deteriorate the HCF behavior. A large number of studies have clearly proven that with the application of laser remelting, the number of LOF pores decreases, which leads to a higher density [18,43–45]. The effect of remelting on the surface porosity is also shown in Appendix. As mentioned in Section 3.2, the remelted samples, particularly the TV samples, showed an improvement in the HCF life as a result of a significant reduction in the number of LOF pores. It should be noted that the location of the discontinuities (LOF pores and MP) plays a major role in the fatigue behavior of AM Ti6Al4V [23]. However, further research is needed to reveal the influence of the locations of LOF pores and MP in SLM specimens as a function of the melting sequence and heat-treatment, which will be vital to advance an understating of the HCF behavior.

#### 4.3. Tribological properties

As discussed in Section 3.4, lower wear volumes were observed in the remelted samples compared to the as-built SLM samples (SV), with decreases of  $\sim 12\%$  under the ball-below condition and  $\sim 70\%$  under the ball-above condition with an increase in the number of melting steps from SV to TV. The higher wear volume of the SV samples compared to the DV and TV samples could be explained according to Archard's linear law, in which it is inversely proportional to the hardness value of the material, as shown in Eq. (4.1) [46]:

$$V = \frac{kFS}{3H} \quad (4.1)$$

where  $V$  is the total volume loss ( $\text{m}^3$ ),  $H$  is the hardness of the softest contacting surfaces (Pa),  $F$  is the total applied load (N),  $S$  is the sliding distance (m), and  $k$  is the abrasive coefficient (dimensionless constant). Although hardness plays a crucial role in the volumetric loss of the worn material, there are several other important factors that also influence the wear behavior of materials, such as the microstructure, mechanical properties (ductility and UTS), and physical properties (density and thermal properties). As observed in Section 3.3, the SV, DV, and TV samples showed the presence of the  $\alpha/\alpha'$  phase. On the other hand, the HV samples showed the presence of a biphasic ( $\alpha + \beta$ ) microstructure. The microstructures of the SV, DV, TV, and HV samples for both the TCS and LCS are shown in the appendix, which corroborate the XRD results. The wear volume was

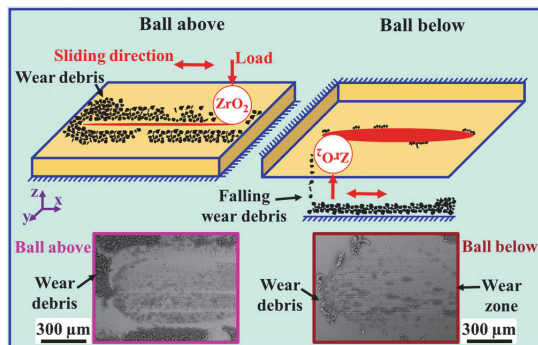


**Fig. 12.** Schematic representation showing behaviors of debris under ball-above and ball-below conditions. SEM images show wear tracks under ball-above and ball-below conditions. Note that the SEM images depict the worn material of the SV sample in the LCS.

reduced by ~23% under the ball-above condition and ~35% under the ball-below condition with heat treatment, which was due to the microstructure evolution of the as-built SLM specimen. In addition, it should be noted that residual stresses could have also influenced the wear volume, with the wear volume decreasing with the residual stress, in agreement with Wang [47]. Moreover, the density of the parts fabricated by SLM affected the hardness of the material. Subsequently, it influenced the wear behavior, where an increase in the density of the parts (Fig. 5b) could have improved the wear performance. Gu et al. [48] reported that fully densified SLM samples exhibited improved wear behaviors.

A schematic representation of the effects of the ball-below and ball-above positions on the wear behaviors of the SLM samples is shown in Fig. 12. The wear volume and CoF values of the parts fabricated by SLM under the ball-below condition were significantly higher than those under the ball-above condition. During the rubbing of the surfaces, wear particles or debris formed as a result of the friction forces between the surfaces, which played an important role in the wear behavior, depending on the mechanical and chemical properties of the moving surfaces. Under the ball-above condition, the wear particles or debris agglomerated around the worn surfaces. On the other hand, the debris produced under the ball-below condition could easily fall off of the worn surfaces as a result of the force of gravity. However, some wear debris remained in the friction area under both ball configurations, and could influence the wear behavior because it acted as load-bearing areas. The SEM micrographs in Fig. 12 depict the ball-below and ball-above conditions in order to compare the effects of the ball position, where a large amount of wear particles are observed around the wear zone. The higher wear rate and CoF under the ball-above condition compared to the ball-below condition were probably due to the formation of a protective tribolayer consisting of compacted wear debris. Hence, the effect and behavior of wear debris should be considered in the design and application of additively manufactured Ti6Al4V parts because they significantly influence the mechanical contact properties.

## 5. Conclusion

In this study, the effects of laser remelting and heat treatment on the mechanical and tribological properties of SLM Ti6Al4V alloy specimens were investigated. Additionally, the effects of remelting and heat treatment on the anisotropy of the surface quality, residual stress, and mechanical and tribological properties were investigated. The following conclusions were drawn.

1. The wear volume and CoF values in the ball-above configuration were significantly lower than those in the ball-below configuration because of the formation of a protective tribolayer consisting of compacted wear debris. The wear debris significantly influenced the mechanical contact properties, and their impact on the design and application of SLM Ti6Al4V parts should be considered. Moreover, the melting sequence decreased the wear volume and CoF values for both the TCS and LCS. However, anisotropy was found for the wear volume and CoF between the TCS and LCS surfaces. Nevertheless, the heat treatment procedure reduced this anisotropy in the wear volume and CoF.
2. Increasing the number of melting steps from single melting to triple melting resulted in an improvement in the HCF strength. Discontinuities (LOF pores and MP) acted as nuclei for crack formation in the SV samples, whereas cracks were mainly initiated from the surface in the DV, TV, and HV samples. The HV value indicated that the HCF strength improved significantly compared to the SV sample, which could have been due to the reduction in the residual stress. In addition, the Charpy absorbed impact energy of the fabricated parts increased with an increase in the number of melting steps from single melting to triple melting. The HV sample exhibited a significant increase in the Charpy absorbed impact energy compared to the SV sample because of the presence of a biphasic ( $\alpha + \beta$ ) microstructure and consequently higher ductility.
3. The parts fabricated using SLM exhibited significant anisotropy in their tensile and compressive strength, hardness, and residual stress values as a function of the melting sequence. The melting sequence reduced the UTS and ductility of the horizontally fabricated samples, which was attributed to the increase in residual stresses. However, post heat treatment not only reduced the anisotropy and residual stress, but also considerably improved the ductility. Furthermore, no significant asymmetry was observed in the strength behavior under tensile and compressive stresses.
4. Anisotropy was observed in the surface topology and high surface roughness (obtained from the 3D profiler and stylus). Laser remelting decreased the surface roughness and anisotropy in the surface topology for both the TCS and LCS as a result of the melting of the metal balls and adhered powder particles. Heat treatment procedures also reduced the anisotropy of the surface topology and surface roughness.

## CRediT authorship contribution statement

**Javad Karimi:** Conceptualization, Data curation, Formal analysis, Investigation, Methodology, Writing – original draft. **Maksim Antonov:** Conceptualization, Formal analysis, Investigation, Writing – review & editing. **Lauri Kollo:** Supervision, Writing – review & editing. **Prashanth Konda Gokuldoss:** Supervision, Writing – review & editing.

## Declaration of Competing Interest

The authors declare that they have no known competing financial interests or personal relationships that could have appeared to influence the work reported in this paper.

## Acknowledgements

The authors would like to thank Mr. Rainer Traksmas for his technical assistance. The authors would like to thank Drs Mart Saarna and Priidu Peetsalu for their assistance and valuable suggestions. This work has been partially supported by ASTRA “TUT Institutional Development Programme for 2016–2022” Graduate

school of Functional Materials and Technologies (2014-2020.4.01.16-0032).

**Appendix A. Supporting information**

Supplementary data associated with this article can be found in the online version at doi:10.1016/j.jallcom.2021.163207.

**References**

[1] T. Maconachie, M. Leary, B. Lozanovski, X. Zhang, M. Qian, O. Faruque, M. Brandt, SLM lattice structures: properties, performance, applications and challenges, *Mater. Des.* 183 (2019) 108137, <https://doi.org/10.1016/j.matdes.2019.108137>

[2] G. Wang, X. Chen, C. Qiu, On the macro- and micro-deformation mechanisms of selectively laser melted damage tolerant metallic lattice structures, *J. Alloy. Compd.* 852 (2021) 156985, <https://doi.org/10.1016/j.jallcom.2020.156985>

[3] L. Zhang, B. Song, L. Yang, Y. Shi, Tailored mechanical response and mass transport characteristic of selective laser melted porous metallic biomaterials for bone scaffolds, *Acta Biomater.* 112 (2020) 298–315, <https://doi.org/10.1016/j.actbio.2020.05.038>

[4] E. Alabort, D. Barba, R.C. Reed, Design of metallic bone by additive manufacturing, *Scr. Mater.* 164 (2019) 110–114, <https://doi.org/10.1016/j.scriptamat.2019.01.022>

[5] R.J. Kane, H.E. Weiss-Bilka, M.J. Meagher, Y. Liu, J.A. Gargac, G.L. Niebur, D.R. Wagner, R.K. Roeder, Hydroxyapatite reinforced collagen scaffolds with improved architecture and mechanical properties, *Acta Biomater.* 17 (2015) 16–25, <https://doi.org/10.1016/j.actbio.2015.01.031>

[6] A.A. Zadpoor, Mechanical performance of additively manufactured meta-biomaterials, *Acta Biomater.* 85 (2019) 41–59, <https://doi.org/10.1016/j.actbio.2018.12.038>

[7] M.J. Mirzaali, S. Janbaz, M. Strano, L. Vergani, A.A. Zadpoor, Shape-matching soft mechanical metamaterials, *Sci. Rep.* 8 (2018) 965, <https://doi.org/10.1038/s41598-018-19381-3>

[8] S.M. Ahmadi, R. Hedayati, Y. Li, K. Lietaert, N. Tümer, A. Fatemi, C.D. Rans, B. Pouran, H. Weinan, A.A. Zadpoor, Fatigue performance of additively manufactured meta-biomaterials: the effects of topology and material type, *Acta Biomater.* 65 (2018) 292–304, <https://doi.org/10.1016/j.actbio.2017.11.014>

[9] N. Kamboj, J. Kazantseva, R. Rahmani, M.A. Rodriguez, I. Hussainova, Selective laser sintered bio-inspired silicon-wollastonite scaffolds for bone tissue engineering, *Mater. Sci. Eng. C* 116 (2020) 111223, <https://doi.org/10.1016/j.msec.2020.111223>

[10] J. Karimi, P. Ma, Y.D. Jia, K.G. Prashanth, Linear patterning of high entropy alloy by additive manufacturing, *Manuf. Lett.* 24 (2020) 9–13, <https://doi.org/10.1016/j.mfglet.2020.03.003>

[11] J. Karimi, M.S. Xie, Z. Wang, K.G. Prashanth, Influence of substructures on the selective laser melted Ti-6Al-4V alloy as a function of laser re-melting, *J. Manuf. Process.* 68 (2021) 1387–1394, <https://doi.org/10.1016/j.jmapro.2021.06.059>

[12] L. Liu, R. Ivanov, R. Kumar, T. Minasyan, M. Antonov, Functionally gradient Ti6Al4V-TiB composite produced by spark plasma sintering functionally gradient Ti6Al4V-TiB composite produced by spark plasma sintering, *IOP Conf. Ser. Mater. Sci. Eng.* 1140 (2021) 12004, <https://doi.org/10.1088/1757-899X/1140/1/012004>

[13] P. Jamshidi, M. Aristizabal, W. Kong, V. Villapun, S.C. Cox, L.M. Grover, M.M. Attallah, Selective laser melting of Ti-6Al-4V: the impact of post-processing on the tensile, fatigue and biological properties for medical implant applications, *Materials* 13 (2020) 2813, <https://doi.org/10.3390/ma13122813>

[14] Y. Eyzat, M. Chemkhi, Q. Portella, J. Gardan, J. Remond, D. Reira, Characterization and mechanical properties of As-Built SLM Ti-6Al-4V subjected to surface mechanical post-treatment, *Procedia CIRP* 81 (2019) 1225–1229, <https://doi.org/10.1016/j.procir.2019.03.298>

[15] Z. Chen, X. Wu, D. Tomus, C.H.J. Davies, Surface roughness of selective laser melted Ti-6Al-4V alloy components, *Addit. Manuf.* 21 (2017) 91–103, <https://doi.org/10.1016/j.addma.2018.02.009>

[16] Q. Han, Y. Jiao, Effect of heat treatment and laser surface remelting on AISI10Mg alloy fabricated by selective laser melting, *Int. J. Adv. Manuf. Technol.* 102 (2019) 3315–3324, <https://doi.org/10.1007/s00170-018-03272-y>

[17] H. Ali, H. Ghadbeigi, K. Mumtaz, Effect of scanning strategies on residual stress and mechanical properties of Selective Laser Melted Ti6Al4V, *Mater. Sci. Eng. A* 712 (2018) 175–187, <https://doi.org/10.1016/j.msea.2017.11.103>

[18] J. Karimi, C. Suryanarayana, I. Okulov, K.G. Prashanth, Selective laser melting of Ti6Al4V: effect of laser re-melting, *Mater. Sci. Eng. A* 805 (2021) 140558, <https://doi.org/10.1016/j.msea.2020.140558>

[19] J.M. Jeon, J.M. Park, J.H. Yu, J.G. Kim, Y. Seong, S.H. Park, H.S. Kim, Effects of microstructure and internal defects on mechanical anisotropy and asymmetry of selective laser-melted 316L austenitic stainless steel, *Mater. Sci. Eng. A* 763 (2019) 138152, <https://doi.org/10.1016/j.msea.2019.138152>

[20] E. Yasa, J. Deckers, J.P. Kruth, M. Rombouts, J. Luyten, Charpy impact testing of metallic selective laser melting parts, *Virtual Phys. Prototyp.* 5 (2010) 89–98, <https://doi.org/10.1080/17452575.2010.503703894>

[21] W.A. Grell, E. Solis-Ramos, E. Clark, E. Lucon, E.J. Garboczi, P.K. Predecki, Z. Loftus, M. Kumosa, Effect of powder oxidation on the impact toughness of electron beam melting Ti-6Al-4V, *Addit. Manuf.* 17 (2017) 123–134, <https://doi.org/10.1016/j.addma.2017.08.002>

[22] P. Kumar, U. Ramamurty, High cycle fatigue in selective laser melted Ti-6Al-4V, *Acta Mater.* 194 (2020) 305–320, <https://doi.org/10.1016/j.actamat.2020.05.041>

[23] J. Gunther, D. Krewerth, T. Lippmann, S. Leuders, T. Troster, A. Weidner, H. Biermann, T. Niendorf, Fatigue life of additively manufactured Ti-6Al-4V in the very high cycle fatigue regime, *Int. J. Fatigue* 94 (2017) 236–245, <https://doi.org/10.1016/j.ijfatigue.2016.05.018>

[24] F. Cao, K.S. Ravi Chandran, The role of crack origin size and early stage crack growth on high cycle fatigue of powder metallurgy Ti-6Al-4V alloy, *Int. J. Fatigue* 102 (2017) 48–58, <https://doi.org/10.1016/j.ijfatigue.2017.05.004>

[25] B. Fotovvati, N. Namdari, A. Delghanghadikolaei, Fatigue performance of selective laser melted Ti6Al4V components: state of the art, *Mater. Res. Express* 6 (2019) 12002, <https://doi.org/10.1088/2053-1591/aae10e>

[26] H. Masuo, Y. Tanaka, S. Morokoshi, H. Yagura, T. Uchida, Y. Yamamoto, Y. Murakami, Influence of defects, surface roughness and HIP on the fatigue strength of Ti-6Al-4V manufactured by additive manufacturing, *Int. J. Fatigue* 117 (2018) 163–179, <https://doi.org/10.1016/j.ijfatigue.2018.07.020>

[27] M.D. Sangid, T.A. Book, D. Naragani, J. Rotella, P. Ravi, A. Finch, P. Kenesei, J.S. Park, H. Sharma, J. Almer, X. Xiao, Role of heat treatment and build orientation in the microstructure sensitive deformation characteristics of IN718 produced via SLM additive manufacturing, *Addit. Manuf.* 22 (2018) 479–496, <https://doi.org/10.1016/j.addma.2018.04.032>

[28] F. Pitt, M. Ramulu, Influence of grain size and microstructure on oxidation rates in titanium alloy Ti-6Al-4V under superplastic forming conditions, *J. Mater. Eng. Perform.* 13 (2004) 727–734, <https://doi.org/10.1361/1059949042>

[29] H. Li, D. Jia, Z. Yang, X. Liao, H. Jin, D. Cai, Y. Zhou, Effect of heat treatment on microstructure evolution and mechanical properties of selective laser melted Ti-6Al-4V and TiB/Ti-6Al-4V composite: a comparative study, *Mater. Sci. Eng. A* 801 (2021) 140415, <https://doi.org/10.1016/j.msea.2020.140415>

[30] M.E. Fitzpatrick, A.T. Fry, P. Holdway, F. Kandil, J. Shackleton, L. Suominen, Determination of Residual Stresses by X-ray Diffraction, *National Physical Laboratory Teddington, United Kingdom*, 2005.

[31] G. Nicoletto, R. Konecna, M. Frkan, E. Riva, Surface roughness and directional fatigue behavior of as-built EBM and DMLS Ti6Al4V, *Int. J. Fatigue* 116 (2018) 140–148, <https://doi.org/10.1016/j.ijfatigue.2018.06.011>

[32] A. Majeed, A. Ahmed, A. Salam, M.Z. Sheikh, Surface quality improvement by parameters analysis, optimization and heat treatment of AISI10Mg parts manufactured by SLM additive manufacturing, *Int. J. Lightweight Mater. Manuf.* 2 (2019) 288–295, <https://doi.org/10.1016/j.ijlmm.2019.08.001>

[33] L. Facchini, E. Magalini, P. Robotti, A. Molinari, S. Hoges, K. Wissenbach, Ductility of a Ti-6Al-4V alloy produced by selective laser melting of prealloyed powders, *Rapid Prototyp. J.* 16 (2010) 450–459, <https://doi.org/10.1108/13552541011083371>

[34] B. Vrancken, V. Cain, R. Knutsen, J. Van Humbeeck, Residual stress via the contour method in compact tension specimens produced via selective laser melting, *Scr. Mater.* 87 (2014) 29–32, <https://doi.org/10.1016/j.scriptamat.2014.05.016>

[35] K. Takao, K. Kusukawa, Fatigue notch characteristics of commercially pure titanium, *Mech. Behav. Mater.* 2 (1992) 445–450, <https://doi.org/10.1016/B978-0-08-037890-9.50189-7>

[36] P. Edwards, M. Ramulu, Fatigue performance evaluation of selective laser melted Ti-6Al-4V, *Mater. Sci. Eng. A* 598 (2014) 327–337, <https://doi.org/10.1016/j.msea.2014.01.041>

[37] Z. Xie, Y. Dai, X. Ou, S. Ni, M. Song, Effects of selective laser melting build orientations on the microstructure and tensile performance of Ti-6Al-4V alloy, *Mater. Sci. Eng. A* 776 (2020) 139001, <https://doi.org/10.1016/j.msea.2020.139001>

[38] S. Lou, X. Jiang, W. Sun, W. Zeng, L. Pagani, P.J. Scott, Characterisation methods for powder bed fusion processed surface topography, *Precis. Eng.* 57 (2018) 1–15, <https://doi.org/10.1016/j.precisioneng.2018.09.007>

[39] R. Li, J. Liu, Y. Shi, L. Wang, W. Jiang, Balling behavior of stainless steel and nickel powder during selective laser melting process, *Int. J. Adv. Manuf. Technol.* 59 (2012) 1025–1035, <https://doi.org/10.1007/s00170-011-3566-1>

[40] N. Hrabec, R. White, E. Lucon, Effects of internal porosity and crystallographic texture on Charpy absorbed energy of electron beam melting titanium alloy (Ti-6Al-4V), *Mater. Sci. Eng. A* 742 (2019) 269–277, <https://doi.org/10.1016/j.msea.2018.11.005>

[41] A. Majeed, Y. Zhang, J. Lv, T. Peng, Z. Atta, A. Ahmed, Investigation of T4 and T6 heat treatment influences on relative density and porosity of AISI10Mg alloy components manufactured by SLM, *Comput. Ind. Eng.* 139 (2020) 106194, <https://doi.org/10.1016/j.cie.2019.106194>

[42] P. Li, P.D. Lee, D.M. Maijer, T.C. Lindley, Quantification of the interaction within defect populations on fatigue behavior in an aluminum alloy, *Acta Mater.* 57 (2009) 3539–3548, <https://doi.org/10.1016/j.actamat.2009.04.008>

[43] B. Liu, B.Q. Li, Z. Li, Selective laser remelting of an additive layer manufacturing process on AISI10Mg, *Results Phys.* 12 (2018) 982–988, <https://doi.org/10.1016/j.rinp.2018.12.018>

[44] C. Pei, W. Zeng, H. Yuan, A damage evolution model based on micro-structural characteristics for an additive manufactured superalloy under monotonic and

- cyclic loading conditions, *Int. J. Fatigue* 131 (2020) 105279, <https://doi.org/10.1016/j.ijfatigue.2019.105279>
- [45] A.G. Demir, B. Previtali, Investigation of remelting and preheating in SLM of 18Ni300 maraging steel as corrective and preventive measures for porosity reduction, *Int. J. Adv. Manuf. Technol.* 93 (2017) 2697–2709, <https://doi.org/10.1007/s00170-017-0697-z>
- [46] L. Bourithis, G.D. Papadimitriou, J. Sideris, Comparison of wear properties of tool steels AISI D2 and O1 with the same hardness, *Tribol. Int.* 39 (2006) 479–489, <https://doi.org/10.1016/j.triboint.2005.03.005>
- [47] Z. Wang, Z. Liu, C. Gao, K. Wong, S. Ye, Z. Xiao, Modified wear behavior of selective laser melted Ti6Al4V alloy by direct current assisted ultrasonic surface rolling process, *Surf. Coat. Technol.* 381 (2019) 125122, <https://doi.org/10.1016/j.surfcoat.2019.125122>
- [48] D. Gu, Y.C. Hagedorn, W. Meiners, G. Meng, R.J.S. Batista, K. Wissenbach, R. Poprawe, Densification behavior, microstructure evolution, and wear performance of selective laser melting processed commercially pure titanium, *Acta Mater.* 60 (2012) 3849–3860, <https://doi.org/10.1016/j.actamat.2012.04.006>

# Curriculum vitae

## Personal data

Name: Javad Karimi  
Date of birth: 16.02.1986  
Place of birth: Borojen, Iran  
Citizenship: Iranian

## Contact data

E-mail: jkarim@taltech.ee; javadkarimimr@gmail.com

## Education

2018–2022 Tallinn University of Technology – PhD  
2014–2016 MSC  
2004–2008 BSC

## Language competence

Persian Native  
English Fluent  
Russian Proficient  
German Proficient

## Professional employment

2016–2018 Researcher, Iran National Gas Company (NIGC),  
Esfahan, Iran  
2014–2015 Young Researcher, Zarif Mosavar, Esfahan, Iran  
2010–2011 Junior Researcher, ShabSanat, Esfahan, Iran  
2008–2010 Junior Researcher, Azmonparto Gharb, Esfahan, Iran

## Research visit

01.12.2020–31.05.2022 Department of Mechatronics, Materials Science,  
University of Innsbruck, Austria

## Academic service

2020–Present Reviewed for Journal: Journal of Manufacturing  
Processes  
2022–Present Reviewed for Journal: Metallurgical and Materials  
Engineering

## Hobbies and life interest

I enjoy reading, and also writing down my ideas and helping others brings me true happiness as well as tending to plants.

## Elulookirjeldus

### Isikuandmed

Nimi: Javad Karimi  
Sünniaeg: 16.02.1986  
Sünnikoht: Borojen, Iraan  
Kodakondsus: Iraani

### Kontaktandmed

E-post: jkarim@taltech.ee; javadkarimimr@gmail.com

### Hariduskäik

2018–2022 Tallinna Tehnikaülikool – PhD  
2014–2016 MSC  
2004–2008 BSC

### Keelteoskus

Pärsia keel Emakeel  
Inglise keel Kõrgtase  
Vene keel Asjatundlik  
Saksa keel Asjatundlik

### Teenistuskäik

2016–2018 Teadur, Iraani riiklik gaasiettevõtte (NIGC), Esfahan, Iraan  
2014–2015 Nooremteadur, Zarif Mosavar, Esfahan, Iraan  
2010–2011 Nooremteadur, ShabSanat, Esfahan, Iraan  
2008–2010 Nooremteadur, Azmonparto Gharb, Esfahan, Iraan

### Välismaal teadustöö

01.12.2020–31.05.2022 Department of Mechatronics, Materials Science, University of Innsbruck, Austria

### Akadeemiline teenistus

2020–täneseni Arvustused teadusajakirja jaoks: Journal of Manufacturing Processes  
2022–täneseni Arvustused teadusajakirja jaoks: Metallurgical and Materials Engineering

### Harrastus

Mulle meeldib lugeda, aga tõelist naudingut pakub ka oma ideede kirja panemine, teiste abistamine ning ka taimede eest hoolitsemine.

ISSN 2585-6901 (PDF)  
ISBN 978-9949-83-892-9 (PDF)